

TURBINE BLADE TIP COOLING AND HEAT
TRANSFER

A Dissertation

Submitted to the Graduate Faculty of the
Louisiana State University and
Agricultural and Mechanical College
in partial fulfillment of the
requirements for the degree of
Doctor of Philosophy

in

The Department of Mechanical Engineering

by

Hasan Nasir

B.S., Bangladesh University of Engineering and Technology, 1997
December 2004

ACKNOWLEDGEMENTS

Behind every success, there is inspiration or support of at least one person. In my case, it was a group of people including my mentor, my family, and my friends. First of all, I would like to thank Dr. Srinath Ekkad for his guidance, wisdom, and financial support. I do not think many advisors would go to the lab to help his student running an experiment. Whenever I had any problem, I knew I could talk to him and he would help me to find a solution. It was no wonder that I started as a Masters student and decided to finish my Ph.D. with him. I was one of his first two students and over the years what Dr. Ekkad would like to say ‘grew old together’. Also, we become more like friends and I will cherish this friendship for my whole life. I could not ask for a better mentor. I especially want to thank my lovely wife Lubna for being in the lab with me during all late nights and long weekends. She literally helped me running some of my experiments. Without her love and support all the accomplishment in the world would mean nothing to me. I also must thank all of my lab mates, both past and present. Special thanks go out to Gautam Pamula, Ryan Herbert, Yiping Lu and Eric Esposito for their help and valuable suggestions on many occasions. Without their help, it would have been difficult to finish many of my tasks. I also would like to thank them to make my stay in the lab more enjoyable. Last and certainly not least, I have to thank my parents for their unconditional support and encouragement. They played a crucial part throughout my educational journey. Whenever I began to falter, they were there to reassure me and give me the confidence I needed to continue. They made many sacrifices and on many occasions, went beyond their limit to help me. I cannot over emphasize their role in my life and thank them enough. I am lucky to have such wonderful parents. Finally, I would like to thank my brothers, Robin, Shantunu and Rahat for their love and affection.

TABLE OF CONTENTS

ACKNOWLEDGEMENTS	i
LIST OF TABLES	v
LIST OF FIGURES	vi
NOMENCLATURE	ix
ABSTRACT	xii
CHAPTER 1	1
1.1 Introduction	1
1.2 Present Study	7
1.3 Literature Survey	9
CHAPTER 2	19
2.1 Heat Transfer Theory	19
2.2 Analysis of Semi-Infinite Solid Assumption	27
CHAPTER 3	30
3.1 Experimental Methods	30
3.2 Liquid Crystal Fundamentals	30
3.3 Infrared Thermography Fundamentals	32
3.4 Pressure Test	39
3.5 Heat Transfer Test	40
3.6 Uncertainty Analysis	42
CHAPTER 4	46
4.1 Description of the Test Facility	46
4.2 Test Apparatus	55
4.3 Inlet Flow Characterization	58
CHAPTER 5	61
5.1 Results (Uncooled Tip)	61
5.2 Pressure Data	62
5.3 Heat Transfer Data	64
CHAPTER 6	69
6.1 Results (Tip Injection)	69
6.2 Pressure Data	69
6.3 Heat Transfer Data	73

CHAPTER 7	79
7.1 Results (Pressure Side Hole Injection)	79
7.2 Pressure Data	79
7.3 Heat Transfer Data	82
CHAPTER 8	87
8.1 Results (Tip and Pressure Side Injection)	87
8.2 Pressure Data	87
8.3 Heat Transfer Data	91
CHAPTER 9	97
9.1 Conclusions	97
9.2 Future Works	98
REFERENCES	99
APPENDIX I: IR CAMERA MEASUREMENT FORMULA	104
APPENDIX II: UNCERTAINTY ANALYSIS	107
VITA	110

LIST OF TABLES

Table 6.1: Local blowing ratios for plane tip with tip only coolant injection	70
Table 6.2: Local blowing ratios for recessed tip with tip only coolant injection.....	72
Table 7.1: Local blowing ratios for plane tip with pressure side only coolant injection.....	81
Table 7.2: Local blowing ratios for recessed tip with pressure side only coolant injection.....	82
Table 8.1: Local blowing ratios for plane tip with combination coolant injection.....	89
Table 8.2: Local blowing ratios for recessed tip with combination coolant injection.....	91

LIST OF FIGURES

Figure 1.1: Components of gas turbine engine	1
Figure 1.2: Typical Blade Cooling.....	2
Figure 1.3: Tip leakage flow seen from the pressure side [1].....	3
Figure 1.4: Conceptual view of the leakage flow through the clearance gap	3
Figure 1.5: Plane tip blade [5].....	5
Figure 1.6: Recessed tip with peripheral squealer rim [5]	6
Figure 1.7: Blades with attached tip shrouds [5]	7
Figure 1.8: Tip leakage flow as explained by Bindon (1989).....	10
Figure 1.9: Overall view of leakage flow loss mechanisms (Yamamoto, 1989).....	12
Figure 1.10: Blade tip flow patterns for squealer tip (Ameri, 1989)	17
Figure 2.1: Flow over a flat plate.....	19
Figure 2.2: Film cooling over a flat plate	22
Figure 2.3: Boundary conditions	28
Figure 2.4: Temperature variation with time at various depths for Middle line.....	28
Figure 2.5: Temperature variation with time at various depths for Suction sideline.....	29
Figure 2.6: Temperature variation with time at various depths for Pressure sideline	29
Figure 3.1: Electromagnetic spectrum of radiation [36].....	33
Figure 3.2: Radiation emitted by a real surface. (a) Spectral distribution (b) Directional distribution [36]	34
Figure 3.3: Comparison between blackbody and real surface emission. (a) Spectral distribution (b) Directional distribution [36].....	35
Figure 4.1: Experimental set up	46
Figure 4.2: Pneumatic valve	47

Figure 4.3: Converging-diverging section	48
Figure 4.4: Top-view of the cascade.....	49
Figure 4.5: (a) Four bladed linear cascade, (b) Pressure blade.....	50
Figure 4.6: Pressure taps on the shroud	50
Figure 4.7: Heat transfer blade.....	51
Figure 4.8: Variable auto-transformer	52
Figure 4.9: Film cooling blade.....	53
Figure 4.10: Blade used for combined cooling.....	53
Figure 4.11: Coolant path	54
Figure 4.12: Pressure system	55
Figure 4.13: Schematic of the visual processing system for liquid crystal method.....	56
Figure 4.14: Schematic of the visual processing system for IR method.....	57
Figure 4.15: Transmissivity of Zinc-Selenide window with wavelengths [45].....	58
Figure 4.16: Inlet total pressure variation during blow down operation.....	59
Figure 4.17: Pressure distribution on the shroud for all three passages.....	60
Figure 5.1: Different squealer geometries tested	61
Figure 5.2: Surface pressure distribution at different span heights [46].....	62
Figure 5.3: Shroud pressure distribution for plain tip and different squealer geometries	63
Figure 5.4: Detailed heat transfer coefficient distribution for plane and different squealer geometries	65
Figure 5.5: Illustration of tip leakage flows for plain tip and squealer based on pressure and heat transfer distributions	66
Figure 5.6: Area averaged heat transfer coefficient for plane and different squealer geometries	68
Figure 6.1: Plane and recessed tip blade with tip coolant injection holes	69

Figure 6.2: Effect of blowing ratio on plane tip for tip coolant injection.....	70
Figure 6.3: Effect of blowing ratio on recessed tip for tip coolant injection.....	72
Figure 6.4: Effect of blowing ratio on plane tip heat transfer coefficient and film effectiveness distribution for tip coolant injection.....	76
Figure 6.5: Effect of blowing ratio on recessed tip heat transfer coefficient and film effectiveness distribution for tip coolant injection.....	77
Figure 6.6: Effect of blowing ratio on recessed tip net heat flux ratio distribution for tip coolant injection.....	78
Figure 7.1: Plane and recessed tip blade with pressure side coolant injection holes.....	79
Figure 7.2: Effects of blowing ratio on plane tip for pressure side coolant injection.....	80
Figure 7.3: Effects of blowing ratio on recessed tip for pressure side coolant injection.....	81
Figure 7.4: Effect of blowing ratio on plane tip heat transfer coefficient and film effectiveness distribution for pressure side coolant injection.....	84
Figure 7.5: Effect of blowing ratio on recessed tip heat transfer coefficient and film effectiveness distribution for pressure side coolant injection.....	85
Figure 7.6: Effect of blowing ratio on plane and recessed tip net heat flux ratio distribution for pressure side coolant injection.....	86
Figure 8.1: Plane and recessed tip blade with tip and pressure side coolant injection holes.....	87
Figure 8.2: Effect of blowing ratio on plane tip for tip and pressure side coolant injection.....	88
Figure 8.3: Effect of blowing ratio on recessed tip for tip and pressure side coolant injection ...	90
Figure 8.4: Effect of blowing ratio on plane tip heat transfer coefficient and film effectiveness distribution for tip and pressure side coolant injection.....	94
Figure 8.5: Effect of blowing ratio on recessed tip heat transfer coefficient and film effectiveness distribution for tip and pressure side coolant injection.....	95
Figure 8.6: Effect of blowing ratio on plane and recessed tip net heat flux ratio distribution for tip and pressure side coolant injection.....	96

NOMENCLATURE

C	chord
C_D	discharge coefficient
d	diameter of film cooling hole
D	squealer depth
E_λ	spectral emissive power
$E_{\lambda,b}$	spectral emissive power of blackbody
H	height of test blade
h	heat transfer coefficient with film injection
h_0	heat transfer coefficient without holes
I_λ	spectral intensity
$I_{\lambda,b}$	spectral intensity of black body
k	thermal conductivity of plexiglas test surface or specific heat ratio
\dot{m}	actual mass flow rate of coolant
M	blowing ratio, $\rho_c U_c / \rho_m U_m$
P	pressure
PR	pressure ratio
P_m	static pressure of mainstream
P_s	static pressure
P_t	total pressure
P_{tc}	total pressure of coolant inside plenum
q''	heat flux with film injection
q''_0	heat flux without film injection

R	gas constant
Re	free stream Reynolds number, $\rho UC/\mu$
S	blade spacing
t	time of color change or the time when the IR image was taken after the test was initiated.
T	temperature
T_{atm}	atmospheric temperature
T_c	coolant temperature
T_f	film temperature
T_i	initial temperature
T_m	mainstream temperature
T_{refl}	reflected ambient temperature
T_{tc}	total temperature of coolant inside plenum
T_w	color change temperature or the prescribed wall temperature
T_u	free stream turbulence
U_c	coolant velocity
U_m	mainstream velocity
U_{source}	camera output signal
W_{atm}	total emissive power of atmosphere
W_b	total emissive power of blackbody
W_o, W_{obj}	total emissive power of the object
W_{refl}	reflected emissive power
x	distance

Greek Symbols

λ	wavelength
θ	zenith angle
α	thermal diffusivity of plexiglas test surface
α_λ	spectral absorbance
ρ	density of air
ρ_λ	spectral reflectance
τ	step change in time
τ_λ	spectral transmittance
ε_λ	spectral emissivity
η	film effectiveness, $\frac{T_f - T_m}{T_c - T_m}$
ϕ	overall cooling effectiveness, $\frac{T_f - T_c}{T_m - T_c}$
μ	viscosity of air

ABSTRACT

Turbine blade tip leakage flow from blade pressure side to suction side over the tip surface increases the thermal loading to the blade tip, leading to a high local temperature and thus, is considered one of the primary sources of blade failure. Leakage flow can be reduced by using a recessed or squealer tip blade or by cooling the blade tip to incorporate film cooling. The performance of different recessed tip geometries were investigated and compared with plane tip performance. A transient liquid crystal technique was employed to measure detailed heat transfer coefficient distributions. Coolant injection from holes located on the blade tip, near the tip along the pressure side and combination cases were also investigated. Experiments were performed for plane tip and squealer tip for different coolant to mainstream blowing ratios of 1.0, 2.0, and 3.0. A transient infrared (IR) thermography technique was used to simultaneously measure heat transfer coefficient and film cooling effectiveness. Static pressure distributions on the shroud were measured to obtain some understanding about the leakage flow direction and its effect on surface heat transfer distribution. All tests were performed in a four bladed, stationary, linear cascade. The Reynolds number based on cascade exit velocity and axial chord length was 8.61×10^5 and the inlet and exit Mach numbers were 0.16 and 0.55, respectively. Tip gap-to-blade span ratio of 1% and recess depth-to-blade span ratio of 4.16% was used. Results showed that performance of the full pressure side squealer was the poorest and that a squealer tip performs better than the plane tip blade. Tip injection reduced heat transfer coefficient on the blade tip and an increase in blowing ratio caused a decrease in heat transfer coefficient for both plane and squealer tip blade. For pressure side film injection, film effectiveness was lower than tip injection. Some reattachment of jets was observed at blowing ratio of 3.0 for plane tip. For squealer tip, almost no film effectiveness was observed. In case of combination cooling, very

high film effectiveness and heat transfer coefficient is observed at blowing ratio of 3.0 for both plane and squealer tip blade tip.

CHAPTER 1

1.1 Introduction

A turbine is a rotating device that uses the action of a fluid to produce work. In gas turbine, a pressurized, high temperature gas is the driving force. For electrical power generation and marine applications, it is generally called a power turbine. For aviation purposes, it is usually called a gas generator. One of the reasons that gas turbine engines are widely used to power aircraft is they are light and compact and have a high power-to-weight ratio. Gas turbines are used in all kinds of unexpected places such as helicopters and even the M-1 tank. The value of gas turbines produced in 2002, both aviation and non-aviation combined, reaches an all time high exceeding the annual sales of all but the top 35 businesses in the world.

The main three components of a gas turbine engine are compressor, combustor and turbine as shown in Figure 1.1. The compressor compresses the incoming air to high pressure, the combustor burns the fuel and produces high pressure, high temperature high velocity gas and the turbine extracts the energy from the gas.

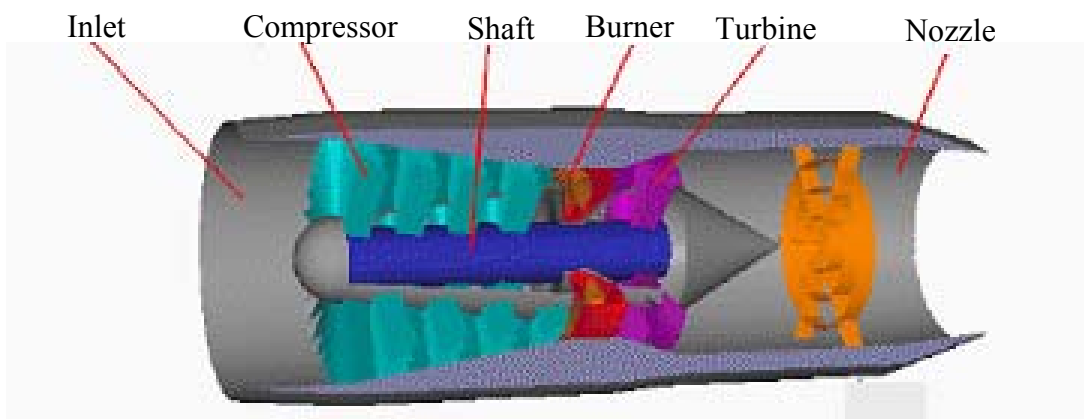


Figure 1.1: Components of gas turbine engine

One way to increase power and efficiency of gas turbines is by increasing turbine-operating temperatures. The motivation behind this is that higher temperature gases yield higher energy potential. However, the components along the hot gas path experience high thermal loading, which can cause distress. The HPT (High Pressure Turbine) first stage blade is one component that is extremely vulnerable to the hot gas. The turbine blades are exposed to a continuous flow of gas that may enter the turbine at a temperature between 850 °C to 1700 °C. This temperature is far beyond the melting point of current materials technology. The turbine blades are required to perform and survive long operating periods at temperatures above their melting point. Various internal and external cooling techniques are employed to bring down the temperature of the blade material temperature below its melting point. As shown in Figure 1.2, in internal cooling, relatively cold air is bypassed from the compressor and passed through the hollow passages inside the turbine blade. In external cooling, the bypassed air is exited out through small holes at discrete locations of the turbine blade. This relatively cold air creates a protective blanket that protects the turbine blade from the harsh environment. This type of cooling is called film cooling.

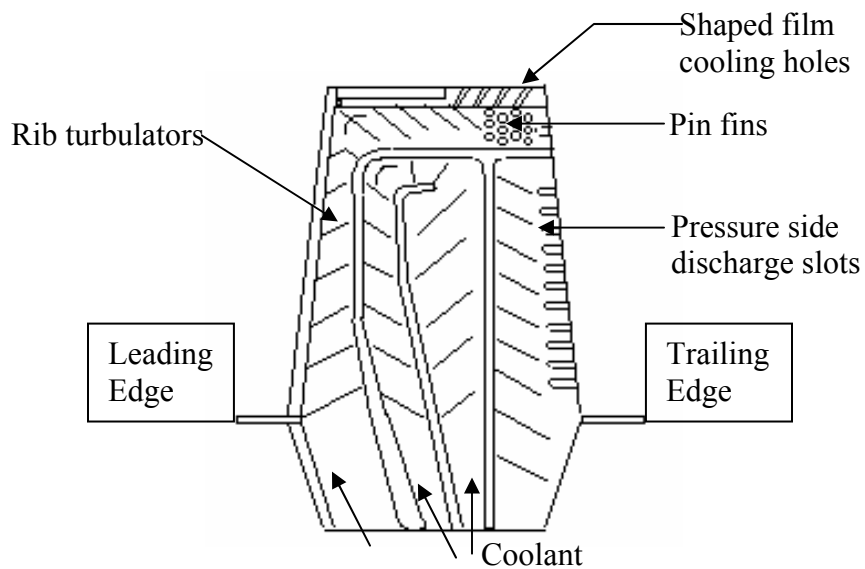


Figure 1.2: Typical Blade Cooling

Gas turbine blades usually have a gap between the blade tip and the stationary casing or the shroud surface known as tip gap (Figure 1.3 and Figure 1.4). This clearance gap is necessary to allow for the blade's rotation and for its mechanical and thermal growth. Due to the pressure difference between the pressure side and the suction side of the blade, hot gas leaks through this gap from the pressure side to the suction side. This is known as tip leakage flow.

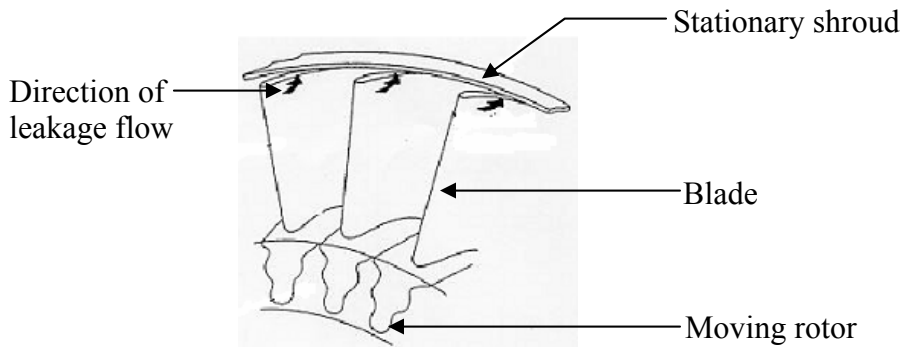


Figure 1.3: Tip leakage flow seen from the pressure side [1]

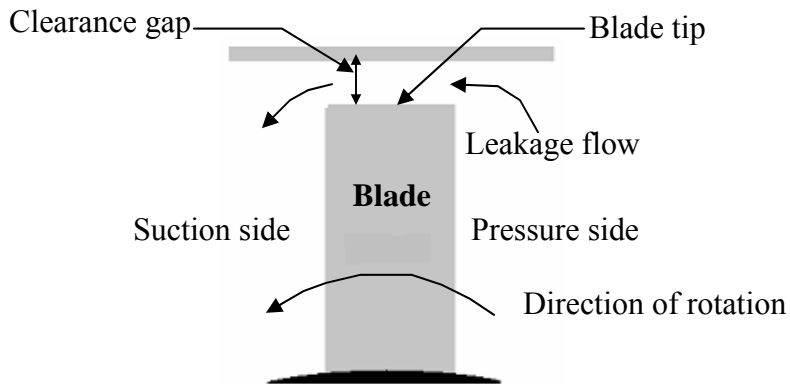


Figure 1.4: Conceptual view of the leakage flow through the clearance gap

The leakage flow results in a reduction in the blade force, the work done and therefore the overall efficiency. In fact, one third of the losses that are associated with the blade or rotor can be attributed to leakage flow [2]. This hot leakage flow also increases the thermal loading on

the blade tip, leading to a high local temperature and thus, is considered one of the primary sources of blade failure. Heat transfer rates at the tip can be the highest over the entire blade surface, leading to large temperature gradients and related durability problems [3]. In general, tip clearances for large commercial engines are of the order of 0.25 mm, which can reduce the specific fuel consumption by 1% and EGT (Exhaust Gas Temperature) by 10 °C [3]. The increase in exit gas temperature is a direct indication of the operational degradation of the engine. If the EGT is higher than a predetermined temperature relative to the initial new or serviced condition, the engine is either turned down in power or removed from service for maintenance. For aircraft engines, significant variations in clearance occur at different operating conditions such as take off and cruise. Differential thermal expansion between the rotating blades and the stationary shroud causes this variation in clearance gap. Also, for some engines, the shroud cools at a much faster rate than the disk resulting in a significant reduction in tip gap to the point that rubbing occurs. These are the main concerns of blade designers.

A perfect blade tip will not allow any leakage flow, generate no secondary flows to reduce stage efficiency nor create losses for downstream airfoil stages and will not require any cooling thereby presenting no thermodynamic losses from the use of compressed air [5]. Therefore, the two main objectives of blade design engineers are (1) to reduce the leakage flow either by reducing the tip gap or by implementing a more effective tip leakage sealing mechanism and (2) to cool the blade tips with the least possible usage of cooling fluid. However, all the blade tips used in today's engine do allow some leakage flow and generate secondary flows. The three major types of blade tips that are being used today: (1) plane tip, (2) recessed tip with peripheral squealer sealing rims, and (3) attached tip shrouds used with plane or flared blade tips. Each blade tips has its advantages and disadvantages.

A very few engines now-a-days use plane blade tip. Figure 1.5 shows a plane tip. Since, any physical leakage resistance sealing mechanisms are absent in this type of blade tip, it provides the lowest aerodynamic efficiency due to relatively high leakages. Plane blade tips may also be more susceptible to damage if and when they do rub against the shroud. But it is easy to design this type of blade tip, as there are no extended surfaces to be cooled like in recessed tip with squealer sealing rims. Film cooling holes on the top can be seen in the figure. The location of the film cooling holes is the direct consequences of the internal cooling passages within the blade. These holes are called purge holes. The functions of the dirt purge holes include the following: (1) purge holes allow centrifugal forces to expel any dirt ingested by the compressor into the turbine rather than clogging the smaller diameter film cooling holes; (2) purge holes provide a way to support the ceramic core during the lost-wax investment casting of the blade manufacturing process, and (3) the extra coolant helps in reducing thermal load at the tip [6].

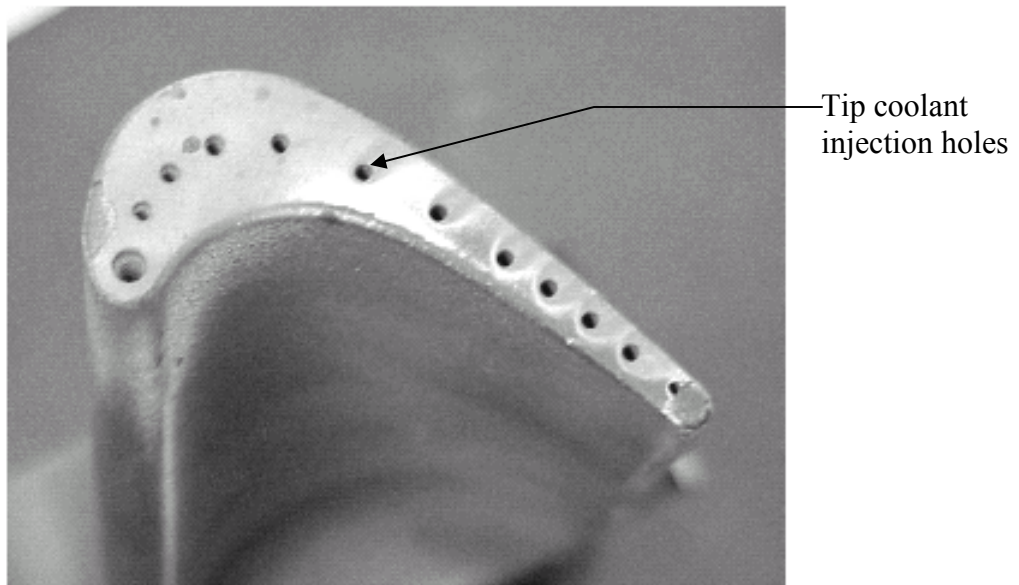


Figure 1.5: Plane tip blade [5]

Recessed tip with a perimeter seal strip is the most common design in practice today within HPT (High Pressure Turbine) blades. Figure 1.6 shows an example of a squealer tip blade. The squealer rim is a natural radial extension of the aerodynamic surface of the airfoil. The function of the squealer rim is to act as a simple two-tooth labyrinth seal. Tip leakage gas is first forced to contract between the pressure side rim and the shroud, then expand into the cavity, and then contract again to pass the suction side rim restriction before expanding into the main flow. A recessed tip with peripheral rim allows a smaller tip clearance, but reduces the risk of blade damage, if the tip rubs against the shroud. This type of blade tip running with a very tight clearance can be a very effective seal. However, the design of recessed tip blade is more complex than the plane tip because of the cooling of the rim to prevent loss by oxidation and erosion. The rim acts as an extended fin that sometimes requires many pressure side film cooling holes, to adequately cool the rim.

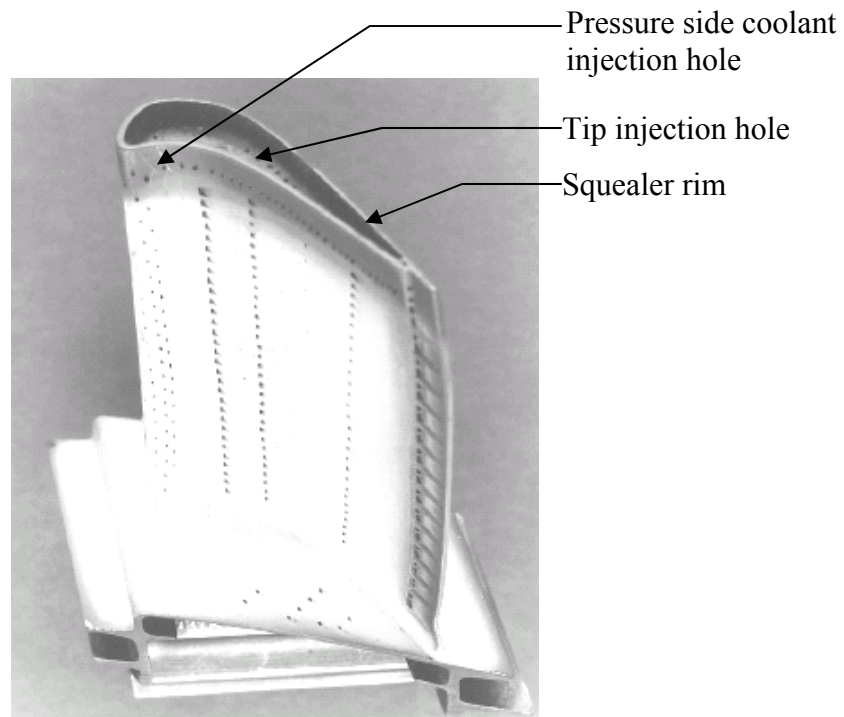


Figure 1.6: Recessed tip with peripheral squealer rim [5]

Blades with attached tip shrouds are mostly used in LPT (Low Pressure Turbine) blades. Figure 1.7 shows an example of such blades. The tip shroud is in essence an inner shroud that moves with the blade tip. There is a stationary shroud casing outside of this tip shroud. Of all the current blade tip design in use today, the tip shroud has the lowest aerodynamic loss when properly installed. But designers have to pay great attention to stress because this blade tip is heavier than plane or recessed tip with squealer rim blade tip due to added mass. This also requires a much more complex cooling system, not only because of the geometry, but also to maintain material temperatures for acceptable stresses.

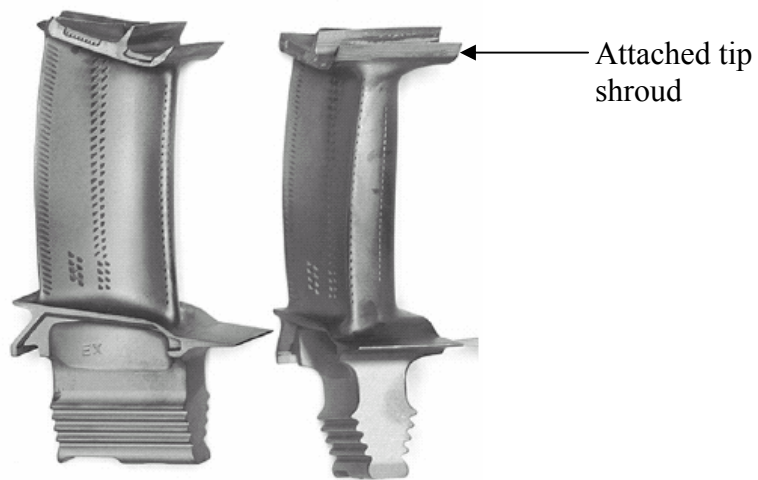


Figure 1.7: Blades with attached tip shrouds [5]

1.2 Present Study

Many parameters affect blade tip heat transfer. Parameters such as mainstream Reynolds number, inlet Mach number and turbulence intensity, unsteady wakes from the trailing edge of the nozzle guide vanes make a significant contribution to the heat load distribution over the blade tip. The total blade turning angle and general blade geometry such as the presence of a squealer

and edge radius, tip gap height and squealer depth also have a tremendous influence on blade tip heat transfer. The effects of these parameters continue to be of interest to those working in the gas turbine industry.

Due to the harsh environment, small thickness of the squealer rim and sometimes, accidental rubbing of the squealer rim against the shroud, some portion of the squealer rim may burn off or break down and fall off. It is unclear how the burned off or damaged squealer perform in this environment. It is a matter of great interest to the engine designer to determine if the partial squealer rim performance is adequate to not require replacing the blade. It is also important to determine the associated heat transfer coefficient for the damaged squealer rim and compare the results with the plane tip and the undamaged or full squealer rim.

Film cooling or injection of relatively cold air through holes to create a protective blanket is also used on the blade tip. When the blade material temperature exceeds a safe temperature limit, film cooling technique by using compressor discharge air is used to retain adequate material properties and structure. But such cooling decreases cycle efficiency as it represents bypassing of the engine main flow path. So, blade designers have to use the bypass air wisely. In film cooling situations, there is a need to determine both local adiabatic wall temperature and heat transfer coefficient to fully assess the local heat flux into the surface.

The objectives of the present study are as follows:

- To investigate the effect of different squealer rim geometry on heat transfer coefficient and static pressure distribution on a gas turbine blade tip in a four-bladed stationary linear cascade.
- To understand leakage flow behavior and associated heat transfer for damaged or burned squealer rim geometry.

- To study the effect of film injection on plane blade tip, measure heat transfer coefficient and film effectiveness for different blowing ratios.
- To study the effect of film injection on recessed tip with peripheral squealer rim blade tip, measure heat transfer coefficient and film effectiveness for different blowing ratios.
- To study the effect of film injection from pressure side holes on plane and recessed tip with peripheral squealer rim blade, measure heat transfer coefficient and film effectiveness for different blowing ratios.
- To study the effect of combination cooling when film is injected from both holes located on blade tip and pressure side, determine heat transfer coefficient and film effectiveness for different blowing ratios.

This investigation differs from those in the past because the tip profile from an in-service High Pressure Turbine of an aircraft engine was used. Other experiments have used the E³ test blade or a power generation blade that have different characteristics. Also, this is the first time heat transfer study for likely damaged squealer tip is considered. The pressure ratio (inlet total pressure to exit static pressure) used is 1.2, which is lower than the actual pressure ratio this blade sees in service (PR = 1.7). A transient liquid crystal technique is used to obtain the tip heat transfer distributions for damaged squealer tips. Whereas, infrared thermography is used to measure heat transfer coefficient and film effectiveness for blade tip film cooling cases. Pressure measurements are made on the shroud to characterize the leakage flow and understand the heat transfer distributions.

1.3 Literature Survey

Tip leakage flow has been known and subject to research for a long time. Rains [7] studied the tip clearance flow in axial compressors and pumps in 1954. Earlier researchers were

all concerned with the leakage flow characteristics and the effect of leakage flow on efficiency of machines. Lakshminarayana [8] proposed an expression to predict the decrease in stage efficiency due to tip clearance. The expression was based on author's earlier flow model for the tip clearance and taking into account all the flow and blade parameters that affect the clearance flow. The predictions agreed closely with several compressor, fan, pump and turbine data available at that time.

Booth et al. [9] outlined a new methodology for predicting and minimizing tip leakage flows. Their analysis considered the momentum balance and their results showed that in the range of tip clearances seen on turbines, the flow over the blade tip may be regarded as primarily inviscid. The proposed model treated the normal velocity component in terms of discharge coefficient and conserved the tangential velocity (momentum) component. The experiments were conducted on a series of three water flow rigs.

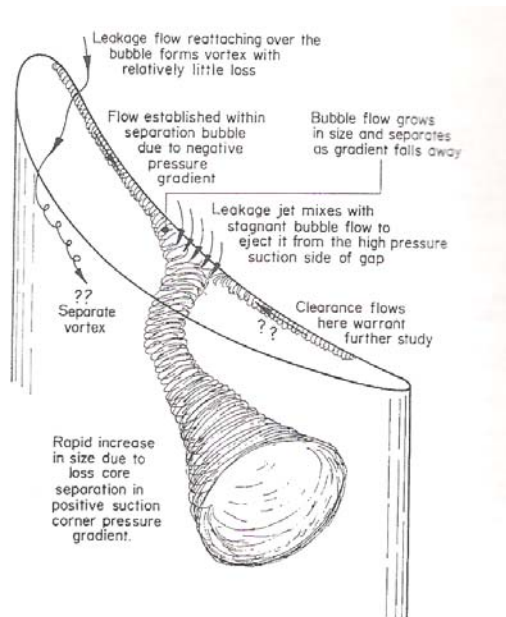


Figure 1.8: Tip leakage flow as explained by Bindon (1989)

Bindon [2] examined the data of Bindon [10,11] to identify and quantify the loss processes in the whole endwall region with tip clearance. The data was taken for a flat tipped seven-blade cascade by using the quantitative streamline gas tracer technique and microscopic velocity probes. He concluded that tip clearance loss varies linearly with gap size. The most important finding was that the internal gap loss made up of 39 percent of the total endwall loss, suction corner mixing loss formed 48 percent and endwall/secondary loss, the remaining 13 percent. It is also suggested that the control of tip clearance loss by reducing the discharge coefficient actually introduces loss.

Yamamoto [12] discussed the mechanism of three-dimensional flows and of the associated losses occurring near the tip endwall region for a six-bladed linear cascade. A five hole Pitot tube with head width of only 0.6 mm was used to survey flows close to the endwall and inside the clearance. The study (Figure 1.9) showed that leakage flow vectors within the clearance gap depend strongly on the incidence and the gap size, particularly within the front part of the gap where the inlet boundary layer fluids pass as a part of leakage flow. His results also showed that leakage vortices are less sensitive to incidence variation than the passage vortex. Another important finding was that the inertia forces of the inlet boundary layer fluids become an important cause of leakage flow with larger clearances, while the pressure gradient within the gap is more important with small clearances.

Yaras et al. [13] measured velocity, flow direction and total pressure within the clearance gap as well as blade surface and endwall static pressure in a five-bladed linear cascade for three clearance gaps. They used a three-hole probe for measurements within the gap. They noted some separation bubbles near the pressure side corner, which took the form of vortices. They also concluded that the regions close to the tip contributes little to the total leakage through the gap

and most of the leakage occurs near the endwall.

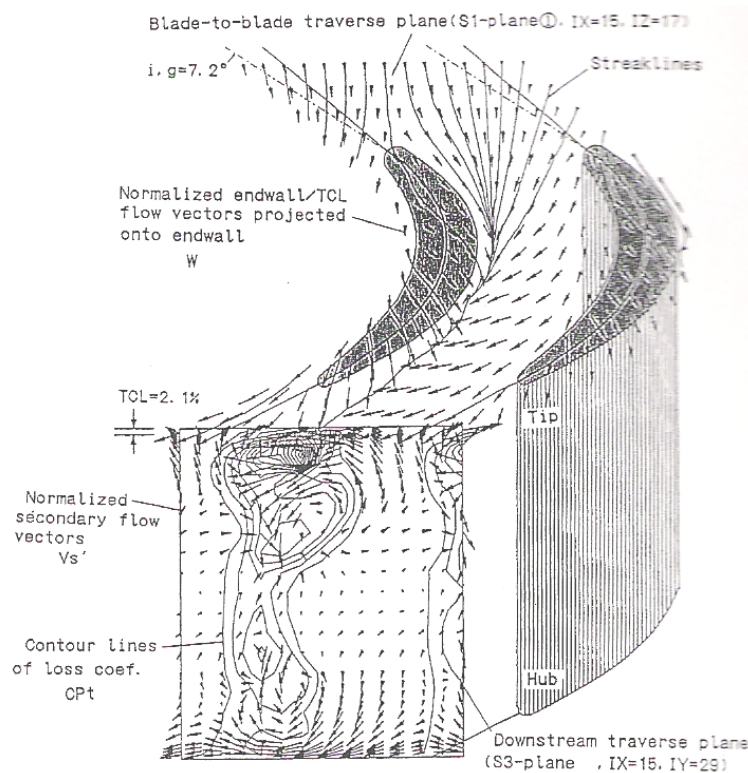


Figure 1.9: Overall view of leakage flow loss mechanisms (Yamamoto, 1989)

The first published study of blade tip heat transfer was the investigation of Mayle and Metzger [14]. Tip average heat transfer coefficients were measured for nominally flat tip models with various flow Reynolds number and rotational speeds. They found that the average tip heat transfer was only a weak function of the rotational speed and the leakage flow is mainly pressure driven. Chyu et al. [15] studied local details of tip heat transfer coefficients for rectangular cavity using moving shroud. It was again determined that the relative motion had a minor influence on the average tip heat transfer though some local effects were observed. Recently Srinivasan et al. [16] studied the effect of endwall motion on blade tip heat transfer. They found 9 percent

reductions on blade tip heat transfer due to wall motion for small clearance. At higher clearances, there was no measurable effect of relative motion.

Bunker et al. [17] were the first to report full surface information on heat transfer coefficients over an airfoil blade tip and shroud model that develops an appropriate pressure distribution for a geometry typical of large power generation turbines. A hue detection based liquid crystal method was used to obtain data for flat, smooth tip surfaces with both sharp and rounded edges. The experimental facility used was a cold flow, steady-state blade, stationary cascade comprised of three airfoils. Their results showed that the pressures measured on the airfoil in the near-tip region form a good basis for determining the overall pressure driven tip leakage flows and shroud pressure measurements agree well with the tip surface pressure. They also observed a characteristic sweet spot of low heat transfer which extends into the midchord region and toward the suction side.

Bunker and Bailey [18] investigated the effect of squealer cavity depth on detailed tip cavity heat transfer. It was found that the effect of cavity depth is not uniform over the entire tip cavity and heat transfer coefficient decreases as the cavity depth increases. Their study also showed that pressure side material loss near the midchord region actually reduces tip heat transfer. Bunker and Bailey [19] explored various tip leakage sealing methods. Local static pressure and heat transfer coefficient using hue intensity method were acquired on the blade tip. The results showed that perimeter squealer rim is the best. Angled strips are better than circumferential and mean chamber strip though all of them increased the heat load over that associated with smooth surface.

Azad et al. [20] studied the effect of different squealer geometry arrangement on blade tip heat transfer coefficient and static pressure distributions. The study was conducted in a five-

bladed linear cascade using transient liquid crystal technique. The overall pressure ratio was 1.32. Their results showed that shroud static pressure measurements provide a good explanation of heat transfer measurements. Also the location of the squealer changes the leakage flow and associated heat transfer. A single squealer on the suction side provides better sealing than single squealer on pressure side or mid camber line.

Teng et al. [21] measured detailed heat transfer coefficient on the blade tip and static pressure data on the shroud. Effects of tip gap and upstream unsteady wake were studied in a low-speed, five-bladed linear cascade. They observed a high heat transfer coefficient on the pressure side as opposed to the suction side. It is also found that reduced tip clearance leads to reduced heat transfer coefficient and unsteady wake effect slightly increases the averaged Nusselt number.

Kwak et al. [22] measured heat transfer coefficients on the blade tip, shroud and also near tip regions of the pressure and suction sides of a blade. Various combinations of single and double squealers were studied. It was found that suction side squealer is better and the effect of tip gap clearance and squealer arrangement has less effect on pressure side heat transfer coefficient.

Papa et al. [23] studied the effect of tip geometry and tip clearance on mass/heat transfer for a large-scale gas turbine blade. Flow visualization using oil dot technique was also studied. For a squealer tip, they observed that incoming flow impinges on the cavity floor and part of the mainstream flow rolls up into a vortex that fills most of the cavity and part is directed toward the suction side squealer. They also observed that increasing the gap level moves the starting point of the leakage flow rearward.

Dunn et al. [24] determined the blade platform heat-flux level and the influence of blade

tip recess on the tip heat transfer for a full-scale rotating turbine stage using thin-film resistance thermometer. The results showed that Nusselt number values on the floor of the recess near the leading edge and on the suction side rim were in excess of the blade stagnation value.

Saxena et al. [25] performed a systematic investigation of various tip leakage flow sealing methods on flow and heat transfer over a turbine blade tip in a low speed cascade. It was found that the trip strips placed in a direction orthogonal to the leakage flow direction produces the lowest leakage flow and heat transfer coefficient. It was also shown that the presence of wake and free-stream turbulence produced higher heat transfer coefficient for the plane tip, however, the enhancement is negligible for other tip geometries.

Kim and other associates of Professor Darryl E. Metzger [26] in a paper honoring the late Professor summarized his more recent experimental work that investigated the effects of coolant injection on convection heat transfer to the blade tip for a variety of tip shapes and coolant injection configuration. Stationary blade tip models and transient liquid crystal technique was used to acquire data. Their results showed that discrete slot injections are better than round hole injections. Also overall film-cooling performance varied significantly with injection location for the grooved-tip cavity injection.

Kwak et al. [27] investigated the effect of film injection on an actual gas turbine blade tip. They found that static pressure on the shroud and film-cooling effectiveness increased as the blowing ratio increased, whereas heat transfer coefficient decreased slightly with increasing blowing ratio. They concluded that these effects might be due to blockage effect of the injected coolant into the tip gap.

Ahn et al. [28] studied the effects of the presence of squealer rim, the location of the film cooling holes, and the tip gap clearance on the film cooling effectiveness in comparison to plane

tip. They used pressure sensitive paint technique. Film cooling holes were located along the camber line on the tip and along the span of the pressure side. All measurements were made at three different tip gap clearances of 1%, 1.5% and 2.5% of blade span. They found that for plane tip cases, the film-cooling effectiveness on blade tip is higher for the case with pressure side injection as compared to only tip and combination (both tip and pressure side injection). Also, squealer blade tip showed negligible film effectiveness for pressure side injection whereas the plane tip showed significant film effectiveness.

Christophel et al. [4] performed experiments in a linear cascade to measure adiabatic effectiveness and heat transfer for blowing from the tip of a turbine blade for two tip gap heights over a range of blowing ratios. They found that the dirt purge jets provided a significant amount of cooling for the leading edge area particularly for the small tip gap case. Also, increased blowing resulted in a larger cooling benefit for the large tip gap as compared with small tip gap. In another paper, Christophel et al. [29] studied the effects of blowing from the pressure side of the tip as well as dirt purge holes placed on the tip. It was found that when injecting coolant through pressure side film cooling holes, tip heat transfer increases with increased gap height. Also, increased blowing ratio caused enhancement of heat transfer on the tip surface.

Polanka et al. [30] compared the experimental data taken in the tip region of a fully rotating turbine blade rotor with true predictions of the flow field made with a 3-D RANS solver. The results showed that the clearance has more of an effect with downstream distance for the tip, particularly after the throat of the blade passage.

Ameri et al. [31] conducted a numerical study of heat transfer on a recessed tip with squealer rim of a generic modern gas turbine blade. The simulations were carried out using a second-order-accurate finite volume scheme on a multiblock grid system. Good agreements with

experimental results were obtained. They observed two dominant vortical structures (Figure 1.10) in the recess region that affected the heat transfer rate significantly. The same group of authors [32] studied the effects of tip clearance and casing recess on heat transfer and stage efficiency in axial turbines. Their numerical study reconfirmed the linear relationship between the efficiency and tip gap height. Also, introduction of recessed casing resulted in a drop in the rate of heat transfer on the pressure side.

Ameri [33] predicted and compared the heat transfer and flow on the blade tip equipped with mean-camberline strip. It was found that mean-camberline strip reduces the tip leakage by as much as 28 percent. It was also observed that sharp edge works better than radiused edge in reducing the tip leakage flow.

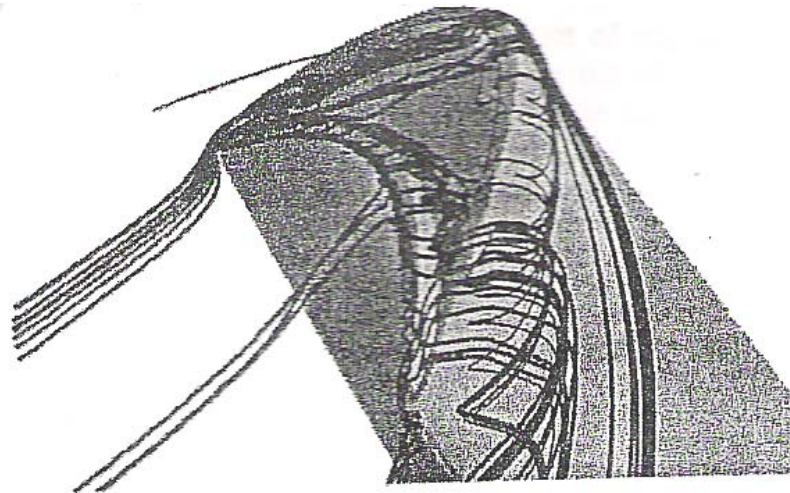


Figure 1.10: Blade tip flow patterns for squealer tip (Ameri, 1989)

Yang et al. [34] performed numerical calculations for a squealer tip. They studied the effect of height, used three different turbulent model and as well as compared their squealer tip data with flat tip blade and experimental data. Reynolds stress model provided the best

agreement and squealer tip proved to be better than flat tip in reducing heat transfer and leakage flow.

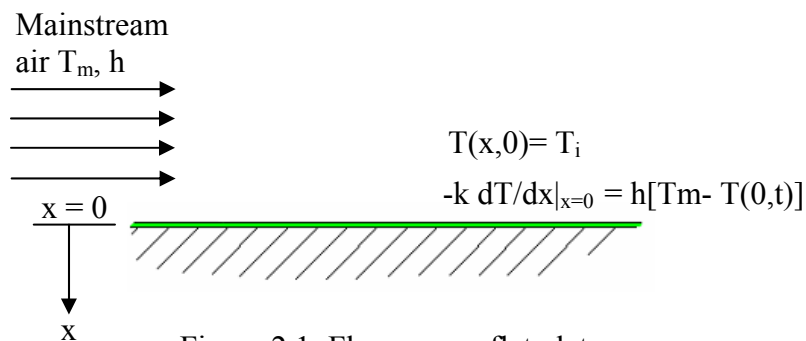
Yang et al. [35] predicted film cooling effectiveness and heat transfer coefficient for three types of film-hole arrangements: 1) the holes located on the mid-camber line of the tips, 2) the holes located upstream of the tip leakage flow and high heat transfer region, 3) combined arrangements of camber and upstream holes. They found that upstream film hole arrangements provided better film cooling performance than camber arrangements.

CHAPTER 2

The main goals of this study are to determine the heat transfer coefficients and film effectiveness. The chapter will present the heat transfer model, the boundary conditions, assumptions behind the model and their validation.

2.1 Heat Transfer Theory

Consider the transient flow over a flat plate as shown in Figure 2.1. In this case, the test plate is initially at a uniform temperature, T_i , and the convective boundary condition is suddenly applied on the plate at time, $t > 0$. Now, if we assume that heat is conducted only in x-direction and perform an energy balance on the plate, we get



The 1-D transient conduction equation

$$\frac{\partial^2 T}{\partial x^2} = \frac{1}{\alpha} \frac{\partial T}{\partial t} \quad (1)$$

The boundary condition (BC) is

$$\text{At } x = 0, \quad -k \frac{\partial T}{\partial x} \Big|_{x=0} = h[T_m - T(0,t)]$$

The initial condition (IC) is

$$\text{At } t = 0, \quad T = T_i, \text{ through out the plate}$$

Equation (1) is a second order partial differential equation; therefore one more BC is required to solve the equation.

The variables used in the above equations are as follows:

T_w = The color change temperature or the prescribed wall temperature

T_i = Initial temperature of the test surface

T_m = Mainstream air temperature

k = Thermal conductivity of plexiglas

α = Thermal diffusivity of plexiglas

t = Time of color change or the time when the IR image was taken after the test was initiated.

h = Heat transfer coefficient

Analytical solution to the transient conduction problem shown in Figure 2.1 can be obtained for the semi-infinite solid, which is any solid that extends to infinity in all but one direction. The semi-infinite solid assumption can also be applied to any situation where the thermal wave applied to one end does not reach the other end during the time frame of interest or test duration. The application of the semi-infinite solid assumption gives an additional BC, which is

$$\text{As } x \rightarrow \infty, T = T_i \text{ for all } t$$

The semi-infinite solid assumptions are valid for our case for two reasons. The test duration is small, usually less than 60 seconds. Secondly, the test surface is made of Plexiglas that has low thermal conductivity, low thermal diffusivity and low lateral conduction. Combinations of the above facts make sure that heat is conducted only in the x-direction and it does not reach the bottom of the test surface.

Solving Equation (1) with the prescribed initial and boundary conditions, the non-

dimensional temperature at the convective boundary surface (at $x = 0$) can be obtained [36]:

$$\frac{T_w - T_i}{T_m - T_i} = 1 - \left[\exp\left(\frac{h^2 \alpha t}{k^2}\right) \right] \left[\operatorname{erfc}\left(\frac{h\sqrt{\alpha t}}{k}\right) \right] \quad (2)$$

For liquid crystal technique, T_w is known prior to the test based on factory setting or *in situ* calibration. For infrared (IR) technique, T_w is the wall temperature that we measure with IR camera. The initial temperature (T_i) of the test surface and the mainstream temperature (T_m) are measured before and during test respectively. The properties of the Plexiglas material such as thermal conductivity (k) and thermal diffusivity (α) are also known. For liquid crystal technique, t is the time of color change that is measured using a frame grabber board and commercial software. For infrared technique, t is the time when the IR image was taken after the test was initiated. So, basically, except for the heat transfer coefficient, h , all the variables in the above equation are either known or measured.

Unlike the heat transfer coefficient measurement for flow over a surface, film cooling over a surface is a three-temperature problem (Figure 2.2). The three temperatures involved are the mainstream temperature (T_m), the coolant temperature (T_c) and the wall temperature (T_w). In film-cooling situations, the mainstream temperature in equation (2) must be replaced by a film temperature (T_f), which is a mixed temperature between the mainstream temperature between the mainstream and coolant temperatures. The film temperature depends on the local mixing between the two streams. In this case, the heat flux into the surface is

$$q_f'' = h_f (T_f - T_w)$$

In the event, that the surface is adiabatic, then the film temperature will be equal to the adiabatic wall temperature. There are two unknowns in the above equation, the heat transfer coefficient (h_f) and film temperature (T_f).

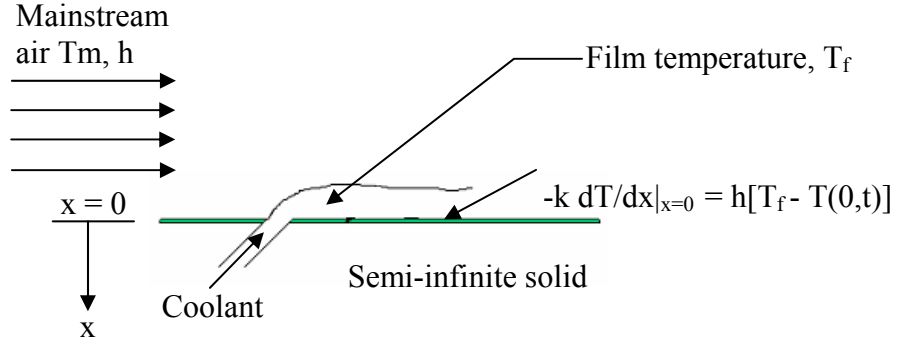


Figure 2.2: Film cooling over a flat plate

To find the unknown T_f in terms of known quantities T_m and T_c , a non-dimensional temperature is defined as the film-cooling effectiveness (η).

$$\eta = \frac{T_f - T_m}{T_c - T_m}$$

$$\text{Or } T_f = \eta(T_c - T_m) + T_m = \eta T_c + (1 - \eta)T_m \quad (3)$$

Note that the highest and lowest value of the film-cooling effectiveness can be 1 and 0 respectively. When the film temperature (T_f) is same as the mainstream temperature (T_m), film-cooling effectiveness (η) equals the value of 0 and when the film temperature (T_f) is same as the coolant temperature (T_c), film-cooling effectiveness (η) equals the value of 1.

Replacing T_m in Equation (2) by T_f from equation (3), the following equation in terms of two unknowns, h and η is obtained.

$$T_w - T_i = \left[1 - \exp\left(\frac{h^2 \alpha t}{k^2}\right) \operatorname{erfc}\left(\frac{h\sqrt{\alpha t}}{k}\right) \right] \times [\eta T_c + (1 - \eta)T_m - T_i] \quad (4)$$

The above equation assumes a step change in coolant temperature, which is not true in the transient experiment. Therefore, the above equation was modified to represent the response

of the changing coolant temperature. The coolant temperature rise is simulated as a superposed set of elemental steps using the Duhamel's superposition theorem. Metzger and Larson [37] showed that the wall temperature response can be represented as

$$T_w - T_i = \sum_{j=1}^N U(t - \tau_j) \Delta T_c \quad (5)$$

where

$$U(t - \tau_j) = 1 - \exp\left[\frac{h^2}{k^2} \alpha(t - \tau_j)\right] \operatorname{erfc}\left[\frac{h}{k} \sqrt{\alpha(t - \tau_j)}\right] \quad (6)$$

The superposition is imposed by measuring the coolant temperature (T_c) variation with time (τ) during the transient test. The step changes are then input into the equation (4) to obtain the unknown heat transfer coefficient and film effectiveness.

To obtain both the heat transfer coefficient (h) and film-cooling effectiveness (η), it is necessary to obtain two equations with two unknowns (h and η) and solve for h and η . Vedula and Metzger [38] presented a method wherein two color change times can be obtained from a single transient test at every location. During the transient test, the liquid crystal coating indicates one surface temperature (T_{w1}) at time, t_1 and another surface temperature (T_{w2}) at time, t_2 . Basically, two events are measured at every point leading to the solution of both h and T_f from the simultaneous solution of the two equations:

$$\begin{aligned} \frac{T_{w1} - T_i}{T_f - T_i} &= 1 - \exp\left(\frac{h^2 \alpha t_1}{k^2}\right) \operatorname{erfc}\left(\frac{h \sqrt{\alpha t_1}}{k}\right) \\ \frac{T_{w2} - T_i}{T_f - T_i} &= 1 - \exp\left(\frac{h^2 \alpha t_2}{k^2}\right) \operatorname{erfc}\left(\frac{h \sqrt{\alpha t_2}}{k}\right) \end{aligned} \quad (7)$$

Ekkad et al. [39] and Du et al. [40] used a transient cooling technique to eliminate the use of superposition integration for the mainstream and coolant temperatures but they still needed two

different tests to obtain both heat transfer coefficient and film effectiveness at every point on the surface

In the present study, a transient infrared thermography technique described by Ekkad [41] will be used to obtain both heat transfer coefficient and film effectiveness from a single test. The transient IR technique is based on the two equations, single test proposed by Vedula and Metzger [36]. In this test, two images with surface temperature distributions are captured at two different times during the transient test. The two temperatures at two different instants are used in the two equations (Eq. 7) shown above to calculate both heat transfer coefficient and film temperature.

A new term called net heat flux ratio is used to measure the combined effect of film effectiveness and heat transfer coefficient. Net heat flux ratio is the ratio of heat flux to the surface with film injection to the heat flux without film injection. If the value is less than one that means surface is being benefited by film cooling and the opposite is true if the value is greater than one. Net heat flux ratio is expressed as

$$\frac{q''}{q''_0} = \frac{h}{h_0} \left(1 - \frac{\eta}{\phi} \right)$$

Where,

h = heat transfer coefficient with film injection

h_0 = heat transfer coefficient without holes

η = film cooling effectiveness

ϕ = overall cooling effectiveness, $(T_f - T_c)/(T_m - T_c)$

q'' = heat flux with film injection

q''_0 = heat flux without film holes

Another term called blowing ratio, M is used to measure amount of coolant being injected in comparison to mainstream flow. It is defined as the ratio of the mass flux of the

coolant to the mass flux of the mainstream or

$$\text{Coolant-to-mainstream blowing ratio, } M = \frac{\rho_c U_c}{\rho_m U_m}$$

Where,

ρ = density of fluid

and U = Velocity of fluid

The subscript c stands for coolant and m for mainstream. The higher the blowing ratio, the more is the coolant mass flux and blowing ratio, $M=0$ represents no injection case. In our case, this blowing ratio is called global blowing ratio because it is based on velocity of the mainstream at the inlet of the cascade. But actual or local blowing ratio for each hole is more than likely different than the global blowing ratio. The reason is that the amount of coolant coming out from each hole depends on the difference between plenum pressure and local static pressure. If pressure difference is higher, more coolant will come out i.e. higher blowing ratio and vice versa.

Local blowing ratio is an important parameter because it gives us the local picture of coolant and leakage flow interaction. The equation (8) is used to calculate actual mass flow rate of coolant coming out through each hole [42]

$$\dot{m} = C_D P_{tc} \left(\frac{P_m}{P_{tc}} \right) \sqrt{\frac{2k}{(k-1)RT_{tc}} \left(\left(\frac{P_{tc}}{P_m} \right)^{\frac{k-1}{k}} - 1 \right)} \frac{\pi}{4} d^2 \quad (8)$$

Where

\dot{m} = Actual mass flow rate of coolant.

C_D = Discharge coefficient or the ratio of actual mass flow rate to ideal mass flow rate through the film cooling hole.

P_{tc} = Total pressure of coolant inside plenum

P_m = Static pressure of mainstream

k = Specific heat ratio

R = Gas constant

T_{tc} = Total temperature of coolant inside plenum

d = Diameter of film cooling hole

Equation (8) assumes an isentropic one-dimensional expansion from the total pressure in the coolant loop to the static pressure in the primary or mainstream. For present study, static pressure measured on the floor of the plenum is used as the total pressure of coolant. It can be safely assumed in our case that static and total pressures inside the plenum are same because plenum acts as a reservoir. Static pressure inside the plenum is measured at two places on the floor and no significant difference in pressure readings were found. It shows that coolant flow equalizes well inside the plenum.

For tip injection cases, static pressure measured on the shroud along the camber line is used as the static pressure of the mainstream, P_m . As static pressure taps on the shroud are not located exactly on top of the film cooling holes on the blade tip, linear interpolation is used to measure mainstream static pressure, P_m for each hole. For pressure side injection cases, static pressure measured on the 86.7% of the blade span (please see Figure 5.2) on the pressure surface (not tip) of the blade for no injection is used as the mainstream static pressure. As pressure side taps on the shroud are located 6.35 mm upstream of the actual pressure surface of the blade, shroud pressure data were not used as mainstream static pressure. In addition, linear interpolation is used for these cases. Due to the above-mentioned assumptions, local blowing ratios calculated are just estimated values. But as will be seen later, local blowing ratios calculated this way provides good insights to the heat transfer data.

For every case, all the variables in equation (8) are known except discharge coefficient, C_D . First of all, same value of C_D is assumed for all holes and the value is altered until the summation of mass flow rates coming out from each hole equals the experimental mass flow rate.

2.2 Analysis of Semi-Infinite Solid Assumption

In order to verify the validity of the semi-infinite solid assumption, a two-dimensional transient analysis is performed with ANSYS[®] software. Blade geometry used for the analysis is a section between the leading and trailing edges. The transient analysis lasts for thirty seconds, which corresponds to the average test duration. The finest mesh for this analysis contained 12,659 elements. Boundary conditions are as follows: heat transfer coefficients of 800, 1000, 1300 W/m² K on the tip, pressure side and suction side respectively, the free stream temperature is 288 °K, and the initial blade temperature is 383 °K. These temperatures represent the actual test temperatures. Graphs were obtained for three locations, which extend 12.7mm into the blade, which represents the center of the plexiglas piece. As illustrated in Figure 2.3, Line 1 is close to suction side, line 2 is at the center and line 3 is close to pressure side.

Figure 2.4 shows the temperature variation with time for the middle line. Each colored line represents a point at certain depth as shown in Figure 2.3. The bottom most line in the graph represents the point at the tip. As expected, the temperature for this point changes very rapidly with time. The important point to note that the center temperature almost did not change at all within the first 30 seconds. It shows that the heat conduction did not reach even half of the thickness of the plexiglas piece. This shows the validity of our semi-infinite solid assumption

Figure 2.5 presents the temperature response in the Plexiglas near the suction side. The center temperature drops 20 °K in 30 seconds due to high heat transfer coefficient on the suction

side. Note that during a typical heat transfer test, color change over most of the blade tip occurs within the first five to twenty seconds, so the calculations in the high heat transfer regions are not as affected by temperature penetration. The blade tip temperature drops significantly. All other temperatures, at point between the center and tip, drop slightly more than the center temperature. The temperature penetration into the plexiglas test section is insignificant. Figure 2.6 presents the temperature response in the plexiglas near the suction side. Results in Figure 2.6 are similar to those in Figure 2.5, but the temperature drop is slightly lower.

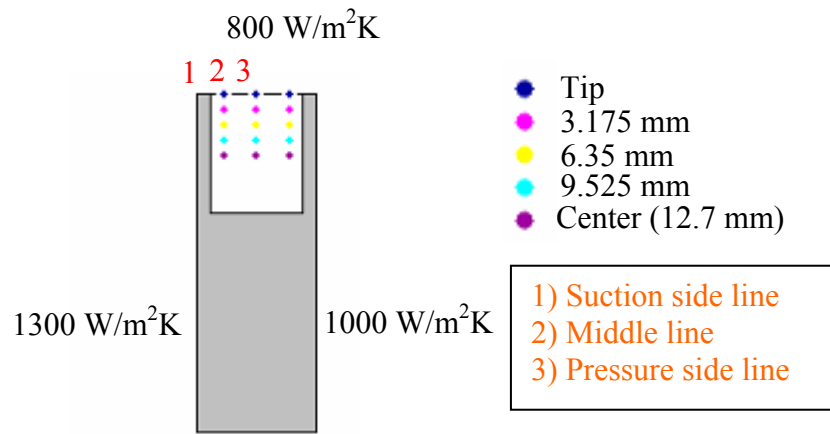


Figure 2.3: Boundary conditions

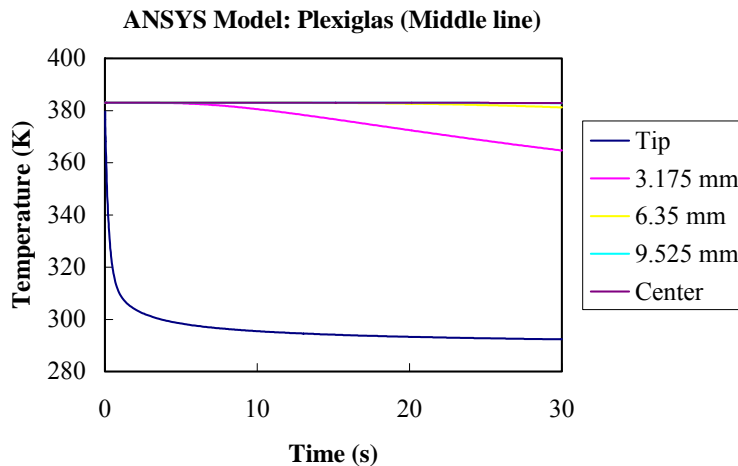


Figure 2.4: Temperature variation with time at various depths for Middle line

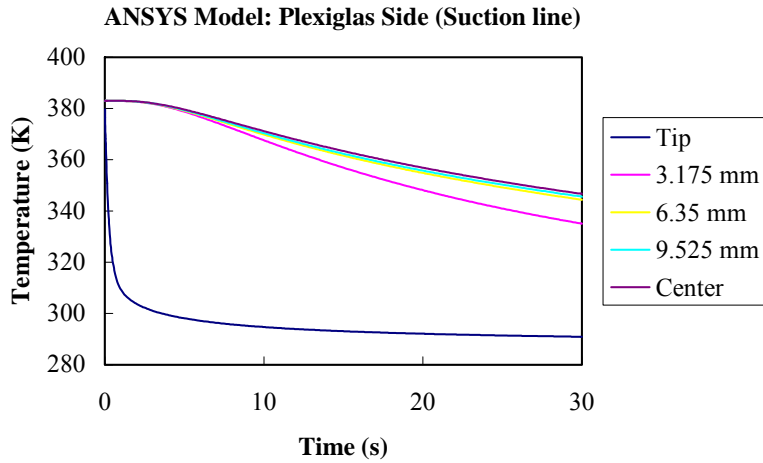


Figure 2.5: Temperature variation with time at various depths for Suction sideline

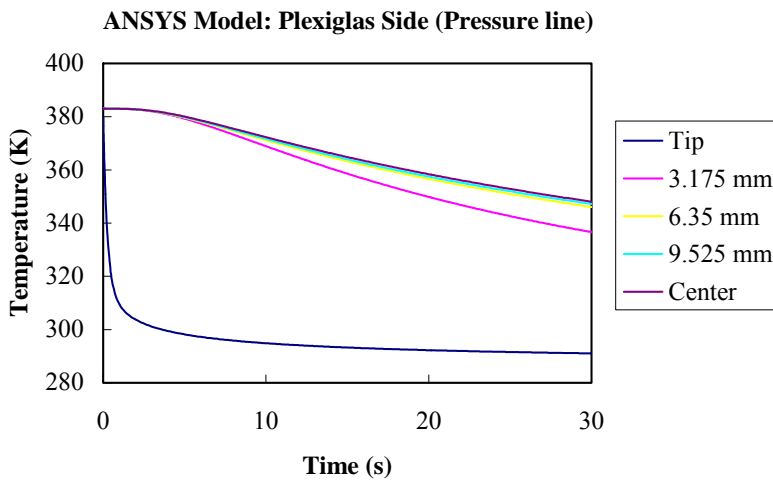


Figure 2.6: Temperature variation with time at various depths for Pressure sideline

CHAPTER 3

3.1 Experimental Methods

Two types of data will be presented, static pressure distribution on the shroud and heat transfer coefficients as well as film effectiveness data on the blade tip. Pressure data will help to indicate the leakage flow behavior and path. Static pressure distributions on the shroud also help us explain the heat transfer data. On the other hand, heat transfer data will give us idea about the thermal loading on the blade tip. A transient liquid crystal technique will be used to calculate heat transfer coefficients for uncooled blade tip and infrared (IR) thermography will be used to measure heat transfer coefficient and film effectiveness for blade tips with film cooling. First, a little background on liquid crystal and IR thermography will be presented. Then experimental procedure relating pressure test and heat transfer test will be described. In the end, the theory behind the transient liquid crystal technique and transient infrared thermography will be explained.

3.2 Liquid Crystal Fundamentals

Liquid crystals are highly anisotropic fluids that exist between the boundaries of the solid phase and the conventional, isotropic liquid phase. The liquid crystals are referred to as thermochromic since they reflect different colors selectively when subjected to temperature changes. Liquid crystal has helical structure that expands, shrinks or rotates when temperature varies. This structure change causes the liquid crystal to selectively reflect the incident white light and reveal various colors at different temperatures. The color change for the Thermochromic Liquid Crystals (TLC) ranges from clear at ambient temperature, through red as temperature increases and then to yellow, green, blue and violet before turning colorless (isotropic) again at higher temperature. The color-temperature play interval depends on the TLC

composition. The bands can be selected of about 0.5°C to 20°C and working temperature of -30°C to above 120°C . That means, the appearance of red can be any temperature between -30°C to 120°C and the change of color from red to blue can be within 0.5°C to 20°C . These color changes are repeatable and reversible as long as the TLC's are not physically or chemically damaged. Depending on material viscosity, the response time of TLC varies from 5 milliseconds to seconds. Accuracy of $\pm 0.1^{\circ}\text{C}$ may be readily achieved for measuring surface temperature.

Pure liquid crystal materials are thick, viscous liquids, greasy and difficult to deal with under most heat transfer laboratory conditions. The TLC material is also sensitive to mechanical stress. These problems are overcome by using encapsulated liquid crystals, which are liquid crystal enclosed in protective 5 to 10 μm diameter capsules suspended in a sprayable binder material. For surface temperature measurements application, the unencapsulated material to a clear plastic sheet and sealing it with a black backing coat to form a pre-packaged assembly is used.

1) Transition Temperature Calibration

The temperature at which color change from red to green occurs for liquid crystal get altered if liquid crystal is subjected to ultraviolet rays or when it ages. So, calibration is needed before running any test. For the calibration purpose, a thermocouple is placed on the liquid crystal sheet. Camera is focused on the liquid crystal sheet and a tiny area is selected including the thermocouple tip. Heater is turned on to heat up the liquid crystal sheet and frame grabber board is also turned on through the software so that the time at which any point near the thermocouple changes color from red to green will be detected and written on a file. Data logger for thermocouple is also turned on along with the heater. This data logger writes the time and corresponding temperature in a file. When liquid crystal sheet become colorless after changing

color, the test is stopped. Then the time from the start of the test at which color change took place is read from the frame grabber board file. Liquid crystal color change temperature is the temperature in the temperature data file, which corresponds to the same time that is read from the frame grabber board.

The advantages of using liquid crystals are as follows:

- 1) Continuous temperature distribution of the surface
- 2) No thermocouple wiring
- 3) Non-intrusive test
- 4) No need to interpolate or extrapolate data
- 5) Applicable on both stationary and moving surfaces
- 6) Better accuracy than thermocouple

The limitations of using liquid crystals are as follows:

- 1) It is not suitable for high temperature applications
- 2) Because of its reflection nature, liquid crystal thermograph may be sensitive to viewing angle and illuminating light strength.
- 3) The color response degrades by chemical contamination and exposure to ultraviolet radiation.

3.3 Infrared Thermography Fundamentals

All bodies at a temperature above absolute zero emit thermal radiation in all wavelengths in all possible directions into space. Thermal radiation refers to radiation energy emitted by bodies because of their temperature. According to Maxwell's electromagnetic theory, radiation is treated as electromagnetic waves. The electromagnetic spectrum is divided arbitrarily into a number of wavelength regions, called bands, distinguished by the methods used to produce and

detect radiation. Figure 3.1 shows such subdivisions of the electromagnetic wave spectrum. There is no fundamental difference between radiation in the different bands of the electromagnetic spectrum. They are all governed by the same laws and the only differences are those due to differences in wavelength.

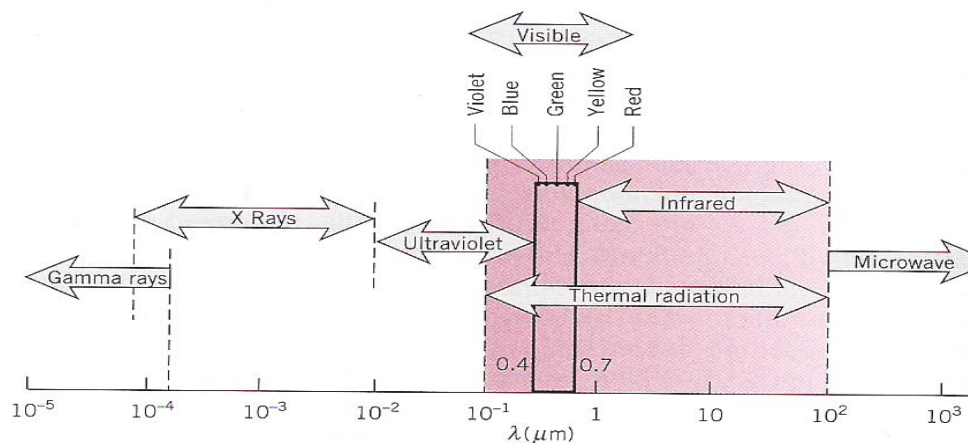


Figure 3.1: Electromagnetic spectrum of radiation [36]

Infrared Thermography makes use of the infrared spectral band. At the short-wavelength end, the boundary lies at the limit of visual perception. Whereas at the long-wavelength, it merges with the microwave radio wavelengths. The infrared band is often further subdivided into four smaller bands, the boundaries of which are also arbitrarily chosen. They include: the near infrared ($0.75\text{-}3 \mu\text{m}$), the middle infrared ($3\text{-}6 \mu\text{m}$), the far infrared ($6\text{-}15 \mu\text{m}$) and the extreme infrared ($15\text{-}100 \mu\text{m}$).

Thermal radiation emitted by a surface encompasses a range of wavelengths. As shown in Figure 3.1, the magnitude of the radiation varies with wavelength and the term spectral is used to refer to the nature of this dependence. Emitted radiation consists of a continuous, non-uniform distribution of monochromatic (single-wavelength) components. Radiation emitted by a surface

can also be directional as shown Figure 3.2. To properly quantify radiation heat transfer, both spectral and directional effects should be taken into account.

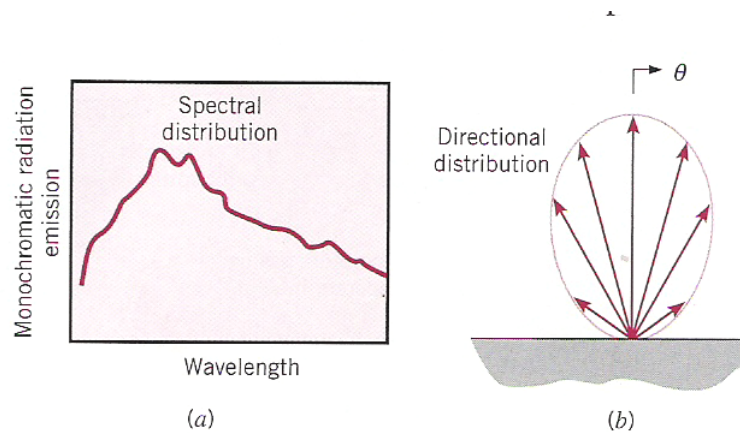


Figure 3.2: Radiation emitted by a real surface. (a) Spectral distribution (b) Directional distribution [36]

When describing the radiation characteristics of real surfaces, it is useful to introduce the concept of a blackbody. A blackbody is considered to absorb all incident radiation from all directions at all wavelengths without reflecting, transmitting or scattering it. For a given temperature and wavelength, no other body at the same temperature can emit more radiation than a blackbody. The radiation emission by a blackbody at any temperature T is the maximum possible emission at that temperature.

So far, only blackbody radiators and blackbody radiation have been discussed. However, real objects almost never comply with these laws over an extended wavelength region –although they may approach the blackbody behavior in certain spectral intervals. Figure 3.3 shows the difference between the blackbody and real surface radiation.

There are three processes, which can occur that, prevent a real object from acting like a blackbody: a fraction of the incident radiation α may be absorbed, a fraction ρ may be reflected, and a fraction τ may be transmitted. Since all of these factors are more or less

wavelength dependent, the subscript λ is used to imply the spectral dependence of their definitions. Thus

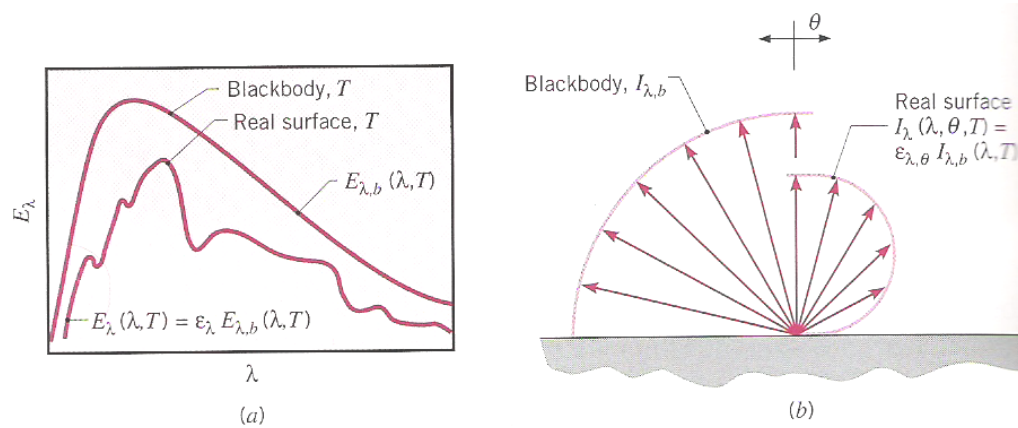


Figure 3.3: Comparison between blackbody and real surface emission. (a) Spectral distribution (b) Directional distribution [36]

The spectral absorptance α_λ = the ratio of the spectral radiant power absorbed by an object to that incident upon it.

The spectral reflectance ρ_λ = the ratio of the spectral radiant power reflected by an object to that incident upon it.

The spectral transmittance τ_λ = the ratio of the spectral radiant power transmitted through an object to that incident upon it.

The sum of these three factors must always add up to the whole at any wavelength, so we have the relation:

$$\alpha_\lambda + \rho_\lambda + \tau_\lambda = 1$$

For opaque materials $\tau_\lambda = 0$ and the relation simplifies to:

$$\alpha_\lambda + \rho_\lambda = 1$$

Another factor, called the emissivity, is required to describe the fraction ϵ of the radiant

emittance of a blackbody produced by an object at a specific temperature. Thus, we have the definition:

The spectral emissivity ε_λ = the ratio of the spectral radiant power from an object to that from a blackbody at the same temperature and wavelength. Expressed mathematically, this can be written as the ratio of the spectral emittance of the object to that of a blackbody as follows:

$$\varepsilon_\lambda = \frac{W_{\lambda,o}}{W_{\lambda,b}}$$

Generally speaking, there are three types of radiation source, distinguished by the ways in which the spectral emittance of each varies with wavelength.

A blackbody, for which $\varepsilon_\lambda = \varepsilon = 1$

A graybody, for which $\varepsilon_\lambda = \varepsilon = \text{constant less than 1}$

A selective radiator, for which ε varies with wavelength

According to Kirchoff's law, for any material the spectral emissivity and spectral absorptance of a body are equal at any specified temperature and wavelength. That is:

$$\varepsilon_\lambda = \alpha_\lambda$$

From this we obtain, for an opaque material (since $\alpha_\lambda + \rho_\lambda = 1$):

$$\varepsilon_\lambda + \rho_\lambda = 1$$

For highly polished materials ε_λ approaches zero, so that for a perfectly reflecting material (*i.e.* a perfect mirror) we have:

$$\rho_\lambda = 1$$

When viewing an object, the camera receives radiation not only from the object itself; it also collects radiation from the surroundings reflected via the object surface. Both these radiation

contributions become attenuated to some extent by the atmosphere in the measurement path. Also, radiation contribution comes from the atmosphere itself. To measure temperature accurately, it is therefore necessary to compensate for the effects of a number of different radiation sources. This is done on-line automatically by the camera. The following object parameters must, however, be supplied for the camera [44]:

The object emittance, ε

The relative humidity

Transmittance of the atmosphere, τ_{atm}

Object distance

The effective temperature of the object surroundings, or the reflected ambient temperature T_{refl}

The temperature of the atmosphere T_{atm}

Among all the parameters: the relative humidity and object distance are easy to provide. The two temperatures are less of a problem provided the surroundings does not contain large and intense radiation sources. If the atmosphere is air (like in our case), then we can safely assume the transmittance of atmosphere as 1. A new parameter will replace τ_{atm} if the IR camera sees through a IR transparent window. In our case, we used Zinc-Selenide window and the transmittance of the window was 0.72. There is also a way to find out the transmittance of the window and the emittance of the object experimentally that will be explained in the following two paragraphs.

1) Emissivity Calibration

The blade tip was painted with flat black paint first. When the paint dried, the blade was heated up for one and a half hours so that the Plexiglas reaches the steady state temperature.

During the heating, the Plexiglas temperature was checked every fifteen minutes. Then a reference point was selected and its temperature was measured using a thermocouple. After that the emissivity was altered until the temperature measured by the camera agrees with the thermocouple reading. This is the emissivity value of the reference object. However, the temperature of the reference object must not be too close to the ambient temperature for this to work. During the emissivity calculation, Zinc-Selenide window was not used. So, the transmissivity value used was 1.

2) Transmissivity Calibration

Now to find out the transmissivity of the window, we again heat up the blade until it reached steady state temperature. Then a reference point was selected and a thermocouple was used to measure its temperature. Then the camera was focused on the surface so that the camera sees through the Zinc-Selenide window. The emissivity of the surface found previously was used as the emissivity of the surface and also the temperature of the window was entered. After that the transmissivity of the external optics (i.e. window) was altered until the temperature measured by the camera and by the thermocouple matches perfectly. The transmissivity found by this technique and the transmissivity value of the window supplied by the manufacturer matches exactly.

There are many advantages of this new technique.

- 1) There is no need for spraying expensive liquid crystals on the surface. Typical surface preparation requires only black paint.
- 2) The experiment does not require two experiments thus reducing run time and also uncertainties relating to running two different tests at two different times.
- 3) The test is not limited by the operating point of the liquid crystals. Liquid crystals

cannot operate beyond 50°C whereas the present technique has no such limits as long as the test plate material is made of low conductivity.

- 4) The IR camera also provides initial temperature distribution on the surface, which is very difficult to obtain from liquid crystals.
- 5) The coolant does not require to be heated as in the case of two test techniques resulting in reduced capital costs and timesaving.

3.4 Pressure Test

Pressure measurements are made on the shroud for each configuration. As mentioned earlier, static pressure data are taken for three rows of holes. First row of holes are 6.35 mm away from the pressure side, second row of holes are along the camber line and third row of holes are 6.35 mm away from the suction side. First row gives us idea about the flow before it enters the tip section; the second row shows the flow condition inside the tip and third row gives us idea about the flow when it leaves the tip section.

The pressure system needs 86.18 KPa (125 psi) of supply pressure to drive internal valves. Moisture is blown from the pressure system data ports using the supply pressure before each test. Prior to the actual test, the data ports are calibrated and reset to zero to ensure accuracy. Tubes connected to the shroud are tightly plugged into the Pressure System data ports. Each tube is tested to ensure no leakage at the point of connection, and to make sure there are not torn or frayed.

The compressor is then turned on and the supply tank is filled until it reaches 1,896,058 Pa (275 psi). The same pressure is used for each experiment. Because of the short duration of the test, the tank never fully empties. The pneumatic valve is then opened and air enters the test rig. The duration of all pressure tests matched that of the heat transfer tests. The pressure

system reads static pressures and outputs a large data file, which gives data in the form of an Excel spreadsheet.

3.5 Heat Transfer Test

Two types of heat transfer test are run. The first type is for when only heat transfer coefficients (HTC) are measured on the blade tip. This will be called HTC test. The second type is for when both heat transfer coefficients and film effectiveness are measured. This will be called film-cooling test. Basically, both types of test are similar. In both cases, the heat transfer blade is heated for two hours until it reaches steady temperature and then mainstream air is allowed into the test section to cool the blade. During the cooling, the time of liquid crystal color change is captured. But, in film-cooling test, because of two unknown variables (heat transfer coefficients and film effectiveness), two tests are run for each case and also film-cooling air of known temperature is injected through the film cooling holes on the blade tip.

1) HTC Test

Heat transfer blade is heated for two hours to ensure that its temperature reaches steady state before testing. During heating, thermocouples are used to monitor the blade internal and external temperature. These thermocouples are checked every 5-15 minutes. Four thermocouples are placed on top of the liquid crystal sheet. One thermocouple is placed near the leading edge, one near the trailing edge and the other two in-between. All the thermocouples are placed along the mean camber line. When steady state temperature is reached, the temperatures of all four thermocouples are noted down and then they are removed just before the test is run. Basically the whole blade tip is divided into four regions and the temperature of each thermocouple is used as the initial temperature of the corresponding region for the calculation purpose. This was done to take into account the non-uniformity of the temperature of the

plexiglas piece.

Once the blade is at steady state, the camera is focused on the heat transfer blade tip. Lights are also focused on the test surface to illuminate the tip surface for color capture. A region of interest or ROI (a rectangular area covering the whole blade tip) is selected using the image processing software Optimas[®]. This region of interest is the same for all heat transfer tests. Background intensity is set to ensure that lighting is uniform. A threshold is set to indicate the onset of actual color change during the transient test.

The compressor is run and the supply tank is filled to 1.89 MPa (275 psig). Note that the same pressure is used for each experiment. Although air leaves the tank, the short duration of test ensures that the tank never fully empties. The heaters are switched off, and the pneumatic valve is then opened so that air may enter the test rig. A thermocouple measures the mainstream temperature during the test. The experiment ends when the entire surface area changes color to red. The experiment takes 15 – 45 seconds to complete.

2) Film-Cooling Test

Most of the steps mentioned above are also executed in film-cooling test. One major difference is that we used infrared (IR) camera instead of a RGB camera and also some extra steps were carried out which will be mentioned now. Thirty minutes before the actual test is run, the film cooling air is turned on and diverted away from the test section. Flow rate of the coolant is set. At the same time, heater starts heating up the coolant. A thermocouple monitors the temperature of the exiting air. As the air temperature reaches steady state, preparations are made to run the actual test. Coolant air is allowed into the plenum approximately two seconds before the mainstream air enters the test section. This was done to ensure the synchronization. A thermocouple inside the plenum measures the coolant temperature before it exits out through the

holes. This temperature is used as the coolant temperature for the calculation.

As mentioned earlier both heat transfer coefficient and film effectiveness were calculated from a single test. All the parameters needed for IR camera such as atmosphere temperature, object distance, transmittance of the window, emissivity of the surface, relative humidity of air were entered through the software for IR camera. The camera is set to capture and record the thermal image of the surface every five seconds after the test was initiated. The software also writes down the time at which each image was captured. The first image is used as the initial temperature of the surface; the image at ten seconds and twenty seconds were used in two equations (Eq 7).

3.6 Uncertainty Analysis

In order to determine the accuracy of this study, an error analysis is preformed using the methodology of Kline and McClintock [43]. The three basic steps of measuring uncertainty related to a particular experiment are as follows

1. Estimate the uncertainty interval for each measured quantity
2. State the confidence limit on each measurement
3. Analyze the propagation of uncertainty into results

Suppose that independent variables $x_1, x_2 \dots x_n$ are measured in the laboratory. The measurements are used to calculate some result, R for the experiment. In general R may be expressed mathematically as

$$R = R(x_1, x_2 \dots x_n)$$

A variation, δx_i , in x_i would cause variation δR_i in R

$$\delta R_i = \frac{\partial R_i}{\partial x_i} \delta x_i$$

The relative variation in R is

$$\frac{\partial R}{R} = \frac{1}{R} \frac{\partial R}{\partial x_i} \partial x_i = \frac{x_i}{R} \frac{\partial R}{\partial x_i} \frac{\partial x_i}{x_i}$$

Now we have to express relative uncertainty in R caused by the combined effects of the uncertainties in all the x_i s. It is shown that the best representation for the relative uncertainty of the result is

$$u_R = \pm \left[\left(\frac{x_1}{R} \frac{\partial R}{\partial x_1} \frac{\partial x_1}{x_1} \right)^2 + \left(\frac{x_2}{R} \frac{\partial R}{\partial x_2} \frac{\partial x_2}{x_2} \right)^2 + \dots \dots \dots \left(\frac{x_n}{R} \frac{\partial R}{\partial x_n} \frac{\partial x_n}{x_n} \right)^2 \right]^{1/2}$$

The method explained above is the standard procedure to measure uncertainty of the result from a single test. To apply this method, we have to express the result in terms of the variables first. The equation that we used to calculate heat transfer coefficient for flow over a flat plate is

$$\frac{T_w - T_i}{T_m - T_i} = 1 - \left[\exp\left(\frac{h^2 \alpha t}{k^2}\right) \right] \left[\operatorname{erfc}\left(\frac{h\sqrt{\alpha t}}{k}\right) \right]$$

Or $h = f(T_w, T_i, T_m, \alpha, k, t)$

In the above equation, h is present in both exponential and error function. It is not possible to express h in the above equation to express in terms of other variables. So, the following procedure is used to find out relative uncertainties in calculating h.

First a conservative error estimate of the measured quantities was done. Then the relative uncertainties in measured quantities were calculated. Finally, the average uncertainties of the results were calculated by taking the square root of the summation of the square of all the relative uncertainties.

Error estimates of each variable are as follows

$$T_w = 32.3 \pm 0.2 \text{ }^\circ\text{C}$$

$$T_i = 70 \pm 2 \text{ }^\circ\text{C}$$

$$T_m = 20 \pm 0.2 \text{ }^\circ\text{C}$$

$$t = 8 \pm 0.125 \text{ seconds}$$

Here, α and k are tabulated values. As a custom, 3 percent relative uncertainty is assumed for both variables. The relative uncertainties of the rest of the four variables are

$$UT_w = 0.2 / 32.2 = 6.192\text{E-}3$$

$$UT_i = 2 / 70 = 0.029$$

$$UT_m = 0.2 / 20 = 0.01$$

$$Ut = 0.125 / 8 = 0.016$$

$$U\alpha = Uk = 0.03$$

The root mean square uncertainty in calculating heat transfer coefficient over flat plate, h is

$$U_h = \sqrt{(UT_w)^2 + (UT_i)^2 + (UT_m)^2 + (Ut)^2 + (U\alpha)^2 + (Uk)^2}$$

$$U_h = 0.055 \text{ or } 5.5 \%$$

In Appendix II, uncertainty in calculating h using maximum deviation of all variables in the positive direction is shown. It appears that 5.5 % uncertainty calculated above is a conservative value in comparison to the value in Appendix II.

In calculating heat transfer coefficient for film cooling case, relative uncertainty related to coolant temperature will also be added.

$$T_{ch} = 20 \pm 0.2 \text{ }^\circ\text{C}$$

$$UT_{ch} = 0.2 / 20 = 0.01$$

So, the root mean square uncertainty in calculating heat transfer coefficient for film cooling case is

$$U_{h_{\text{film}}} = \sqrt{(UT_w)^2 + (UT_i)^2 + (UT_m)^2 + (UT_{\text{ch}})^2 + (Ut)^2 + (U\alpha)^2 + (Uk)^2}$$

$$U_{h_{\text{film}}} = 0.056 \text{ or } 5.6 \%$$

Film effectiveness was calculated using the following equation

$$\eta = \frac{T_w - T_{i,2}}{T_{c,2} - T_{m,2}} \frac{1}{F(h)} + \frac{T_{i,2} - T_{m,2}}{T_{c,2} - T_{m,2}}$$

Where,

$$F(h) = 1 - \left[\exp\left(\frac{h^2 \alpha t}{k^2}\right) \right] \left[\operatorname{erfc}\left(\frac{h\sqrt{\alpha t}}{k}\right) \right]$$

Relative uncertainty related to coolant temperature for film effectiveness calculation is

$$T_{ce} = 70 \pm 0.2 \text{ } ^\circ\text{C}$$

$$UT_{ce} = 0.2 / 70 = 2.857\text{E-}3$$

So, the root mean square uncertainty in calculating film effectiveness, η is

$$U_\eta = \sqrt{(Uh)^2 + (UT_w)^2 + (UT_i)^2 + (UT_m)^2 + (UT_{ce})^2 + (Ut)^2 + (U\alpha)^2 + (Uk)^2}$$

$$U_\eta = 0.078 \text{ or } 7.8 \%$$

The maximum uncertainty based on 2-D conduction will occur at regions close to the edges and near the holes for film cooling studies. This uncertainty in measured 'h' can be close to $\pm 9\%$ and for effectiveness can be close to $\pm 12\%$.

CHAPTER 4

4.1 Description of the Test Facility

This experiment uses a blow down test facility i.e. a big tank is filled up with compressed air first and then the tank is emptied during a short duration. The test rig was designed to produce the required pressure ratio across the blade for a short duration. The entire setup is made of Medium Carbon Steel of 3.175-mm thickness. The whole test facility is shown in Figure 4.1 and can be divided into four sections: 1) Compressor and the inlet valves 2) Diverging-Converging section 3) Test Section 4) Coolant Supply

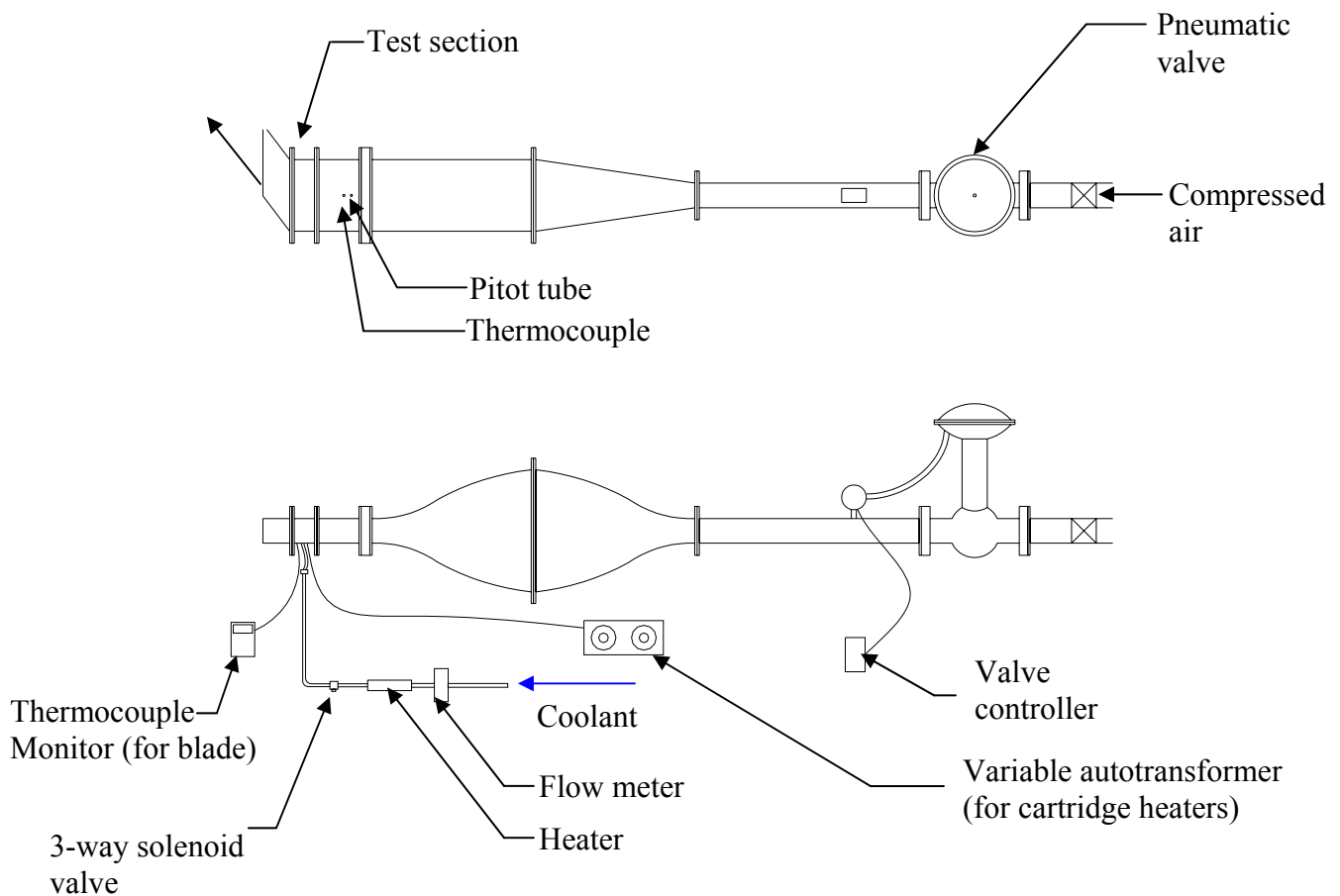


Figure 4.1: Experimental set up

1) Compressor and Inlet Valve

An Atlas Copco[®] GR110 compressor equipped with a Pneumatech Inc. air dryer is used as the source of mainstream air supply. The compressor supplies air to a large tank capable of holding 7.571-m³ of high-pressure air. This system is capable of generating a steady flow rate of 0.5 kg/s.

The air is delivered to the test section through a 10.16-cm diameter pipe. Air first passes through a gate valve. The gate valve allows the entire wind tunnel to be isolated from the supply tank. Downstream from that valve is a large pneumatically actuated Fisher control valve, which is shown in Figure 4.2. A Fisher-Rosemount DPR 960 controller regulates the pneumatic valve. The controller allows one to set the valve and maintain a specified valve opening and/or operating pressure in the test section.



Figure 4.2: Pneumatic valve

2) Diverging-Converging Section

Figure 4.3 shows the diverging-converging section. The inlet of the diverging section is 10.16-cm by 10.16-cm and the width and height of the exit section are 0.28-m and 0.406-m respectively. The length of the section is 0.61-m. To allow for a smooth transition of height and width, all the walls are made on a 4th order polynomial curve. The rectangular diverging section is connected to the circular pipe via an entrance section that changes area from circular on one end to rectangular at the other end.

The height of the converging section changes from 0.406-m to 0.102-m, whereas the width remains the same. This change in height takes place through a distance of 0.61-m. All the sections are attached via flanges. The purpose of the diverging-converging section is to settle down the flow and make it more uniform before it enters the test section.

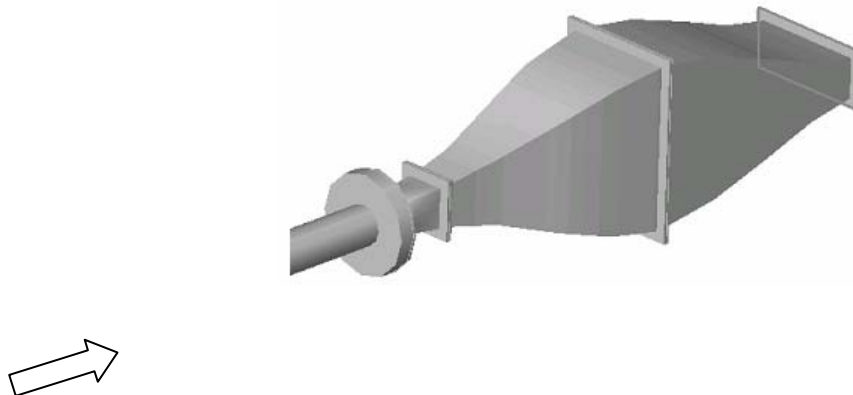


Figure 4.3: Converging-diverging section

3) Test Section

There is a 0.28-m wide, 0.102-m wide and 0.191-m long section upstream of the main test section. Holes are drilled on the top wall of this section. Thermocouples, Pitot-static probe or

hot-wires can be inserted through these holes to take temperature and velocity measurements of the incoming air.

The main test section is a linear cascade with four, two-dimensional blade tip models. Blade geometry is taken from the tip section of a General Electric HPT blade. Each blade is made of aluminum using an EDM machine, and they bolt to a steel base plate that can easily be removed from the test section. The blade spacing (S) is 95.25 mm, and the axial chord (C) is 60.02 mm. The two outer blades guide airflow around the inner blades. Inner blades are used for pressure and heat transfer measurements. All blades have a length from root to tip (H) of 76.2 mm. Figure 4.4 and Figure 4.5 (a) shows the four-blade linear cascade.

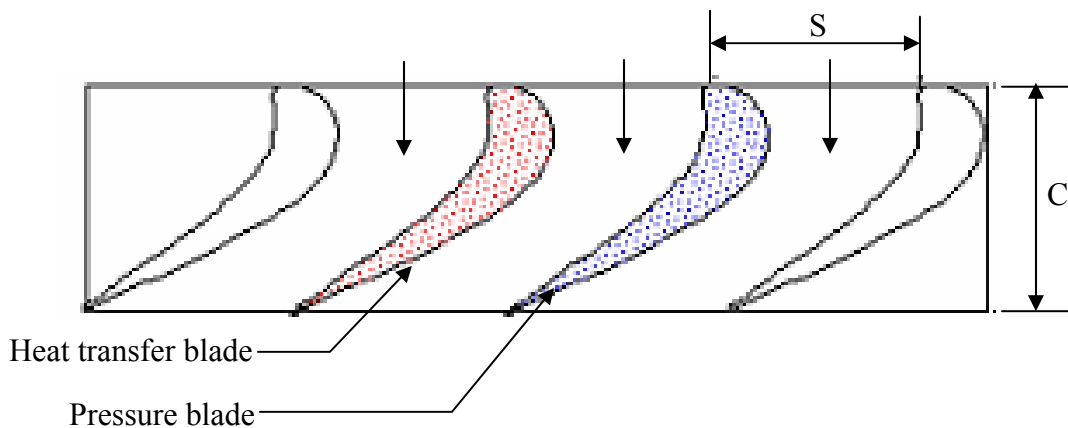


Figure 4.4: Top-view of the cascade

The third blade from the left in Figure 4.5 (a) is the pressure blade. Figure 4.5 (b) shows the static pressure taps location at different heights on blade surface. Though pressure data on the blade surface is not taken for film cooling study, local static pressure measurements (P_s/P_o) on the pressure blade (for no film cooling case) at different heights taken by Kontrovitz [46] is used for local blowing ratio calculation and is shown in chapter 5.



Figure 4.5: (a) Four bladed linear cascade, (b) Pressure blade

For this study, static pressure measurements on the shroud are also taken for each case. A special top plate with holes 6.35 mm away from the suction side, 6.35 mm from the pressure side, and along the camber line, allows pressure measurements on the stationary shroud. Camber line is the line located equal distance apart from both pressure and suction side of the blade. Figure 4.6 shows the top plate with static pressure taps.

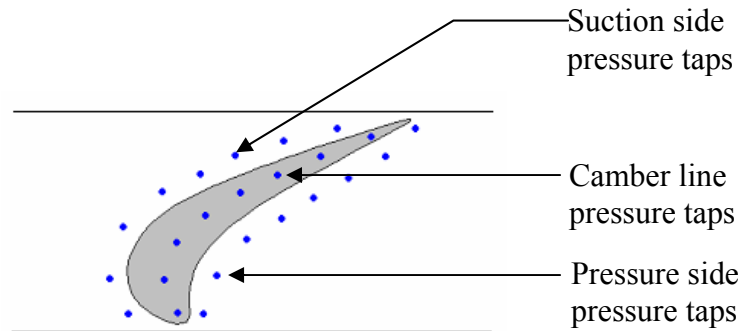


Figure 4.6: Pressure taps on the shroud

Figure 4.7 shows the heat transfer blade. The blade is made of aluminum and there is 25.4 mm recess is on the top of this blade to allow a plexiglas piece to fit in. The squealer rim, left after machining the recess, is 1.5875 mm thick. A liquid crystal sheet of the same shape as

the plexiglas piece is placed on top of the plexiglas piece. The experimental procedures involve heating the heat transfer blade to a high temperature then cooling it with compressed air in a blow down mode. The liquid crystal sheet changes color as it cools down (please see the experimental methodology section). Two Hotwatt[®] cartridge heaters are imbedded in the blade aluminum core to heat the blade. These heaters have a length and diameter of 31 mm and 6.35 mm respectively. The cartridge heaters have stainless steel sheaths and are capable of reaching temperatures up to 676 °C, however they are never operated above 110 °C during testing.

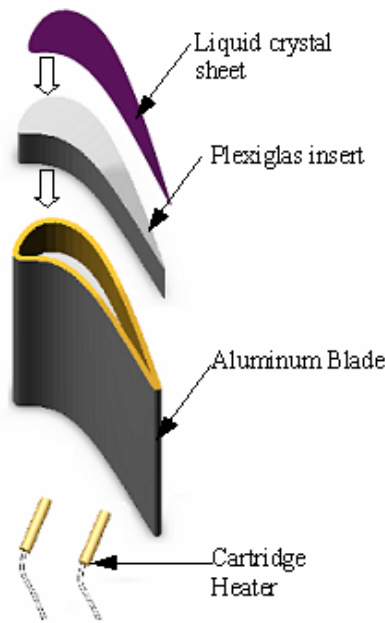


Figure 4.7: Heat transfer blade

Each heater is connected to a Staco[®] Variable Autotransformer (Figure 4.8), which allows the user to adjust the amount of current going into each heater and thereby controlling the blade temperature. A type-k thermocouple is placed between the Plexiglas insert and the aluminum blade, and additional thermocouples are placed on the blade tip. The thermocouples

are monitored to ensure that a uniform blade temperature is maintained.

The heat transfer blade shown in Figure 4.7 is used to measure heat transfer coefficient on the blade tip. The blade used for film-cooling is little bit different. The aluminum blade used is the same but the plexiglas piece is different. The plexiglas piece is shown in Figure 4.9. There are two pieces. The bottom piece has the plenum where the coolant settles down before it comes out through the holes. There are five through holes of diameter 1.524 mm along the camber. The holes are angled 90° or orthogonal to the leakage flow. The diameter of the hole is 1.524-mm. The holes are located at axial chord locations of 17, 25, 35, 55, and 74% respectively along the camber line. For recessed tip, the holes are placed at the bottom of the squealer cavity at the same locations along the camber line as for the plain tip. The second piece is 0.25 inch thick and has holes that match the holes on the bottom piece.



Figure 4.8: Variable auto-transformer

For this study, coolant injection from pressure side holes and combined cooling when coolant is injected from both tip and pressure side holes will be studied also Figure 4.10 shows 3-D model and cut away view of the blade. There are seven holes located along the pressure side of the airfoil surface. The diameter of each hole is 1.524 mm and the center-to-center distance between each hole is 6.35 mm. The first hole is located 17% of axial chord. Center of each hole

is 5.08 mm down from the tip and each hole is oriented at each location with angle of 20 degrees to the surface (70 degrees to surface normal). The angle is steep so that coolant keeps attached to the surface and also to allow drilling into the internal cooling passages. For recessed tip blade, coolant coming out through these holes also helps to cool the squealer rim.

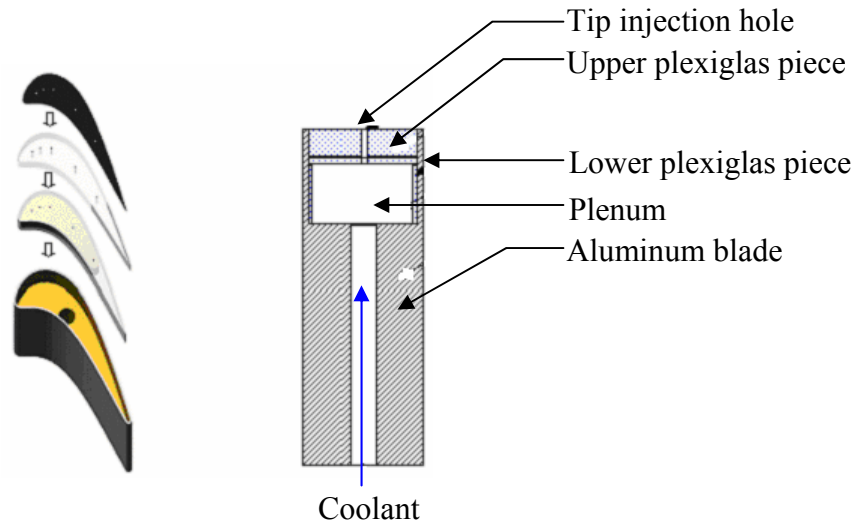


Figure 4.9: Film cooling blade

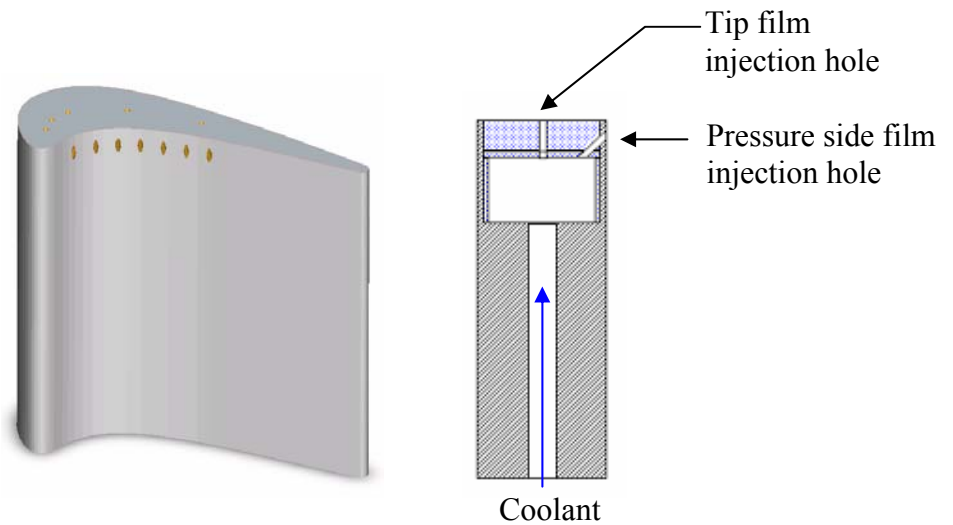


Figure 4.10: Blade used for combined cooling

The final major component is the cascade exhaust. The exhaust area is fitted with two tailboards. One tailboard is aligned with the pressure blade trailing edge and the other is aligned with the heat transfer blade. The tailboards are important because they are made adjustable and enable the user to equalize pressure in the passages adjacent to each blade and ensure periodic flow in all passages.

4) Coolant Supply

Coolant is supplied from a 0.454-m³ capacity tank, which is filled up by a Blackmer HD 602B compressor. Figure 4.11 shows the blow up view of the coolant path. A flow meter and a hotwatt heater are connected on the flow line. The flow meter measures the coolant flow rate and the heater is used to heat up the coolant. A variable autotransformer connected to the heater controls the electricity supplied to the heater thereby controls the temperature of the coolant. A three-way solenoid valve is connected downstream of the heater. Coolant is diverted away from the test section when it is being heated up. Coolant is supplied to the blade plenum via a ½ inch diameter flexible metal hose. Heater and the coolant path are wrapped with insulation to minimize the heat loss.

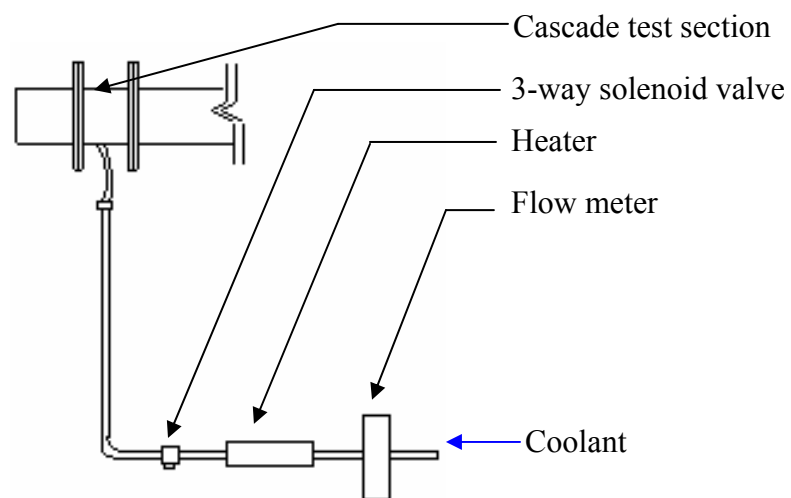


Figure 4.11: Coolant path

4.2 Test Apparatus

As mentioned earlier, static pressure on the shroud and heat transfer coefficient as well as film effectiveness over the blade tip are measured. Pressure measurement system and visual processing system for heat transfer measurement will be discussed in this section.

1) Pressure System

Figure 4.12 shows the pressure measurement system. Pressure Systems, NetScanner, Model 98RK is used for all pressure measurements. Two modules contain 32 ports. 1.5875 mm diameter tubes connect the ports and the static pressure taps on the shroud.

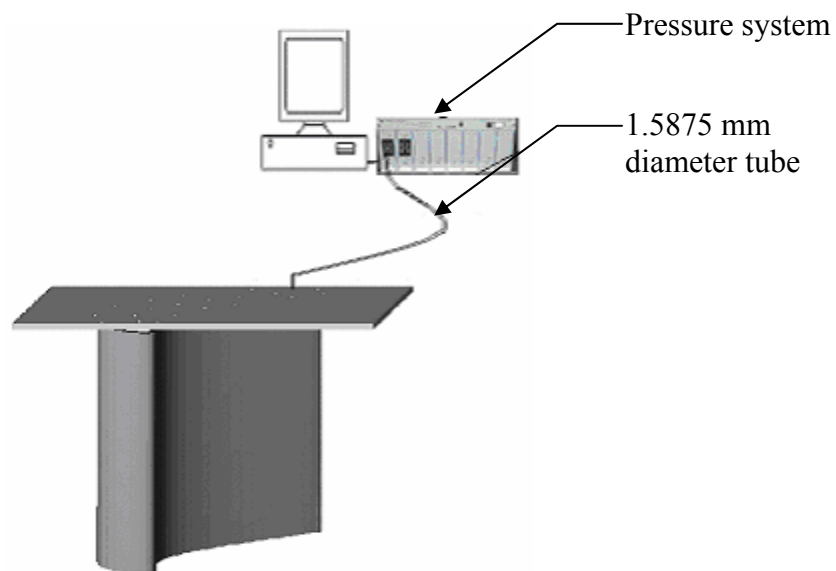


Figure 4.12: Pressure system

2) Visual Processing System

Figure 4.13 shows the schematic of the visual processing system used for transient liquid crystal method. A Pulnix RGB camera is placed right above the heat transfer blade. This camera is connected to a CFG 24-bit frame grabber board in a PC. Image processing software

(Optimas[®] v6.5) communicates with the frame grabber board. A macro allows Optimas[®] to record the time at which the liquid crystal changes from colorless to red. It produces a time file, which gives the time of change for each pixel to turn red. Thermocouples with a DAQ system was used to measure temperature. The DAQ system used is called InstruNet[®]. It read the microVolt outputs of the thermocouples, which were linked to a PC through an InstruNet[®] interface. An external box was used as the connection point for the thermocouples. This apparatus contained signal conditioning amplifiers and cold junction compensation for each channel. All the thermocouples used for the study are Type K thermocouples.

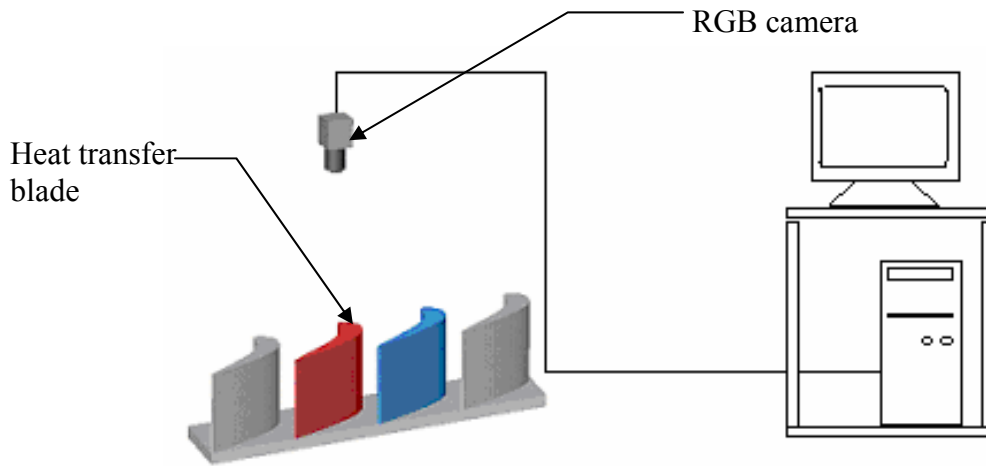


Figure 4.13: Schematic of the visual processing system for liquid crystal method

Figure 4.14 shows the schematic of the visual processing system used for IR method. The infrared thermography system used is a FLIR systems ThermaCAM SC 500. The camera offers a high quality, non-intrusive method for obtaining thermal data through a commercially available software package for data analysis. The camera has a range of -40°C to 500°C . The ThermaCAM 500 utilizes uncooled microbolometer longwave detectors to sense IR radiation. This makes them ideal for general thermal measurement applications. The SC 500 system features real time

14-bit digital output, a 320 x 240 pixel detector, precision temperature measurement, internal data storage, and outstanding thermal sensitivity. The camera has following specifications: the field of view and minimum focus distance are $24^{\circ} \times 18^{\circ}$ and 0.5m respectively, the spectral range is 7.5 to 13 μm and accuracy is +/- 2% or 2 $^{\circ}\text{C}$ [44].

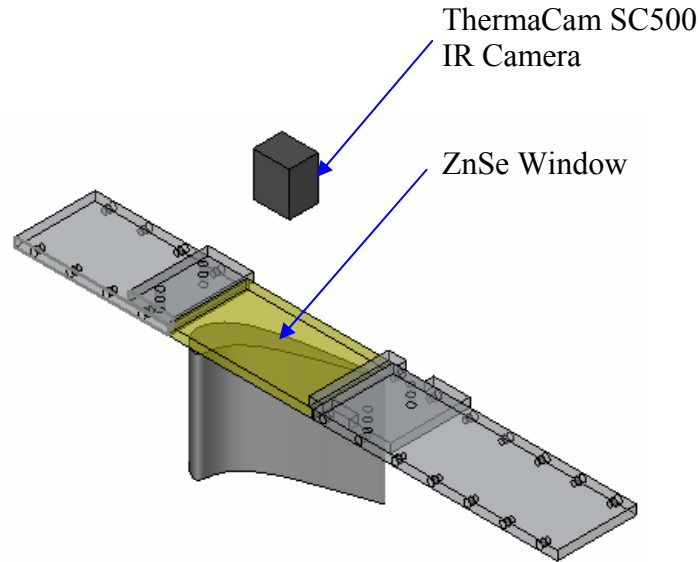


Figure 4.14: Schematic of the visual processing system for IR method

The IR window is made of Zinc-Selenide. It is chemically inert, non-hygroscopic, highly pure and theoretically dense material. It has extremely low bulk losses due to absorption and scatter, has a high resistance to thermal shock and is stable in virtually all environments [45]. Figure 4.15 shows the transmissive property of the window with wavelengths. More information is available at the CVD materials website (<http://www.cvdmaterials.com/znse.htm>). It is clear that the window has transmissivity of 0.72 for the wavelength the IR camera operates.

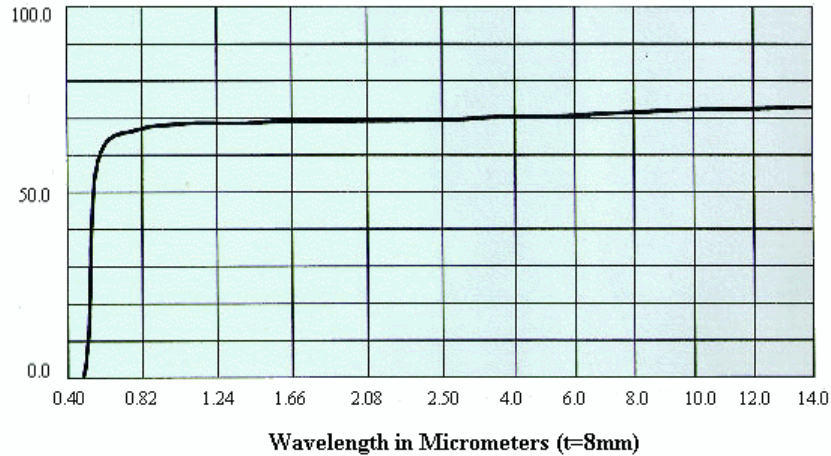


Figure 4.15: Transmissivity of Zinc-Selenide window with wavelengths [45]

4.3 Inlet Flow Characterization

In this section, information about the inlet flow conditions will be given. The test conditions at the inlet to cascade were measured using hot wire anemometry. The flow inlet velocity at cascade inlet was 65 m/s, which represents a cascade inlet Mach number of 0.16. The exit velocity to the cascade was 188 m/s, which is a Mach number of 0.54. The Reynolds number based on cascade exit velocity and blade axial chord is 861,000. Free stream turbulence intensity was also measured using hot wire. The average free-stream turbulence intensity at the cascade inlet was $Tu = 12.1\%$. As mentioned earlier, a blow down test facility is used; therefore the inlet total pressure does not remain constant. A test was performed to determine the total pressure variation during the blow down operation. Inlet total pressure was measured with a pitot probe (located 23 cm upstream of the test blades at midspan) and the NetScanner[®] pressure system. Figure 4.16 shows the inlet total pressure variation with time.

From the Figure 4.16, we see that the total pressure peaks immediately after the valve opens within 1.5 seconds and then drops steadily for the duration of the test. The variation during

the test of 30 seconds from highest to lowest absolute pressure is 3-5%. One point should be noted that the majority of the liquid crystal color change takes place after the first ten to twenty seconds of the heat transfer test. Also the duration of all pressure tests match those of the heat transfer tests.

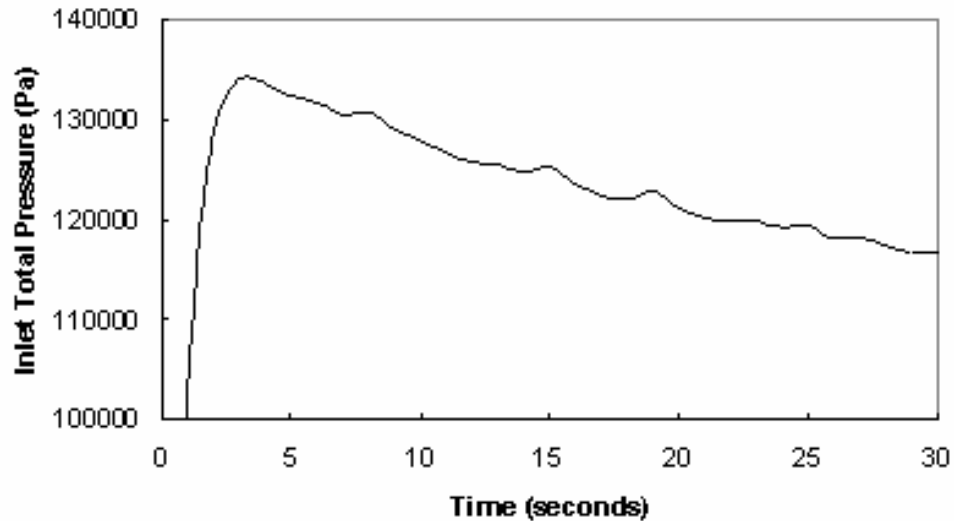


Figure 4.16: Inlet total pressure variation during blow down operation

Before running any experiments, tests were run to equalize pressure distribution through the three passages. Equalizing the passage pressures ensures that the flow field around the pressure and heat transfer blades is similar. Small holes are located on the shroud at identical locations above each passage. The tailboards were adjusted to achieve the equalization of pressure distribution in all three passages. Figure 4.17 represents the pressure (P_s/P_t) distributions in the three passages. Results show that the pressure distributions are relatively similar through each of the passages but the levels are slightly different. The middle passage lies between the heat transfer and the pressure blade.

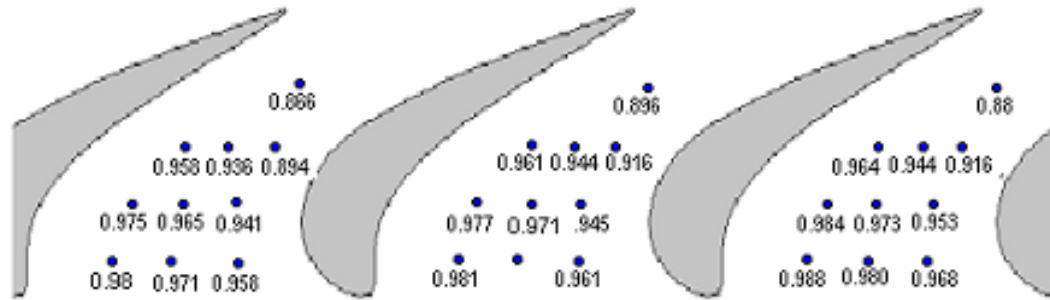


Figure 4.17: Pressure distribution on the shroud for all three passages

CHAPTER 5

5.1 Results (Uncooled Tip)

Figure 5.1 shows the plane tip and different squealer geometries that are investigated for this study. The first figure shows the simple plane tip geometry without any squealer. The second figure shows the full squealer and the rest of the figures show the four different partial squealer arrangements. For all the cases, tip gap is measured from the tip of the squealer to the shroud. The first partial squealer geometry is called pressure side (PS) squealer. The squealer rim exists along the entire pressure side edge of the blade only. The second partial squealer geometry is called suction side (SS) squealer. The squealer rim exists only along the entire suction side of the

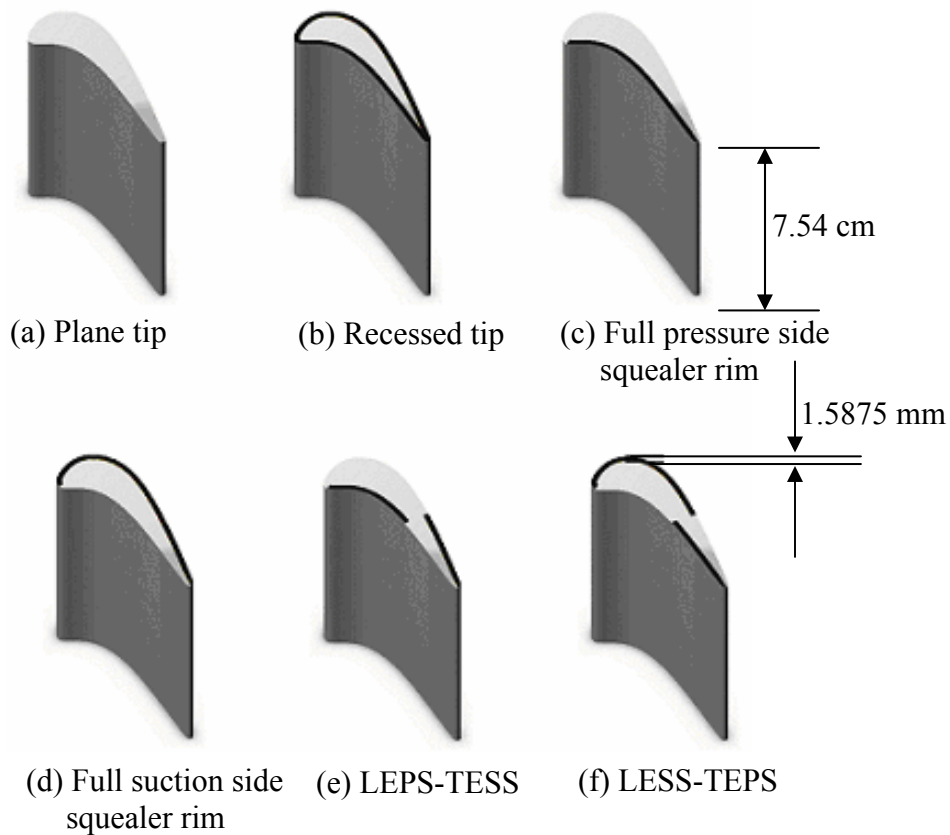


Figure 5.1: Different squealer geometries tested

blade. The third partial side squealer geometry has the pressure side leading edge and along the suction side trailing edge (LEPS-TESS). The fourth partial squealer geometry has the squealer rim on the leading edge suction side and along the pressure side trailing edge (LESS-TEPS).

5.2 Pressure Data

Figure 5.2 shows the effects of tip leakage flow on surface pressure distribution (Kontrovitz, 2000). The measurements for the blade pressure side, referred to as (P), and the suction side, referred to as (S). Pressure distributions are plotted for three different span locations. The locations from hub to tip are 33.3, 86.7, and 100% of the span.

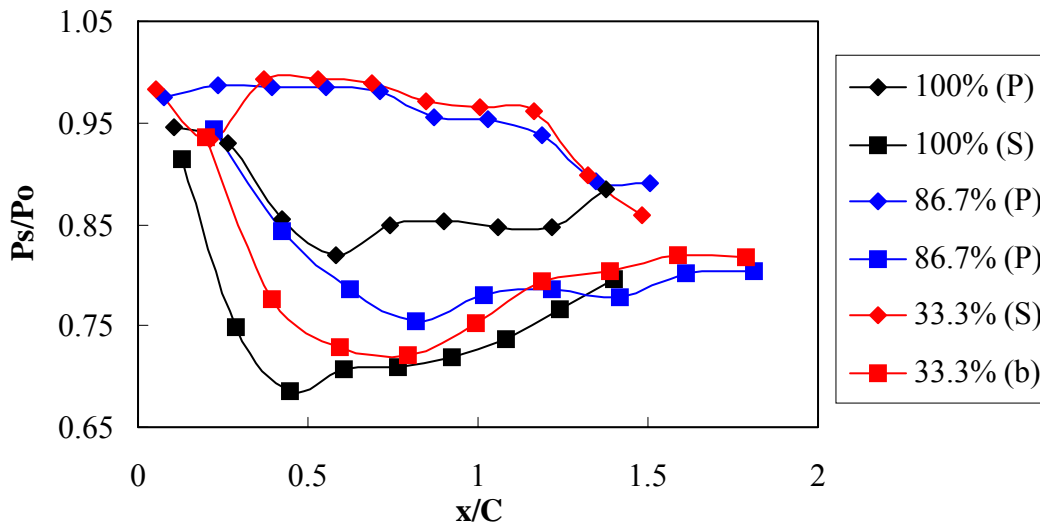


Figure 5.2: Surface pressure distribution at different span heights [46]

The data for 33.3% shows a large pressure gradient between the suction and pressure side. Leakage flow at the tip has not affected the pressure distribution around the blade surface. However, at 86.7% leakage flow has altered the pressure distribution slightly. The data for 86.7% shows a smaller gradient compared to the 33.3% data. This indicates secondary flow over

the blade surface in the direction of the blade tip. The 100% height, which is on the blade tip, has a much smaller pressure gradient than the 33.3% and 86.7% cases. The 100% height pressure gradient is greatly reduced because the clearance gap has induced secondary flow.

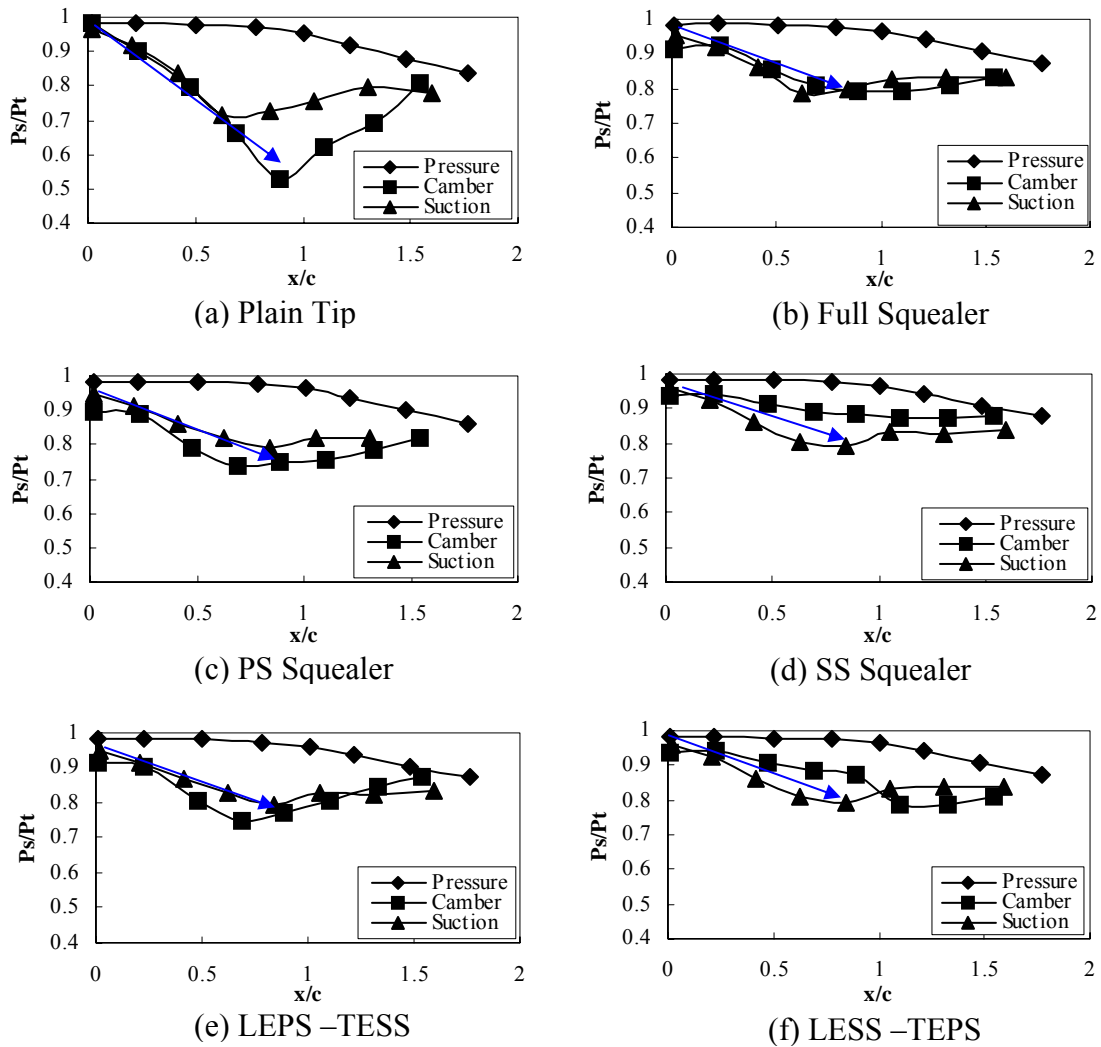


Figure 5.3: Shroud pressure distribution for plain tip and different squealer geometries

Figure 5.3 presents the pressure distributions on the shroud for the plane and all the squealer geometries. All the partial squealer geometries have squealer depth to span ratio of

0.0104 and tip gap of 1.0% of the blade span. Static pressures on the shroud (P_s) are normalized by the inlet total pressure (P_t) and the distance along the blade profile (x) is normalized by the axial chord (C) for all the graphs. Higher value of the pressure ratio (P_s/P_t) indicates lower velocity and the lower value of P_s/P_t represents the higher velocity of air.

The pressure gradient across the pressure side to the camber line indicates the strength of the leakage flow. It is clear that suction side reduces the pressure gradient more than any other geometry. The LESS-TEPS squealer also reduces leakage flow from leading edge to the mid-section but then the pressure gradient flips due to the squealer on the pressure side. It is obvious from the data that whenever a squealer is placed on the pressure side, it accelerates the flow. The effect of the acceleration will be seen on heat transfer data that will be presented later.

5.3 Heat Transfer Data

Detailed heat transfer distributions over the blade tip are presented for both plain tip and different squealer geometries in Figure 5.4. Blue, green areas represent lower heat transfer coefficient regions and red, pink areas represent higher heat transfer coefficient regions.

For the plain tip (Figure 5.4(a)), a region of low heat transfer coefficient is observed. This region is referred to as the “sweet spot”. Heat transfer coefficient values are significant along the trailing edge, close to pressure side. Flow separation occurs at the pressure side tip edges as the flow enters the clearance gap and then reattaches on the tip surface causing a low heat transfer region immediately behind the edge and a high heat transfer region in the reattachment region. The heat transfer coefficient values in the trailing edge region range from 800-1000 W/m^2K .

Full squealer (Figure 5.4 (b)) reverses the heat transfer distributions on the tip surface. The higher heat transfer region moves towards the leading edge due to flow separation and reattachment phenomena. A region of high heat transfer coefficient occurs from $X/C = 0-0.5$ due

to high pressure gradient across the area from pressure to camber line. This region, called the “hot spot”, has values ranging from 600-800 W/m²K. There also appears to be an overall reduction in heat transfer coefficient over the entire tip surface.

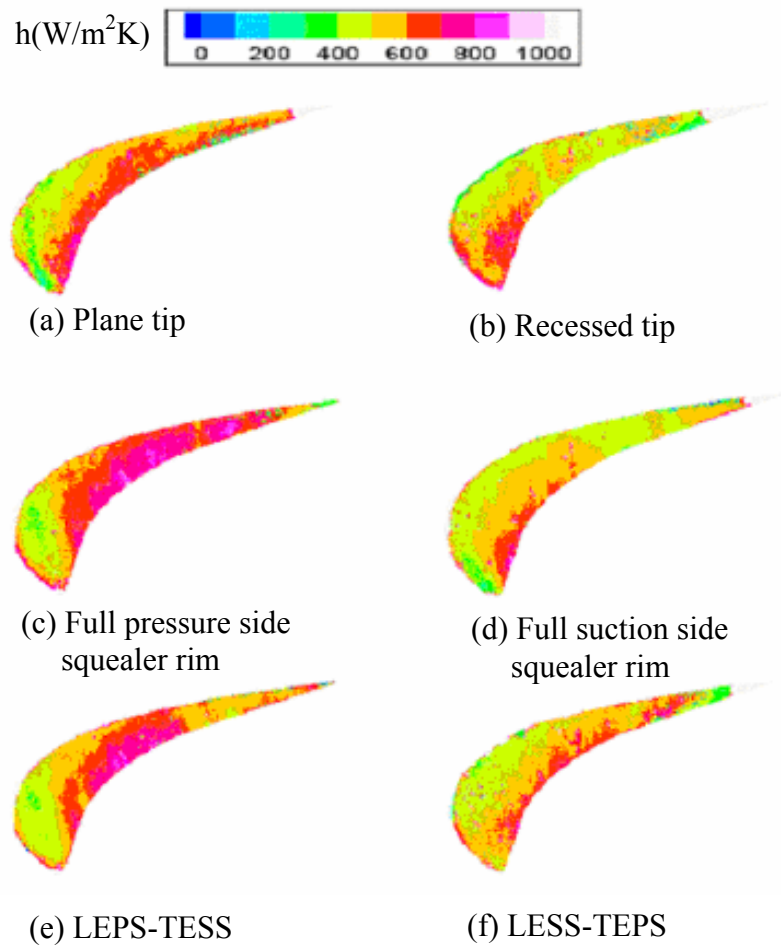


Figure 5.4: Detailed heat transfer coefficient distribution for plane and different squealer geometries

Figure 5.5 presents the overall interpretation of the flow over the plain and squealer tip based on the pressure and heat transfer results. Most of the flow over the plain tip hugs the pressure side along the leading edge and crosses over after $X/C > 0.5$. The leakage flow is limited in the leading edge region due to the lower pressure gradient across the tip. This cause the low

heat transfer region referred to as the “sweet spot”. Towards the trailing edge, the pressure gradient across the tip increases causing a strong leakage flow and subsequently higher heat transfer coefficients. For the squealer tips, the leakage flow occurs in the region immediately after the leading edge. Flow enters the cavity reattaches to the recessed flow and then accelerates through the clearance gap on the suction side rim. The flow closer to the trailing edge hugs the blade surface and does not flow over the tip due to reduced pressure gradient.

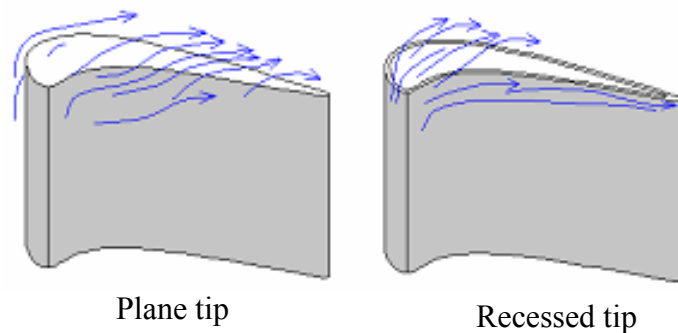


Figure 5.5: Illustration of tip leakage flows for plain tip and squealer based on pressure and heat transfer distributions

With the full PS squealer (Figure 5.4(c)), the heat transfer coefficients are enhanced compared to the plain tip. This may be due to the flow accelerating after entering the tip gap along the tip surface towards the TE due to the blockage at the entrance of the gap. There is stronger separation and reattachment over the entire tip surface. With the full SS squealer (Figure 5.4(d)), the tip leakage flow does not see the overall pressure gradient across the tip gap. The leakage flow is accelerated into the tip gap but decelerates as it encounters the suction side squealer wall. There is very little flow separation due to the lack of the pressure side squealer wall. There appear some remnants of a sweet spot as in the case of the plain tip and reduced heat transfer at the TE due to the suction side squealer wall.

With the LEPS-TESS partial squealer (Figure 5.4(e)), the sweet spot region is greatly enhanced but the flow separation along the pressure sidewall is clearly higher. This causes higher heat transfer coefficient along the mid section of the tip surface. This squealer, although produces higher heat transfer coefficients than the plain tip, does perform better than the full PS squealer. With the LESS-TEPS partial squealer (Figure 5.4 (f)), the heat transfer coefficient along the pressure side edge is higher than the suction side edge. The flow appears to have a weak flow separation and reattachment along the leading edge and the presence of the squealer on the pressure side along the trailing edge reduces leakage flow. Overall this squealer configuration produces lower heat transfer coefficients than the plain tip but is still lower than the values obtained for the full SS squealer. Both Bunker and Bailey [10] and Azad et al. [4] showed similar results for pressure side squealer versus suction side squealers.

Figure 5.6 shows the overall averaged heat transfer coefficients for the tip surface for different tip geometries. The heats transfer coefficients were averaged pixel to pixel to obtain the area-averaged heat transfer coefficients. The differences in heat transfer distributions on the surface are very different for each tip geometry, but the overall value can be used to obtain the total heat load to the tip surface. As seen from the plot, the plane tip value is around $600 \text{ W/m}^2\text{K}$. The full squealer provides the best reduction in heat transfer coefficients. The PS squealer increases the overall heat transfer coefficient. Among all the squealers, the SS squealer is the only one that reduces heat transfer coefficient compared to the plane tip. This indicates that the loss of squealer on the pressure side rim may be actually benefit the tip surface. Any suction side loss will cause an increase in heat load.

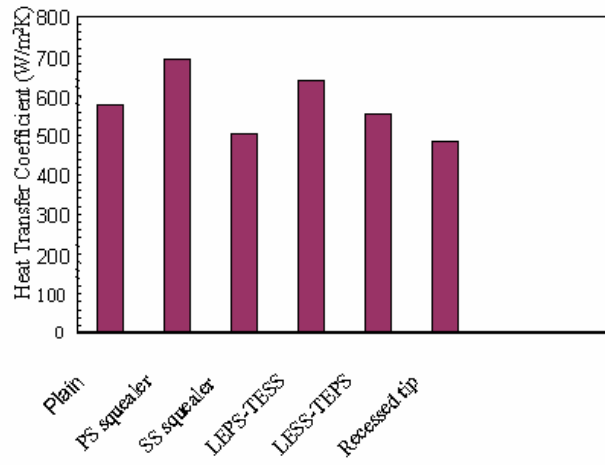


Figure 5.6: Area averaged heat transfer coefficient for plane and different squealer geometries

CHAPTER 6

6.1 Results (Tip Injection)

In this chapter, pressure data on the shroud and heat transfer data on the blade tip for both plane tip and recessed tip with peripheral squealer rim blade for blowing ratios $M=0, 1.0, 2.0$ and 3.0 will be given. The gap between the tip of the squealer rim to the shroud is maintained at 1%. Figure 6.1, shows the plane and recessed tip blade used for this study.

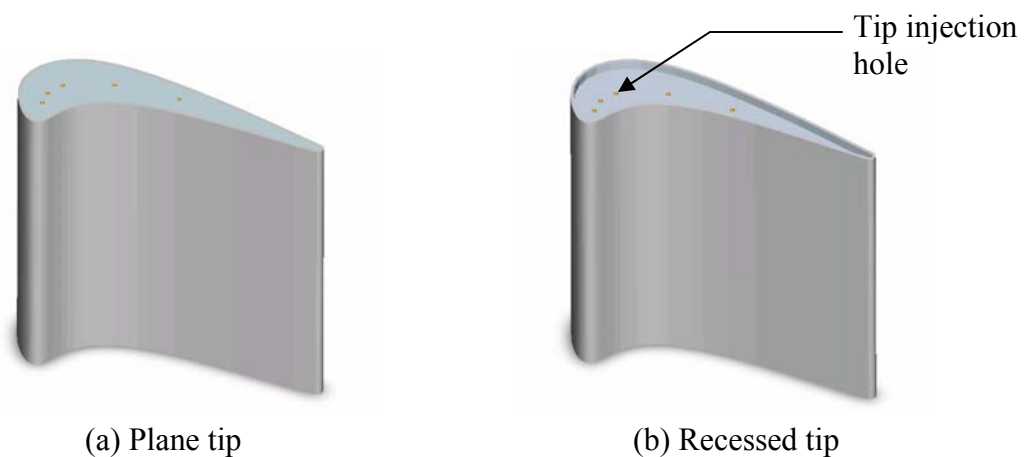


Figure 6.1: Plane and recessed tip blade with tip coolant injection holes

6.2 Pressure Data

Figure 6.2 shows the effect of blowing ratio on plane tip film injection. Static pressures on the shroud (P_s) are normalized by the inlet total pressure (P_t) and the distance along the blade profile (x) is normalized by the axial chord (C) for all the graphs. The diamond, square and triangle legends represent values for pressure taps located pressure side, camber line and suction side respectively. Different color is used for different blowing ratios. The lower value of pressure ratio indicates higher velocity and vice versa. As expected, we see acceleration of flow from pressure side to the camber line. The first noticeable effect of coolant injection is the shift of lowest value for camber line between no coolant injection ($M=0$) and all coolant injection

cases. Also, as the blowing ratio increases, the pressure ratio value increases for all pressure taps. This may be due to the blockage effect of coolant injection. Coolant may be restricting the leakage flow which should help reducing the heat load on the blade tip as will be seen in heat transfer data.

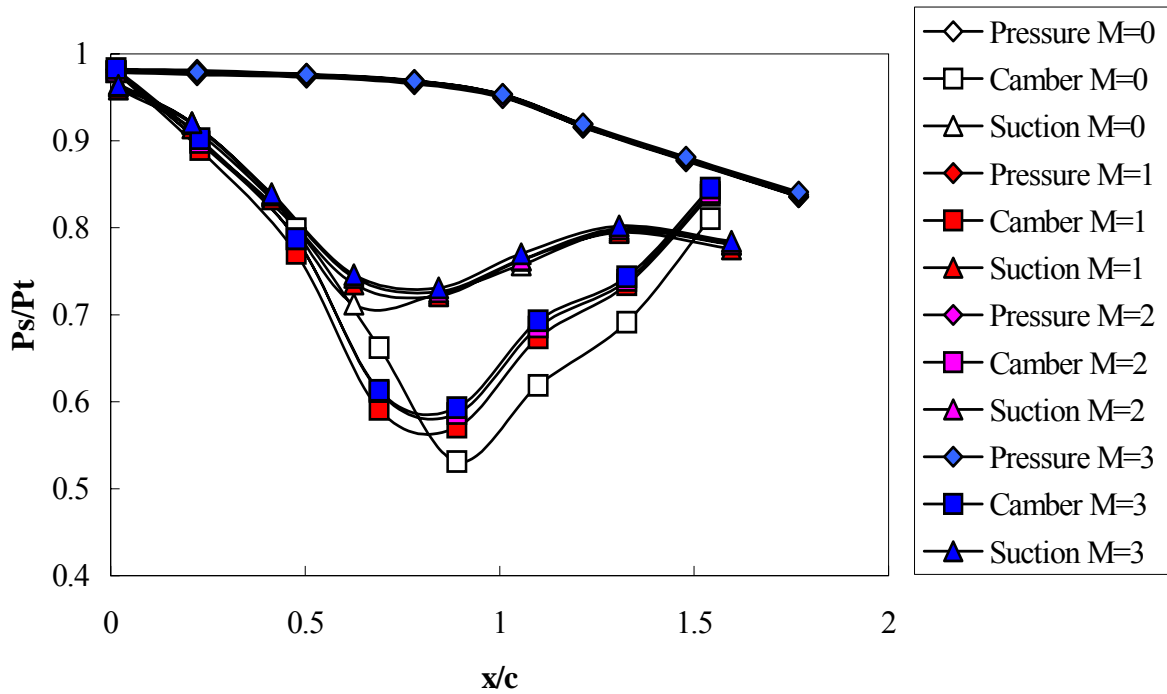


Figure 6.2: Effect of blowing ratio on plane tip for tip coolant injection

Table 6.1: Local blowing ratios for plane tip with tip only coolant injection

Recessed Tip with Tip Injection						
Hole	Global M	Local M	Global M	Local M	Global M	Local M
1	1.0	1.0953	2.0	2.0341	3.0	2.9969
2		1.0804		2.0758		3.0891
3		1.0529		2.0825		3.1305
4		0.9361		2.0100		3.1008
5		0.8567		1.7582		2.6970

Local blowing ratios for plane blade tip with tip only injection cases are shown in Table 6.1. The local blowing ratios are calculated using the equation and procedure described at the end of section 2.1 of chapter 2. Hole number starts with the first hole from the leading edge. As seen, local blowing ratios for first three holes are lower than global blowing ratios for all three global blowing ratios. Whereas last two holes show higher local blowing ratios than global blowing ratio and 4th hole has the highest local blowing ratio. As mainstream static pressure is higher near the leading edge, coolant mass flow rate coming out through the first three holes are lower. In contrary, mainstream static pressure along middle to near trailing edge is lower which results in higher coolant mass flow rate or higher blowing ratio.

Figure 6.3 shows the effects of coolant injection from the tip for recessed blade tip with peripheral squealer rim. One obvious difference between plane tip and recessed tip is the magnitude of pressure ratio for camber line values. For recessed tip, the ratio is much higher than plane tip. So, we can expect lower values of heat transfer coefficient for recessed tip. Also one interesting observation is that for plane tip, camber line values almost collapse with suction line values near leading edge ($x/c < 0.5$), whereas, for recessed tip, camber line values are lower than suction line values. This indicates that flow is accelerating near the leading edge for recessed tip and opposite is true for plane tip. So, higher heat transfer region for recessed tip near leading edge region and lower heat transfer region for plane tip can be expected. In heat transfer result; above-mentioned scenario will be observed.

For effects of blowing ratio, it is noticed that as the blowing ratio increases, a decrease in pressure ratio near leading edge is observed. Whereas, an increase in pressure ratio with an increase in blowing ratio is observed for middle to trailing edge region. So, a decrease and an increase in heat transfer coefficient for near leading edge and trailing edge respectively are

expected. But we will see from our heat transfer results that flow over recessed tip is too complex to explain from shroud pressure distribution. We will try to present a possible explanation in the heat transfer results section.

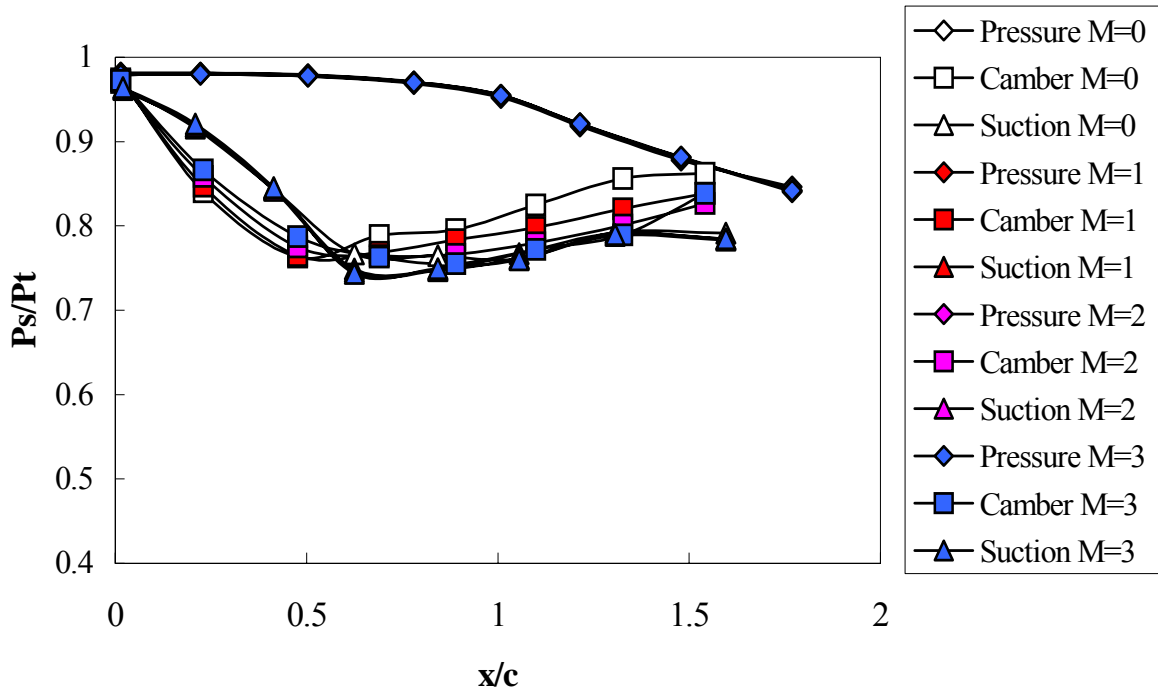


Figure 6.3: Effect of blowing ratio on recessed tip for tip coolant injection

Table 6.2: Local blowing ratios for recessed tip with tip only coolant injection

Plane Tip with Tip Injection						
Hole	Global M	Local M	Global M	Local M	Global M	Local M
1	1.0	0.2511	2.0	0.9758	3.0	1.8433
2		0.6237		1.3742		2.2846
3		0.9729		1.8706		2.8605
4		1.9737		3.4473		4.7490
5		1.2087		2.3112		3.2845

Local blowing ratios for recessed tip with tip only injection cases are shown in Table 6.2. It is observed that local blowing ratios are much more even between holes and the values are closer to global blowing ratios. This shows that even pressure distribution is present on recessed blade tip than plane blade tip. It also seems that flow is decelerating or pressure is high near the trailing edge, which results in lower blowing ratio for 5th hole.

6.3 Heat Transfer Data

Detailed heat transfer coefficient and film effectiveness distribution for plane tip is presented in Figure 6.4 for different blowing ratios. For no coolant injection case (case (a)), a low heat transfer coefficient region is observed near the leading edge. This is referred to as ‘sweet spot’. In this region, suction and camber line pressures collapse, meaning that there is little pressure difference to drive leakage flow. Very high heat transfer coefficient region is observed along the pressure side from middle of the blade towards trailing edge. This is due to the pressure side entry loss vortex. The heat transfer coefficient distribution observed is typical for plane blade tip and observed by many previous researchers.

The obvious effect of coolant injection is a reduction in heat transfer coefficient, especially along the pressure side region. Also, horseshoe vortex is clearly visible ahead of each hole. For blowing ratio, $M=1$, from the direction of horseshoe vortex, it is clearly seen that leakage flow is directing from pressure side leading edge towards suction side trailing edge. A region of very low heat transfer coefficient region is also observed just after the holes. Due to acceleration of flow in between holes, higher heat transfer coefficient regions are observed there. Due to blockage effect, heat transfer coefficient decreases as blowing ratio increases. It is also seen that the region of small heat transfer coefficient near the trailing region diminishes as blowing ratio increases.

No film effectiveness is observed for almost entire blade tip except small regions just after the holes. Because of the difference in local blowing ratio between holes, different jet widths are observed for different holes. An increase in film effectiveness is noticed as blowing ratio increase from 1 to 2. But a decrease in value is noticed for blowing ratio, $M=3$. As seen in table 1, the local blowing ratios for each hole are pretty high, which most likely results in ‘lift off’. During ‘lift off’, due to high momentum of the coolant jet, it shoots up and dissipates into the mainstream without adhering to the primary surface as seen for hole number 1 and 3. Sometimes, the jet may reattach itself to the surface, which results in high effectiveness as seen for hole number 2, 4 and 5.

Effects of blowing ratio on heat transfer coefficient and film effectiveness distribution for recessed tip is presented in Figure 6.5. Reverse trend is observed for recessed tip than plane tip. A high heat transfer coefficient region is noticed near the leading edge region and lower values are noticed for trailing edge region. This opposite trend is actually beneficial to the blade because the cross section is the widest near the leading edge due to which it can better withstand higher heat load than thin trailing edge.

It appears that as blowing ratio increases, heat transfer coefficient decreases, at least near the leading edge. Though the decrease is not as obvious as plane tip. Also, there is a low heat transfer region near pressure side of trailing edge region. Thickness of this region is smallest for highest blowing ratio. It seems like that for blowing ratio, $M=1$ and $M=2$, leakage flow enters the recessed tip near the leading edge and goes out of the tip near suction side of the trailing edge region. For blowing ratio, $M=3$, possibly the interaction between jet and leakage flow is minimum due to higher momentum of the jet. As a result, leakage flow expands more and reduces the low heat transfer region.

For film effectiveness distribution, highest film effectiveness is observed for blowing ratio, $M=2$. The directions of jets are along the camber line. The first four holes have similar local blowing ratios and they also exhibit similar film effectiveness. Interestingly, the fifth hole has lowest effectiveness for all three blowing ratios. It may be due to the fact that it has the lowest local blowing ratio as noticed in table 2. For blowing ratio, $M=3$, almost no effectiveness is observed for the whole tip. This is due to lift off or blowing off of the jet.

Detailed net heat flux ratio distribution is presented in Figure 6.6. This takes into account the combined effect of film effectiveness and heat transfer coefficient. For plane tip cases, a decrease in net heat flux ratio value for entire tip is observed as blowing ratio increases. Values of more than 1 are observed near the leading edge region. This is due to the fact that, no coolant injection case has very low heat transfer coefficient region, whereas coolant injection actually increases heat transfer coefficient in that region and film effectiveness values are not high enough to make up for the increase in heat transfer coefficient. Also, just after the holes, very low values are observed. This is because of high film effectiveness and low heat transfer coefficient values. Also, a thin region of higher net flux ratio region is observed along the suction side region.

For recessed tip blade, as blowing ratio increases from 1 to 2, we see a decrease in net heat flux ratio values. The high value region near leading edge for blowing ratio, $M=1$ is due to the high heat transfer region observed in Figure 6.5 (e). For blowing ratio, $M=3$, small areas of high net flux ratio are observed near the trailing edge. They are located along the jet direction. It seems that the jet increased the heat transfer coefficient in those areas without producing any film effectiveness.

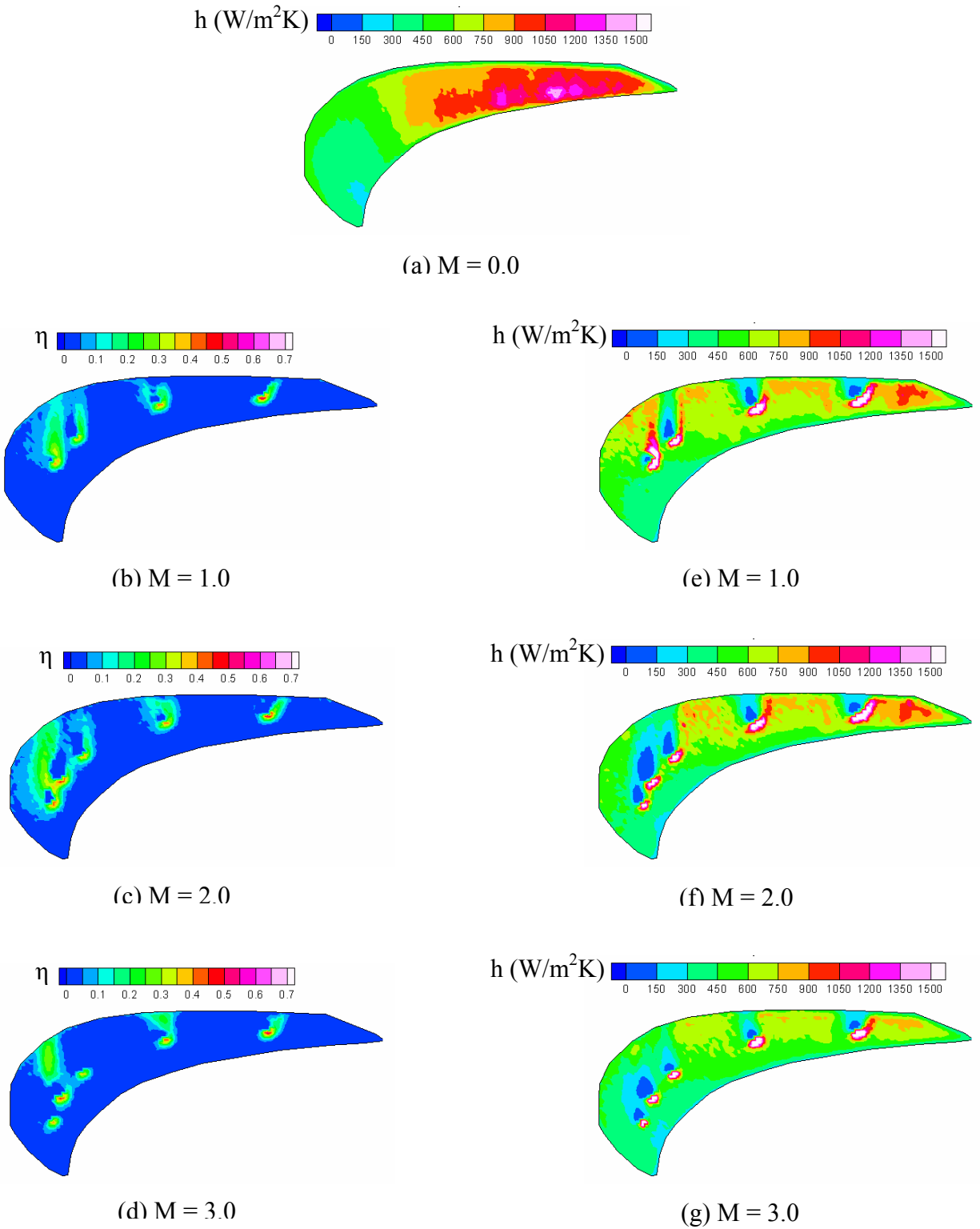


Figure 6.4: Effect of blowing ratio on plane tip heat transfer coefficient and film effectiveness distribution for tip coolant injection

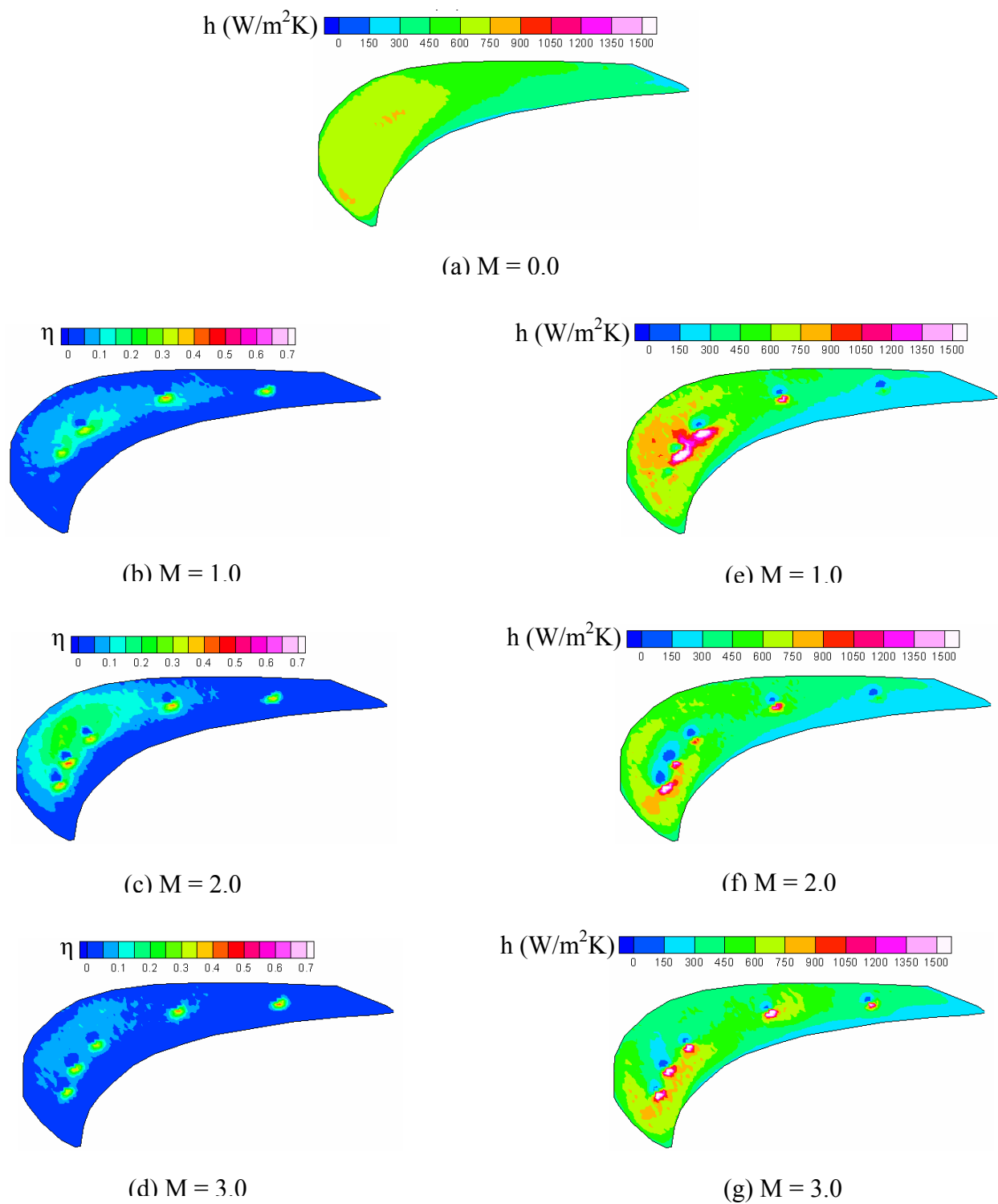
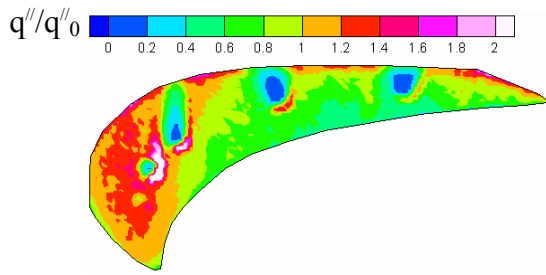
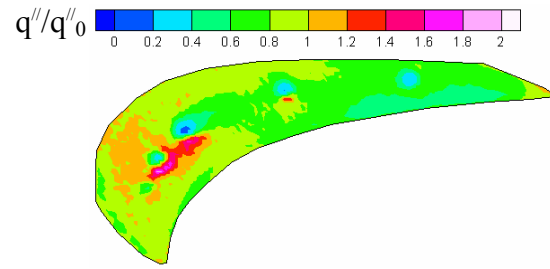


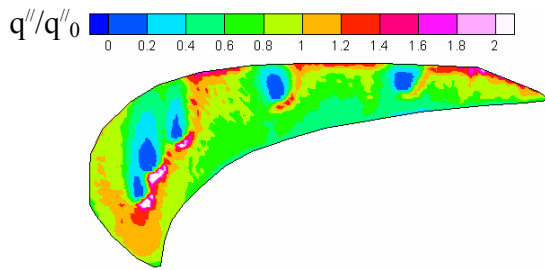
Figure 6.5: Effect of blowing ratio on recessed tip heat transfer coefficient and film effectiveness distribution for tip coolant injection



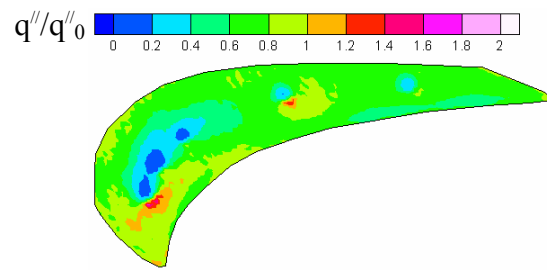
(a) Plane tip ($M = 1.0$)



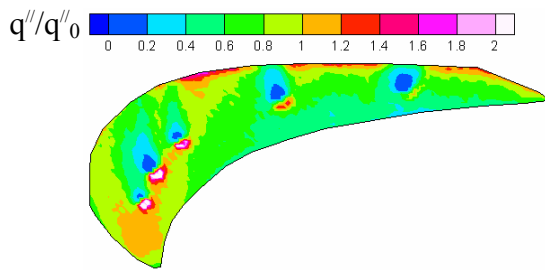
(d) Recessed tip ($M = 1.0$)



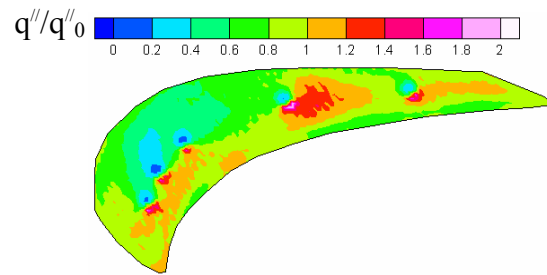
(b) Plane tip ($M = 2.0$)



(e) Recessed tip ($M = 2.0$)



(c) Plane tip ($M = 3.0$)



(f) Recessed tip ($M = 3.0$)

Figure 6.6: Effect of blowing ratio on recessed tip net heat flux ratio distribution for tip coolant injection

CHAPTER 7

7.1 Results (Pressure Side Hole Injection)

In this chapter, pressure data on the shroud and heat transfer data on plane tip and recessed tip for coolant injection from the pressure side holes are presented. Experiments were run for blowing ratios of $M=0$, 1.0, 2.0 and 3.0. Figure 7.1, shows the plane and recessed tip blade used for this study.

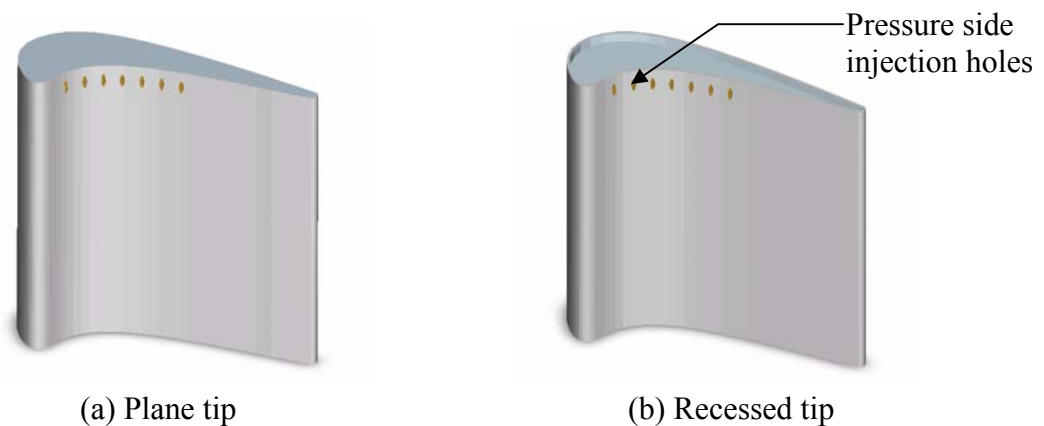


Figure 7.1: Plane and recessed tip blade with pressure side coolant injection holes

7.2 Pressure Data

Figure 7.2 shows the effect of blowing ratio on plane tip for pressure side coolant injection. Coolant injection causes a decrease in pressure ratio or acceleration of flow for camber line near leading edge and middle portion of the blade. Whereas, deceleration near the trailing edge is observed. Interestingly, increase in static pressure for suction line ($0.5 < x/c < 1.0$) between no injection and with injection cases is also noticed.

Local blowing ratios for plane tip with pressure side only coolant injection are presented in Table 7.1. As mentioned in chapter 2, surface pressure on the 86.7% span of the pressure side

of the blade is used as reference data. So, the values presented here are just estimated values. The first observation is that local blowing ratio for all holes are almost equal. This is due to the fact that static pressure on the pressure surface of the blade remains almost constant and does not decrease sharply as compared to suction surface. Also, local blowing ratio values are closer to global blowing ratios.

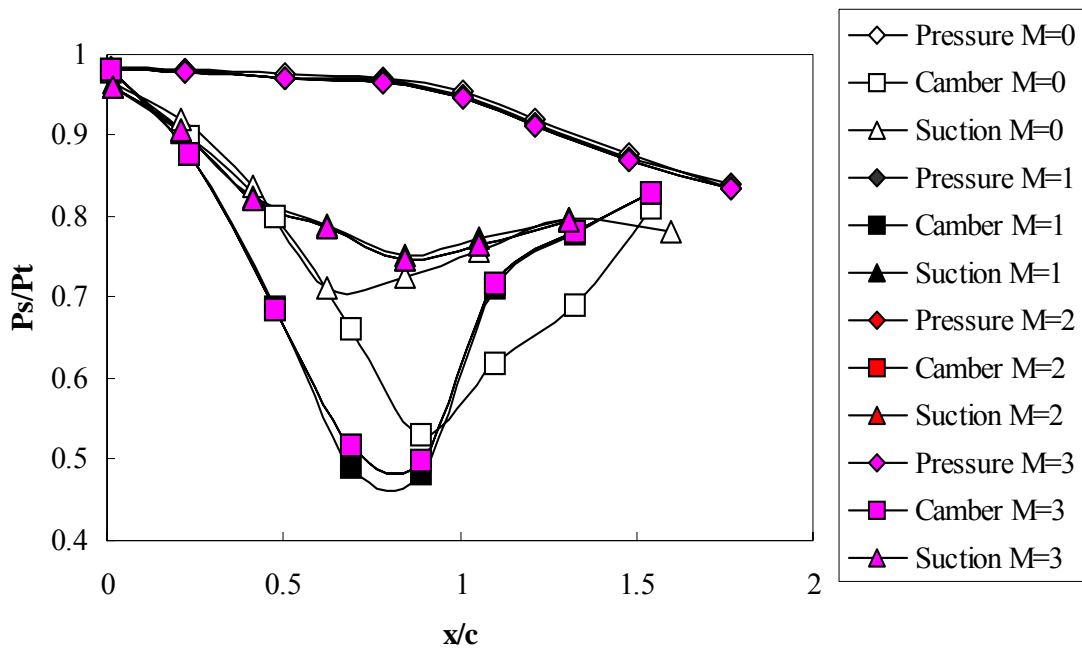


Figure 7.2: Effects of blowing ratio on plane tip for pressure side coolant injection

Figure 7.3 shows the effects of blowing ratio on recessed blade tip for pressure side coolant injection. No injection case ($M=0$) is not visible because it is at the same level as blowing ratio, $M=1$ case. This shows that coolant injection at low blowing ratio does not have any effect on pressure distribution. But for higher blowing ratios, coolant injection increases the pressure ratio for camber line near the leading edge and it creates an opposite effect near the trailing edge. But the effect or the difference in pressure ratio values is more prominent between blowing ratio, $M=1$ and $M=2$ than blowing ratio $M=2$ and $M=3$.

Table 7.1: Local blowing ratios for plane tip with pressure side only coolant injection

Plane Tip with Pressure Side Injection						
Hole	Global M	Local M	Global M	Local M	Global M	Local M
1	1.0	1.0462	2.0	2.0573	3.0	3.0517
2		0.9691		1.9513		2.9544
3		0.9803		1.9666		2.9684
4		0.9900		1.9799		2.9805
5		0.9870		1.9758		2.9767
6		1.0013		1.9953		2.9945
7		1.0314		2.0368		3.0328

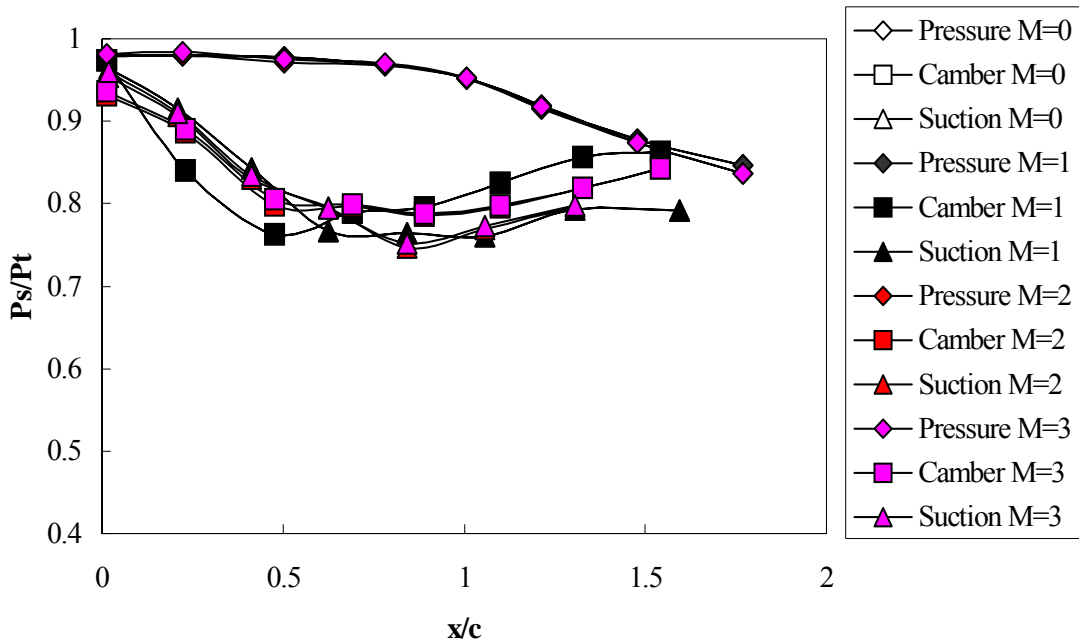


Figure 7.3: Effects of blowing ratio on recessed tip for pressure side coolant injection

Table 7.2 shows local blowing ratios for recessed tip with pressure side injection only case. Not much of a difference is observed between plane and recessed blade tip cases. Though same local blowing ratios are observed between plane and recessed blade tip, it will be observed

later that heat transfer coefficient and film effectiveness distributions between the two blade tips are entirely different. This is due to the two completely different flow patterns present between the two blade tips.

Table 7.2: Local blowing ratios for recessed tip with pressure side only coolant injection

Recessed Tip with Pressure Side Injection						
Hole	Global M	Local M	Global M	Local M	Global M	Local M
1	1.0	1.0307	2.0	2.0527	3.0	3.0484
2		0.9666		1.9662		2.9688
3		0.9759		1.9786		2.9802
4		0.9839		1.9894		2.9900
5		0.9814		1.9860		2.9870
6		0.9933		2.0019		3.0016
7		1.0184		2.0359		3.0329

7.3 Heat Transfer Data

Detailed heat transfer coefficient and film effectiveness distribution for plane tip is presented in Figure 7.4 for different blowing ratios. One obvious effect of pressure side coolant injection is the reduction in heat transfer coefficient along the pressure side that is observed for no injection or $M=0$ case. It appears that separation entry vortices are no longer present for all the coolant injection cases. It has also been noticed that high heat transfer coefficient regions are present along the suction side for blowing ratio, $M=1$ case. These regions diminish as blowing ratio increases to 2. The high heat transfer coefficient regions for blowing ratio, $M=3$ are due to reattachment of coolant jets. Also, streaks of jets marked by low heat transfer regions are visible along the pressure side of the blade tip.

Low effectiveness values are observed for all blowing ratios. Coolant jet streaks are visible for blowing ratio, $M=1$ along the pressure side. But for blowing ratio, $M=2$, those jet streaks are not present. It appears that all the jets lift off and they do not reattach themselves on

the tip. For blowing ratio, $M=3$, we see the reattachment of the jets along the suction side after the jets hit the shroud.

Figure 7.5 shows the detailed heat transfer coefficient and film effectiveness distribution for recessed tip blade. No injection case and blowing ratio, $M=1$ cases are almost identical except the low heat transfer coefficient region located near the pressure side trailing edge for $M=1$ case. This low heat transfer region is present for all blowing ratio cases. As blowing ratio increases, the high heat transfer coefficient region near the leading edge continues to decrease in size. No film effectiveness is observed for all blowing ratio except a faint trace for blowing ratio, $M=3$. Overall, it appears that pressure side coolant injection is totally ineffective for recessed tip case. This may be due to high pressure present inside the squealer cavity. As seen in Figure 7.3, pressure ratios along camber line for recessed tip are much higher than plane tip. This high pressure possibly preventing coolant jets to get into the cavity, which results in no effectiveness for recessed blade tip.

Detailed net heat flux ratio distributions are presented for both plane and recessed tip case in Figure 7.6. For plane tip cases, a high value region is observed near leading edge. The value decreases as blowing ratio increases. It appears that pressure side coolant injection redirected the leakage flow for plane tip. Low value regions can be seen along the pressure side. This is direct effect of the coolant jets. For recessed tip blade, the value of net heat flux ratio is close to 1 for almost all the tip region. This indicates that pressure side coolant injection for recessed tip blade is not beneficial at least for the tip. It may however help in cooling the thin squealer rim.

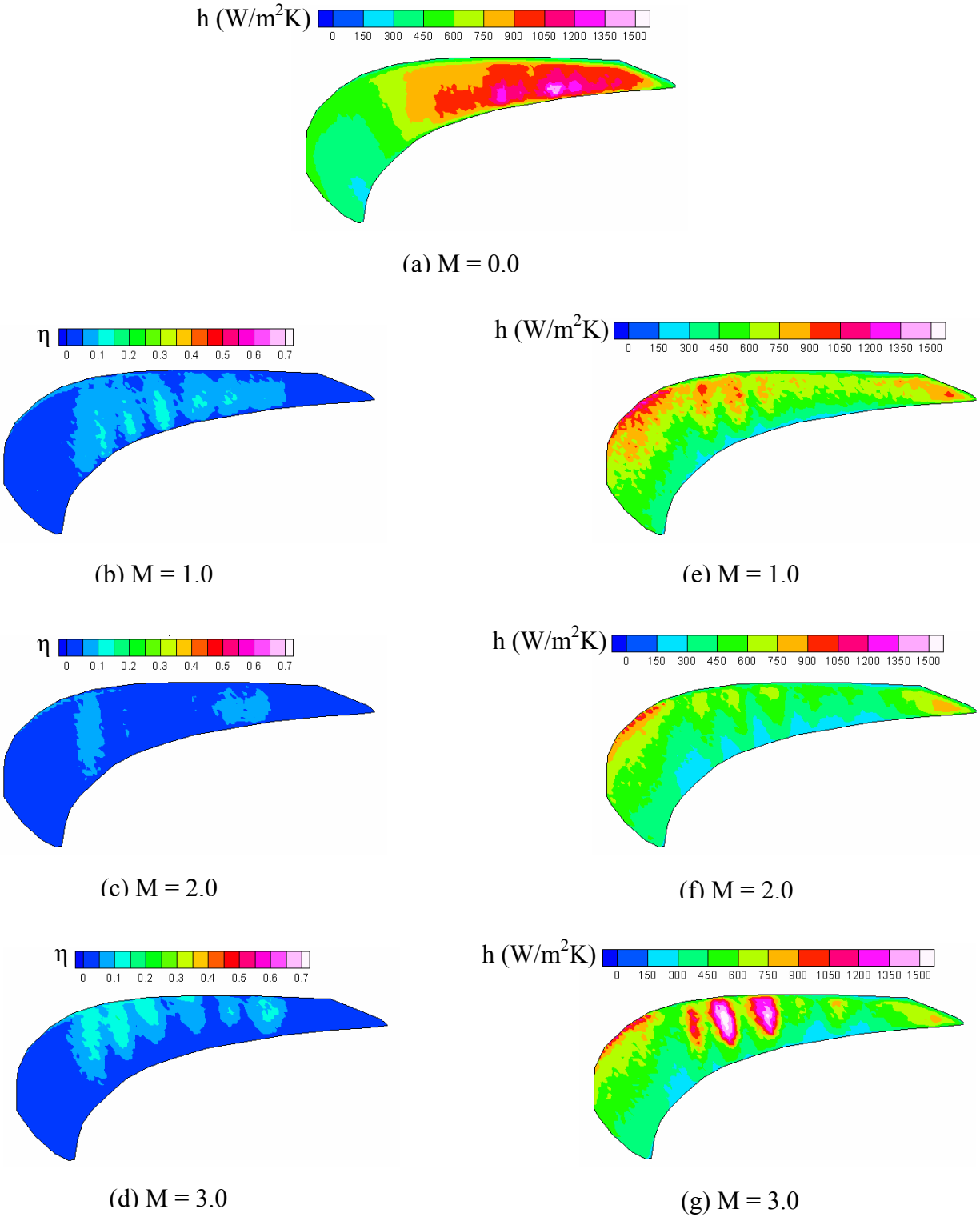


Figure 7.4: Effect of blowing ratio on plane tip heat transfer coefficient and film effectiveness distribution for pressure side coolant injection

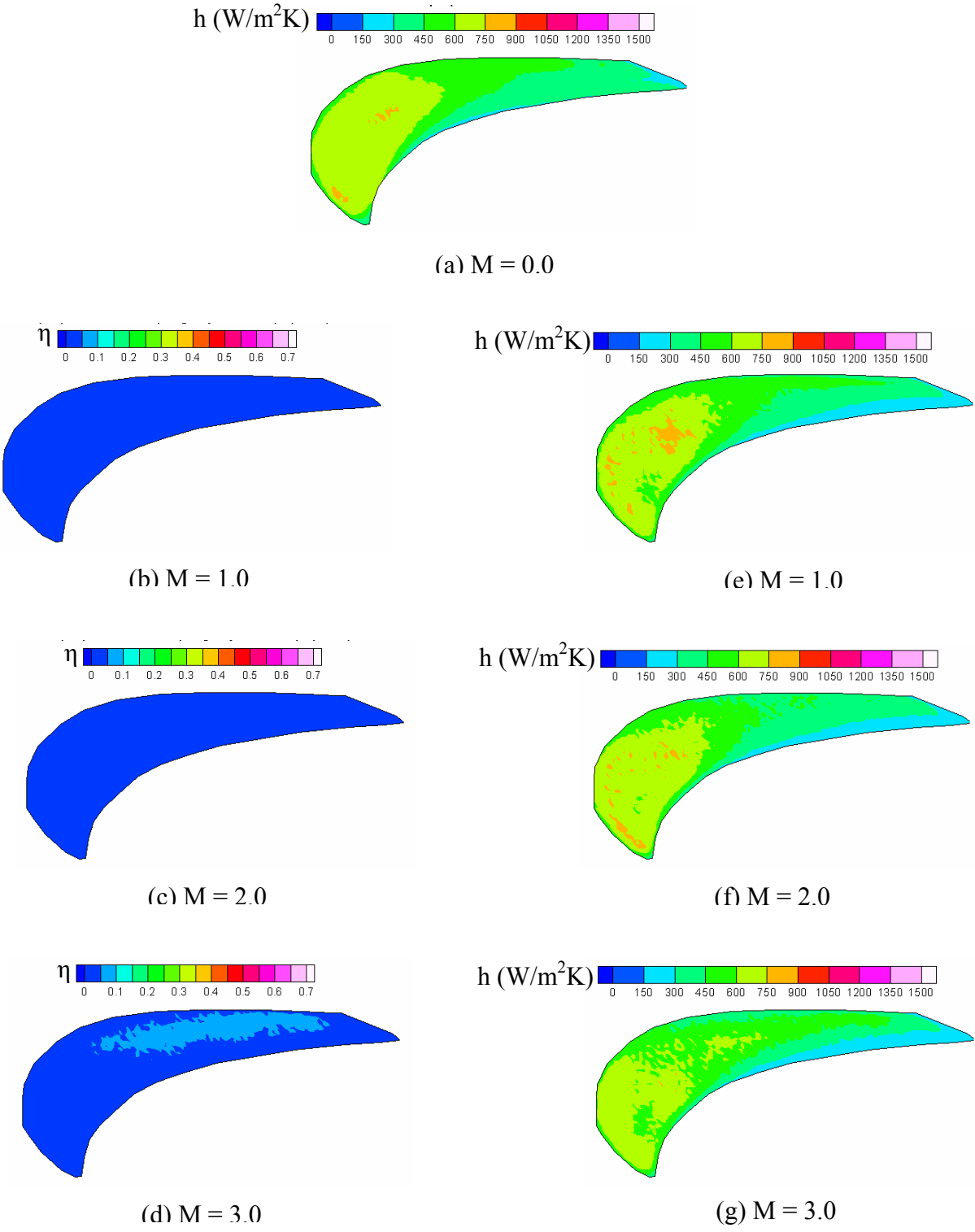
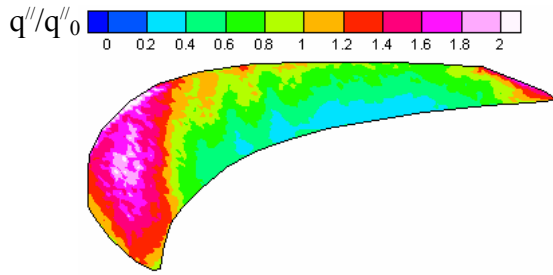
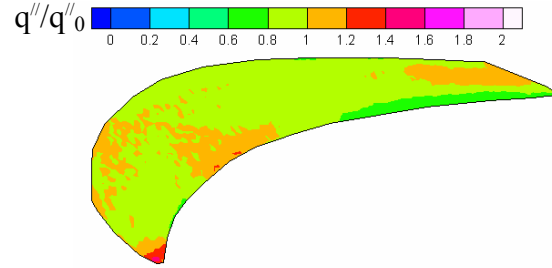


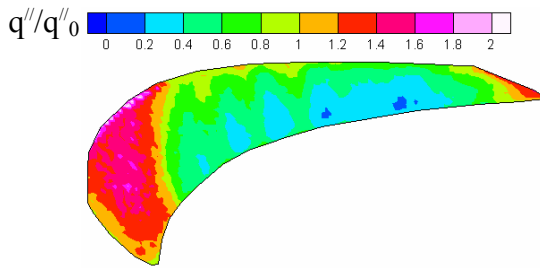
Figure 7.5: Effect of blowing ratio on recessed tip heat transfer coefficient and film effectiveness distribution for pressure side coolant injection



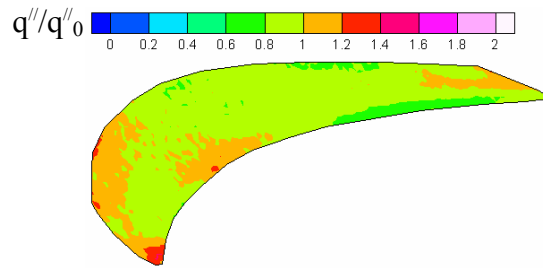
(a) Plane tip ($M = 1.0$)



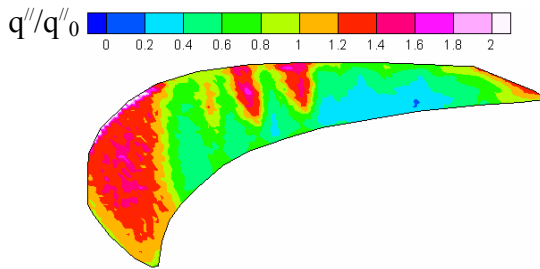
(d) Recessed tip ($M = 1.0$)



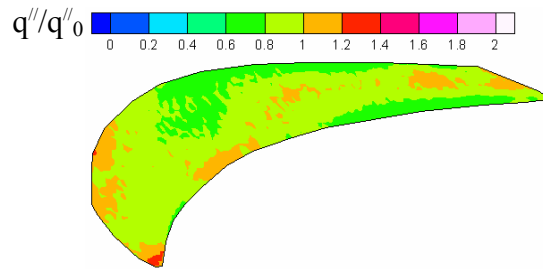
(b) Plane tip ($M = 2.0$)



(e) Recessed tip ($M = 2.0$)



(c) Planet tip ($M = 3.0$)



(f) Recessed tip ($M = 3.0$)

Figure 7.6: Effect of blowing ratio on plane and recessed tip net heat flux ratio distribution for pressure side coolant injection

CHAPTER 8

8.1 Results (Tip and Pressure Side Injection)

Results for combination cooling or when coolant is injected from both tip and pressure side holes will be presented in this chapter. Figure 8.1 shows the plane and recessed tip blade used for the experiment. The tip and pressure side hole configurations have already been discussed in chapter 3.

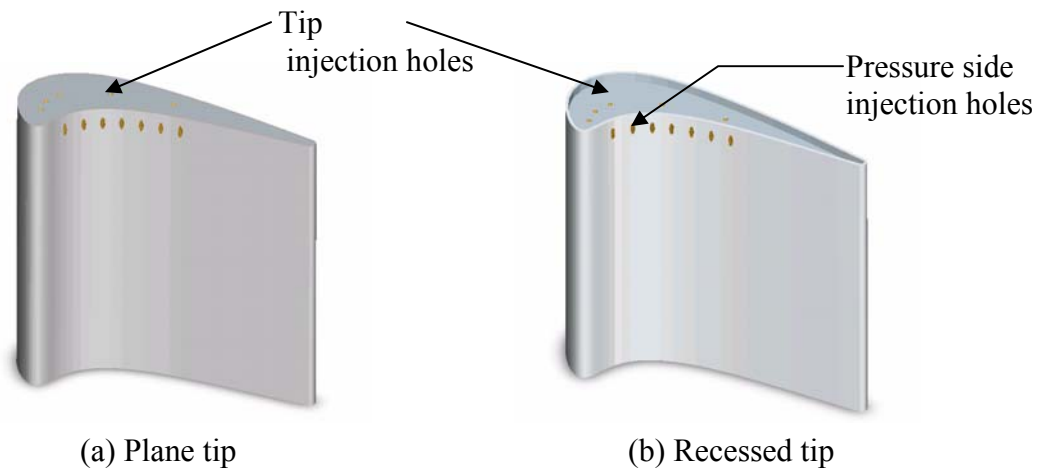


Figure 8.1: Plane and recessed tip blade with tip and pressure side coolant injection holes

8.2 Pressure Data

Plane tip pressure data is presented in Figure 8.2. A substantial difference for camber line data between no injection and with injection cases has been observed. It is clearly seen that coolant injection is causing deceleration of flow in camber line region and as the blowing ratio increases, the pressure ratio for camber line increases. The increase is much more obvious than tip only or pressure side hole only injection. This may be due to huge blockage effects caused by the two streams of jets from tip and pressure side. We also notice a peak just after $x/c = 1$ along the camber line. It may be due to the tip hole or the pressure side hole located at that region or

due to both of the jets being stronger than the other jets. A reduction in pressure ratio for suction line values is also observed.

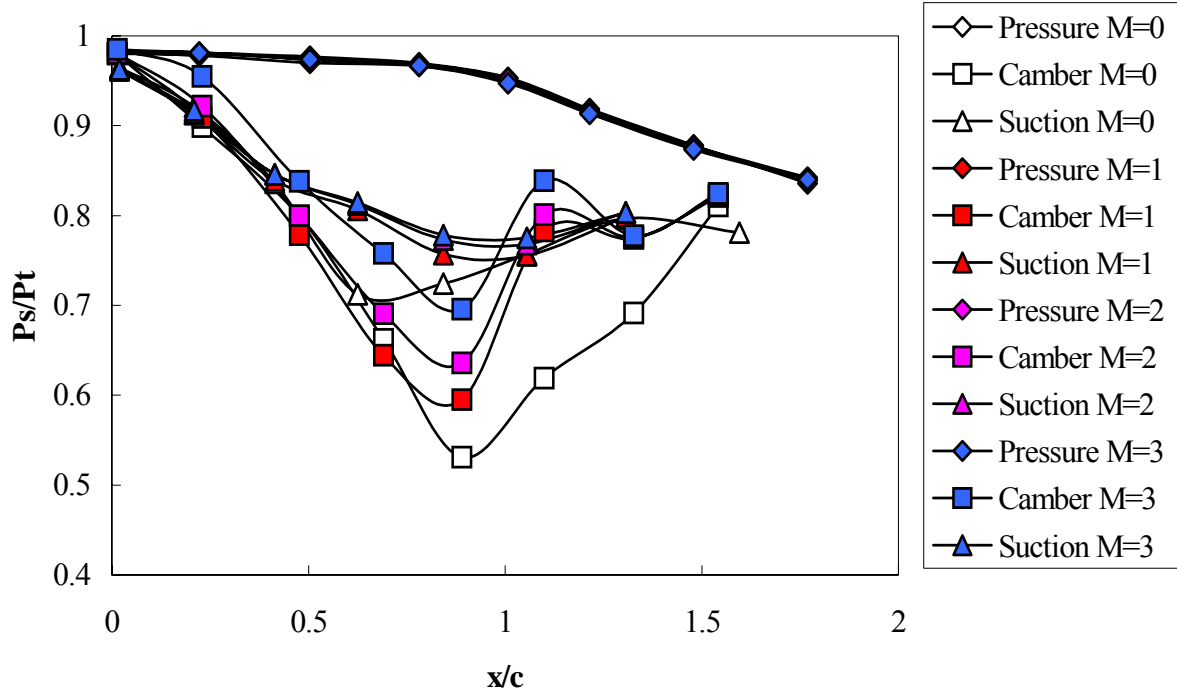


Figure 8.2: Effect of blowing ratio on plane tip for tip and pressure side coolant injection

Local blowing ratios for plane tip with combination injection cases are shown in Table 8.1. It is observed that local blowing ratios for tip coolant holes are higher than pressure side holes. In fact, local blowing ratios for tip coolant holes are higher than global blowing ratios. This is due to the fact that pressure side surface has higher pressure than blade tip especially the camber line where the tip coolant holes are located. This high pressure is causing less coolant to come out through the pressure side holes in comparison to the tip holes. Again, the 4th tip hole has the highest value. If local blowing ratios for tip holes in Table 6.1 (tip only injection) are compared to local blowing ratios for tip holes in Table 8.1 (combination injection), a significant increase in local blowing ratios for combination cases are observed for all the holes, especially

for the first hole. As will be seen later, this increase in blowing ratio for tip holes causes substantial impact between coolant and mainstream interaction, particularly for blowing ratio, $M=3.0$.

Table 8.1: Local blowing ratios for plane tip with combination coolant injection

Plane Tip with Combination Injection							
	Hole	Global M	Local M	Global M	Local M	Global M	Local M
Tip Holes	1	1.0	1.1003	2.0	2.8557	3.0	2.9457
	2		1.3949		3.2801		3.3229
	3		1.6726		3.5392		3.6003
	4		2.5463		3.1916		4.4880
	5		1.4541		2.3274		3.5239
Pressure Side Holes	1	1.0	0.5800	2.0	1.2983	3.0	2.6385
	2		0.5232		1.2349		2.5805
	3		0.5316		1.2441		2.5888
	4		0.5388		1.2520		2.5960
	5		0.5366		1.2495		2.5937
	6		0.5471		1.2612		2.6044
	7		0.5693		1.2861		2.6272

Figure 8.3 shows the effects of coolant injection for the recessed blade tip. For camber line values, there is an increase in pressure ratio as blowing ratio increases. The difference in no injection values and with injection values for suction line diminishes from leading edge to trailing edge. A decrease in heat transfer coefficient value along camber line near leading edge is expected. Also, it has been observed that camber line values are higher than suction line values near trailing edge that is the trademark trend of recessed tip flow. In general, the effect of blowing ratio for recessed tip is not as prominent as plane tip and camber line values for recessed tip are much lower than plane tip.

Local blowing ratios for recessed tip with combination coolant injection are shown in Table 8.2. Again, tip holes have higher local blowing ratios than pressure side holes. But the tip

holes for recessed tip have lower local blowing ratios than plane tip and the opposite is true for pressure side holes. This is due to higher static pressure on the recessed blade tip than plane tip. Also, the tip holes have almost equal local blowing ratios and the values are higher than global blowing ratios.

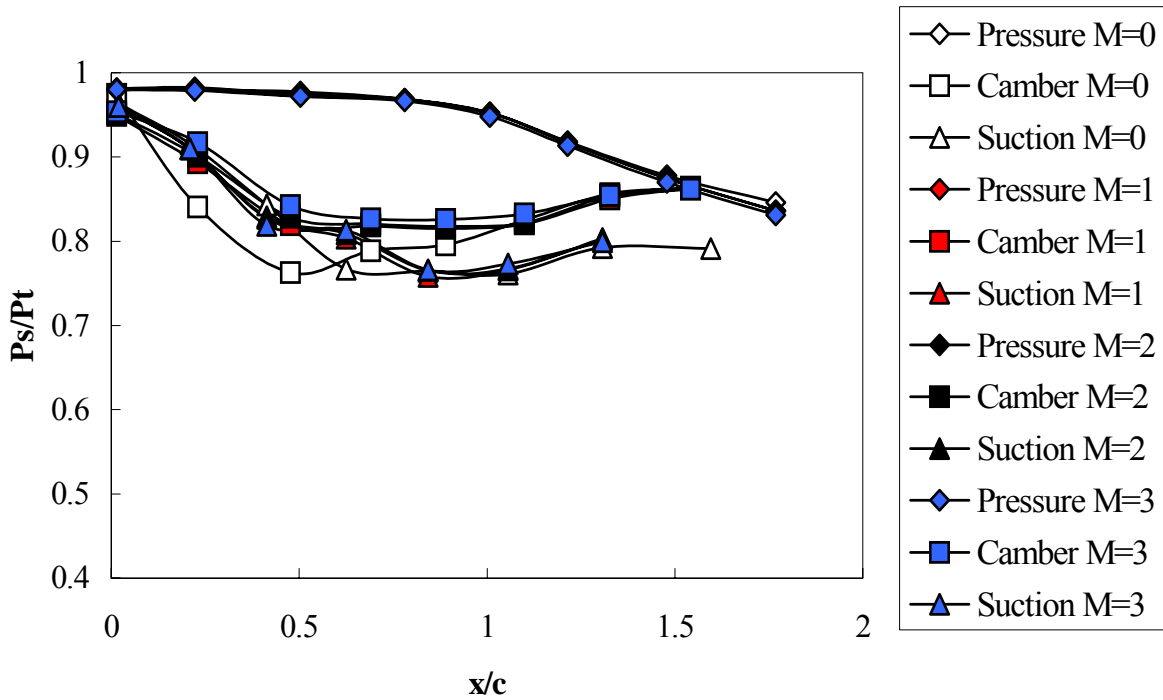


Figure 8.3: Effect of blowing ratio on recessed tip for tip and pressure side coolant injection

Table 8.2: Local blowing ratios for recessed tip with combination coolant injection

Recessed Tip with Combination Injection							
	Hole	Global M	Local M	Global M	Local M	Global M	Local M
Tip Holes	1	1.0	1.4369	2.0	2.5513	3.0	3.1272
	2		1.4413		2.5790		3.3547
	3		1.4468		2.5926		3.4449
	4		1.4446		2.5963		3.5424
	5		1.4760		2.6491		3.4557
Pressure Side Holes	1	1.0	0.7013	2.0	1.6129	3.0	2.7585
	2		0.6427		1.5468		2.7053
	3		0.6513		1.5563		2.7129
	4		0.6587		1.5645		2.7195
	5		0.6564		1.5620		2.7174
	6		0.6673		1.5741		2.7271
	7		0.6902		1.6001		2.7481

8.3 Heat Transfer Data

Figure 8.4 presents detailed heat transfer coefficient and film effectiveness distribution for plane tip for different blowing ratios. Coolant injection decreases the heat transfer coefficient compared to the no injection case. For blowing ratio, $M=2$, streaks of jets from pressure side holes are visible along pressure side of the blade. These streaks are not visible for blowing ratio 1 case. For blowing ratio, $M=3$, very high heat transfer coefficient regions are observed around hole 2, 4 and 5. These butterfly shape regions are extended from middle of the blade towards the suction side. It appears that for this high blowing ratio, coolant jet from the tip hits the shroud first and then bounces back on to the blade tip. This was not observed for tip only and pressure side injection only cases because in combination cases, the pressure side injection jets are creating a barrier for the tip injection jets. In addition, the tip holes have higher blowing ratios and this higher momentum of the jets causing minimum interaction between leakage flow and tip injection jet. As a result, the tip jets shoot up and then reattaches back on to the tip. Also, some reattachments of pressure side injection jets are observed for this case.

For blowing ratio, $M=1$ and $M=2$, coolant jets are much wider than tip only and pressure side injection only cases. This is obviously due to the combined injection and higher blowing ratios. Also, small effectiveness values are observed in between holes because of the injection from pressure side holes. For blowing ratio, $M=3$, high film effectiveness value of around 0.5 is observed for holes 2,4, and 5. Remember that the same holes have high heat transfer coefficient values. Also, high effectiveness values are observed in between holes. This is due to the reattachments of jets coming out of the pressure side holes.

Figure 8.5 shows effect of blowing ratio on recessed tip heat transfer coefficient and film effectiveness distribution for combined cooling. It has been observed that the high heat transfer coefficient region that is present in no injection case is absent for blowing ratio, $M=1$ case. For tip only and pressure side injection only cases, this high heat transfer coefficient region was present for blowing ratio, $M=1$ case. Typical low heat transfer coefficient region located along pressure side trailing edge region is also present for all blowing ratio cases. This region increases in size as blowing ratio increases. Like plane tip, very high heat transfer coefficient regions around holes 2,3, and 4 are present for blowing ratio, $M=3$. This may be due to the same reason as explained in plane tip case.

Blowing ratio, $M=1$ and $M=2$ shows almost same level of effectiveness. The high effectiveness regions are around holes 2, and 3. Though all the tip holes have similar local blowing ratios, hole 1, 3 and 5 are not showing less effectiveness. This is possibly due to the fact that effectiveness not only depend on local blowing ratios but also it depends on how the jet is interacting with leakage flow locally. It appears that leakage flow is streaming along the camber line from the leading edge towards the trailing edge. As expected, high film effectiveness values

are observed for blowing ratio, $M=3$ case. But the level of effectiveness is lower than the plane tip case.

Figure 8.6 shows detailed net heat flux ratio distribution for both plane and recessed tip. For plane tip, the values are lower than 1 for most of the blade tip. Blowing ratio, $M=2$ shows low net heat flux ratio regions along pressure side of the blade tip. A small high value region near leading edge is observed for blowing ratio, $M=3$. Recessed tip shows even distribution of net heat flux ratio except few small areas for blowing ratio, $M=1$ and $M=2$. For blowing ratio 3, high value region is present near leading edge, which extends to middle of the blade.

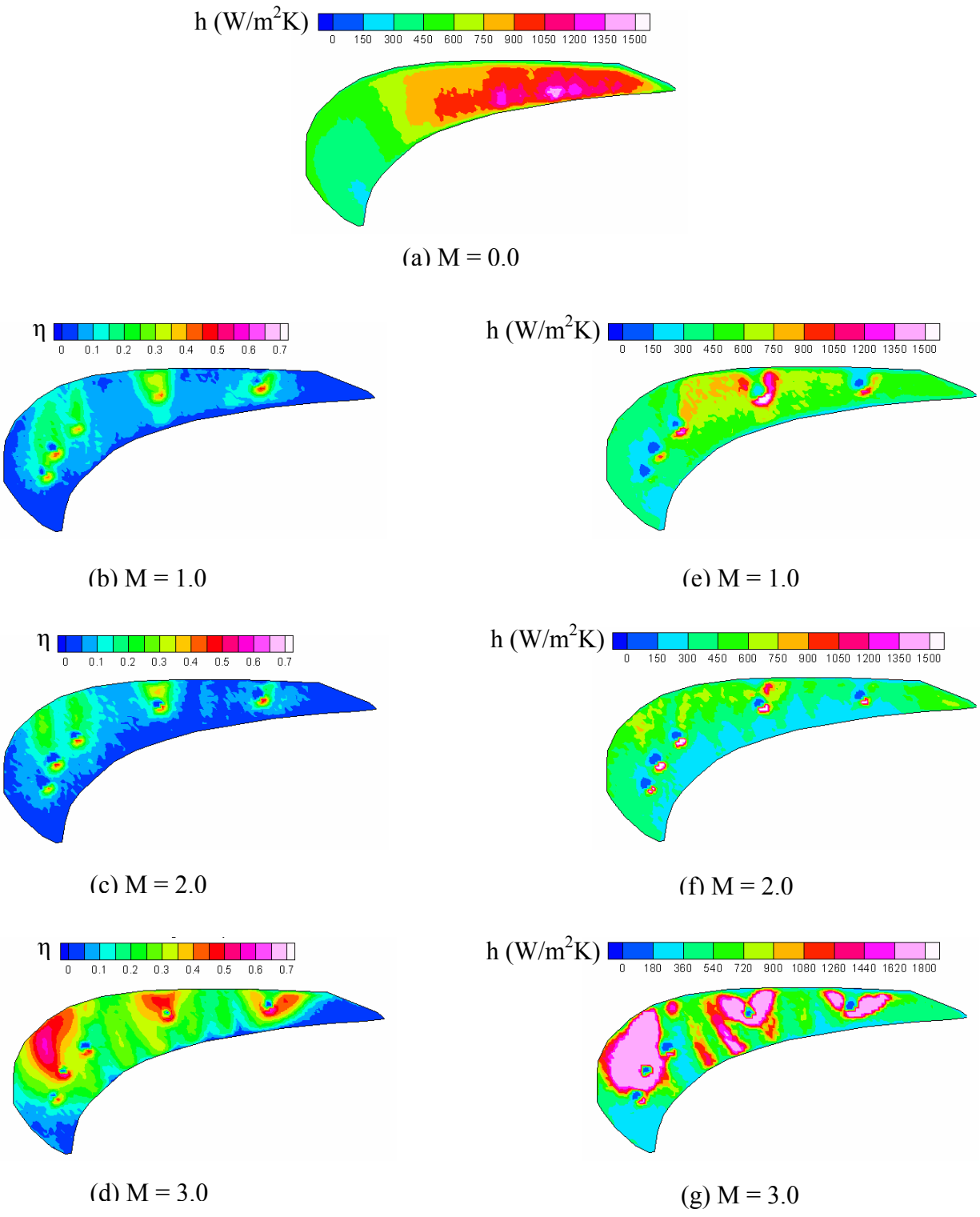


Figure 8.4: Effect of blowing ratio on plane tip heat transfer coefficient and film effectiveness distribution for tip and pressure side coolant injection

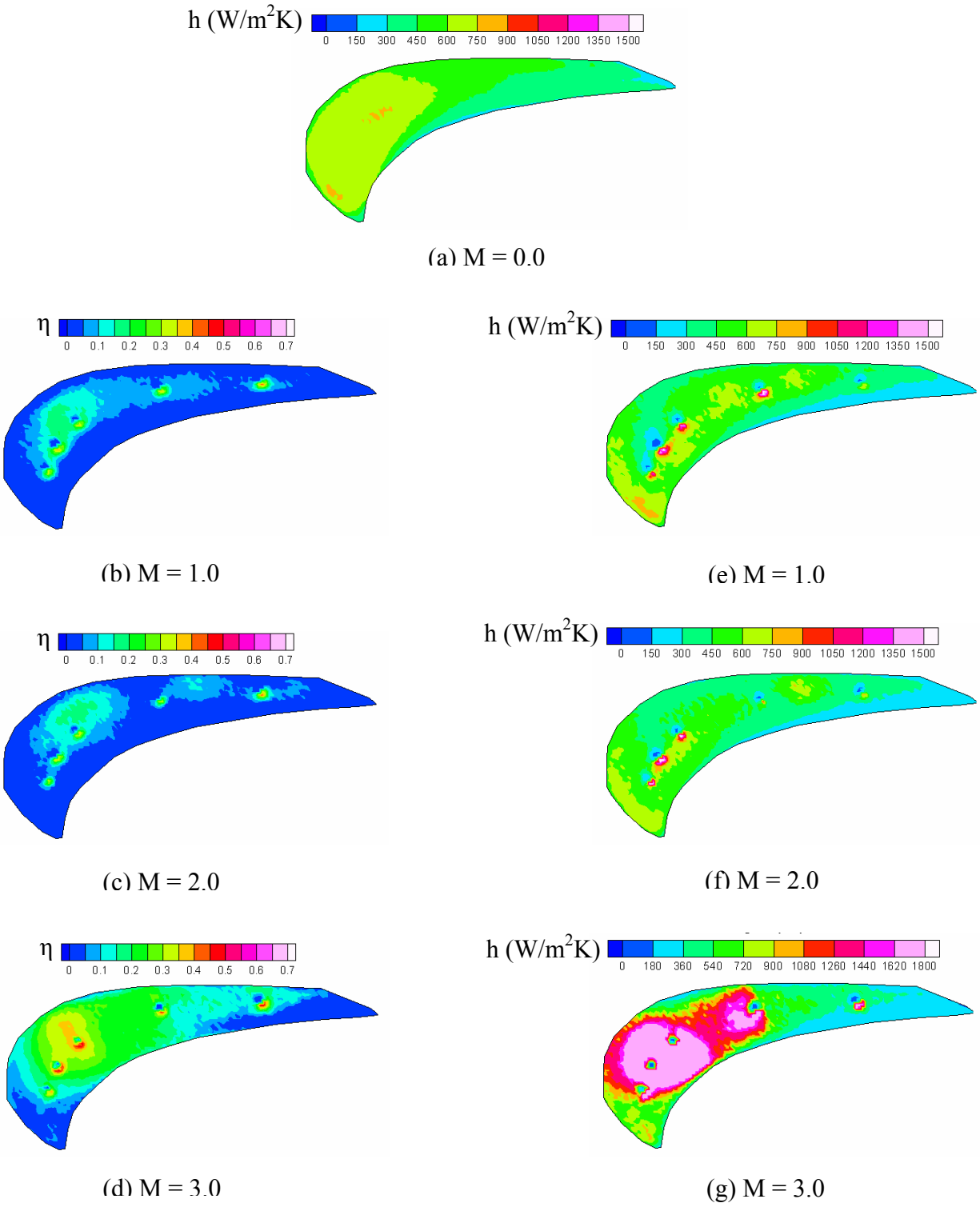
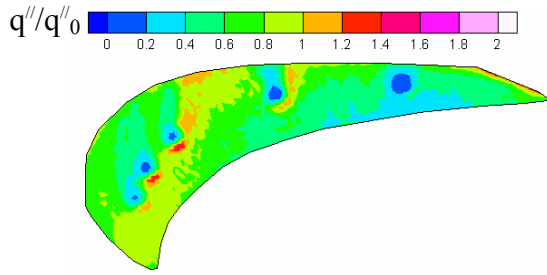
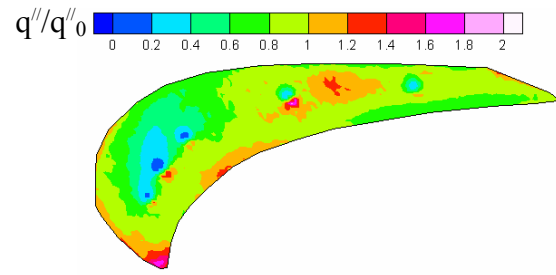


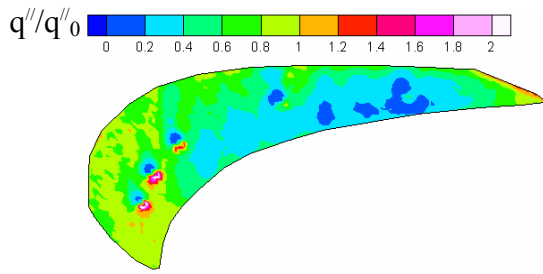
Figure 8.5: Effect of blowing ratio on recessed tip heat transfer coefficient and film effectiveness distribution for tip and pressure side coolant injection



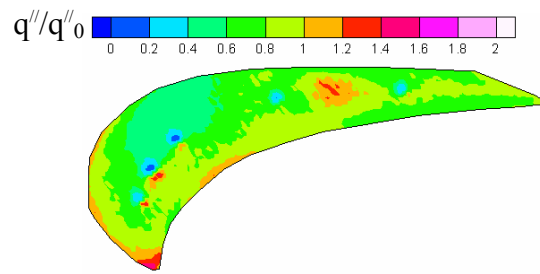
(a) Plane tip (M = 1.0)



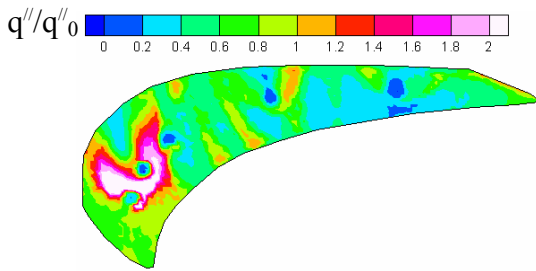
(d) Recessed tip (M = 1.0)



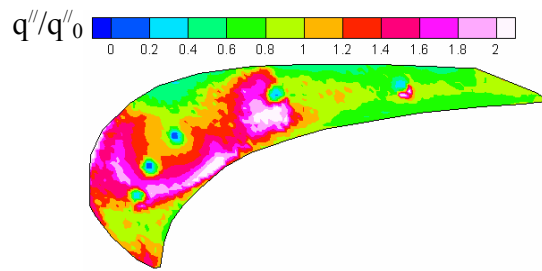
(b) Plane tip (M = 2.0)



(e) Recessed tip (M = 2.0)



(c) Plane tip (M = 3.0)



(f) Recessed tip (M = 3.0)

Figure 8.6: Effect of blowing ratio on plane and recessed tip net heat flux ratio distribution for tip and pressure side coolant injection

CHAPTER 9

9.1 Conclusions

In the first part of the present study, the performance of different recessed tip geometries were investigated and compared with plane tip performance. A transient liquid crystal technology was employed to measure detailed heat transfer coefficient distribution on the blade tip. It was found that burning off of squealer along suction side that represents full pressure side squealer has the poorest performance among all squealer geometries. Also, recessed tip with full peripheral squealer rim proved to be best. It is also observed for partial squealers blade tip that whenever there is squealer rim present along the pressure side, flow appears to accelerate in the middle or camber region of the blade tip.

In the second part of the present study, effects of coolant injection on plane and recessed blade tip were studied for blowing ratios of $M=1.0$, 2.0 and 3.0 . Three cases studied for this case were; (1) coolant injection from holes located on the blade tip, (2) coolant injection from holes located near the tip along the pressure side and, (3) combination cases when coolant is injected both from tip holes and pressure side holes. For tip injection cases, it was found that as blowing ratio increases, heat transfer coefficient decreases for both plane and recessed tip blade. Also, at highest blowing ratio, lift off of jets is observed for both blade tips. Injection of coolant from pressure side holes found to be less effective than tip injection. It appears to be good for plane tip in reducing heat load along the pressure side. But no film effectiveness is observed for recessed tip case. Combined cooling found to be the best among the three cases. For this case, high value of film effectiveness is observed for most of the blade tip. At highest blowing ratio, $M=3$, very high value of heat transfer coefficient and film effectiveness is observed. It appears that for this

high blowing ratio, coolant jet from the tip hits the shroud first and then bounces back on to the blade tip.

It is observed that local blowing ratio is an important parameter to understand flow behavior and particularly for plane tip, local blowing ratios are much more different than global blowing ratios.

9.2 Future Works

For the studied blade tip, it appears that coolant injection from pressure side holes located near blade tip is not efficient for both plane and recessed tip. Especially for recessed tip, no effectiveness is observed. Holes located on the blade tip but along the pressure side can be an alternative choice. A comparative study between these two cases will be valuable.

Cold air used for the coolant is very precious to design engineers. It appears that for pressure side injection, holes located near the leading edge are not beneficial. More studies should be carried out to optimize the location and no of holes for both plane and recessed tip blade.

REFERENCES

- [1] Metzger, D.E., Bunker, R.S., Chyu, M.K., 1989, "Cavity Heat Transfer on a Transverse Grooved Wall in a Narrow Flow Channel," *ASME Journal of Heat Transfer*, Vol. 111, pp. 73-79.
- [2] Bindon, J. P." The Measurements and Formation of Tip Clearance Loss," *Journal of Turbomachinery*, Vol. 111, pp. 257-263, 1989.
- [3] Han, J.C., Dutta, S and Ekkad, S.V. *Gas Turbine Heat Transfer and Cooling Technology*, New York: Taylor and Francis, 2000.
- [4] Lattime, S. B. and Steinetz, B. M., 2002, "Turbine Engine Clearance Control Systems: Current Practices and Future Directions," NASA TM 2002-211794.
- [5] Bunker, R. S. "Axial Turbine Blade Tips: Function, Design, and Durability", *AIAA Journal of Propulsion and Power*.
- [6] Christophel, J. R., Couch, E. and Thole, K. A. "Measured Adiabatic Effectiveness and Heat Transfer for Blowing from the Tip of a Turbine Blade," GT2004-53250, Proceedings of ASME Turbo Expo 2004, Vienna, Austria.
- [7] Rains, D. A., " Tip Clearance Flow in Axial Flow Compressors and Pumps," California Institute of Technology, Mech. Eng. Lab. Report 5, 1954.
- [8] Lakshminaryana, B. " Methods of Predicting the Tip Clearance Effects in Axial Flow Turbomachinery," *ASME Journal of Basic Engineering*, Vol. 92, pp. 467-480, 1970.
- [9] Booth, T. C., Dodge, P. R. and Hepworth, H. K." Rotor-Tip Leakage: Part I—Basic Methodology," *Transactions of the ASME*, Vol. 104, pp. 154-161, 1982.
- [10] Bindon, J. P." Visualization of Axial Turbine Tip Clearance Using a Linear Cascade," Report No. CUED/A-Turbo TR122, Whittle Laboratory, Cambridge University, United Kingdom.

- [11] Bindon, J. P.” Pressure and Flow Field Measurements of Axial Turbine Tip Clearance Flow in a Linear Cascade,” CUED/A-Turbo TR123, Whittle Laboratory, Cambridge University, United Kingdom.
- [12] Yamamoto, A. “Endwall Flow/Loss Mechanisms in a Linear Turbine Cascade With Blade Tip Clearance,” Transactions of the ASME, Vol. 111, pp. 264-275, 1989.
- [13] Yaras, M., Yingkang, Zhu and Sjolander, S. A.” Flow Field in the Tip Gap of a Planar Cascade of Turbine Blades,” Transactions of the ASME, Vol. 111, pp. 276-283, 1989.
- [14] Mayle, R. E. and Metzger, D. E.” Heat Transfer at the Tip of an Unshrouded Turbine Blade,” Seventh Int. Heat Transfer Conf., Hemisphere Pub., pp. 87-92, 1982.
- [15] Chyu, M. K., Moon, H. K. and Metzger, D. E.” Heat Transfer in the Tip Region of Grooved Turbine Blades,” *Journal of Turbomachinery*, Vol. 111, pp. 131-138, 1989.
- [16] Srinivasan, V. and Goldstein, R. J.” Effect of Endwall Motion on Blade Tip Heat Transfer,” *Journal of Turbomachinery*, Vol. 125, pp. 267-273, 2003.
- [17] Bunker, Ronald S., Bailey, Jeremy C. and Ameri, Ali A.” Heat Transfer and Flow on the First-Stage Blade Tip of a Power Generation Gas Turbine: Part 1-Experimental Results,” *Journal of Turbomachinery*, Vol. 122, pp. 263-271, 2000.
- [18] Bunker, Ronald S. and Bailey, Jeremy C.” Effect of Cavity Depth and Oxidation on Turbine Blade Tip Heat Transfer,” 2000-GT-0155, Proceedings of 2001 IGTI, New Orleans, Louisiana.
- [19] Bunker, Ronald S. and Bailey, Jeremy C.” An Experimental Study of Heat Transfer and Flow on a Gas Turbine Blade Tip with Various Tip Leakage Sealing Methods,” 4th ISHMT/ASME Heat and Mass Transfer Conference, 2000, Pune, India.
- [20] Azad, G. S., Han, J. C., Bunker, R. S. and Lee, C. P.” Effect of Squealer Geometry Arrangement on Gas Turbine Blade Tip Heat Transfer,” IMECE2001/HTD-24314, Proceeding of 2001 ASME International Mechanical Engineering Congress and Exposition, New York
- [21] Teng, S., Han, J. C. and Azad, G. S.” Detailed Heat Transfer Coefficient Distributions on a Large-Scale Gas Turbine Blade Tip”, *Journal of Heat Transfer*, Vol. , pp. , .

[22] Kwak, J. S., Ahn, J., Han, J. C., Lee C. P., Bunker, R. S., Boyle, R. and Gaugler, R.” Heat Transfer Coefficients on the Squealer Tip and Near Tip Regions of a Gas Turbine Blade with Single or Double Squealer,” GT2003-38907, Proceeding of ASME Turbo Expo 2003, Atlanta, Georgia, USA.

[23] Papa, M., Goldstein, R. J. and Gori, F.” Effects of Tip Geometry and Tip Clearance on the Mass/Heat Transfer from a Large-Scale Gas Turbine Blade,” GT-2002-30192, Proceedings of ASME Turbo Expo 2002, Amsterdam, Netherlands.

[24] Dunn, M. G. and Haldeman, C. W.” Time-Averaged Heat Flux for a Recessed Tip, Lip, and Platform of a Transonic Turbine Blade,” 2000-GT-0197, Proceeding of IGTI: ASME Turbo Expo 2000, Munich, Germany.

[25] Saxena, V., Nasir, H., and Ekkad, S. V.,” Effect of Blade Tip Geometry on Tip Flow and Heat Transfer for a Blade in a Low-Speed Cascade”, *ASME Journal of Turbomachinery*, Volume 126, pp. 130-138, January 2004.

[26] Kim, Y. W., Downs, J. P., Soechting, F. O., Abdel-Messeh, W., Steuber, G. D. and Tanrikut, S.” A Summary of the Cooled Turbine Blade Tip Heat Transfer and Film Effectiveness Investigations Performed by Dr. D. E. Metzger,” *Journal of Turbomachinery*, Vol. 117, pp. 1-10, 1995.

[27] Kwak, J. S. and Han, J. C.” Heat Transfer Coefficient and Film-Cooling Effectiveness on a Gas Turbine Blade Tip”, GT-2002-30194, Proceeding of ASME Turbo Expo 2002, Amsterdam, Netherlands.

[28] Ahn, J., Mhetras, S. and Han, J. C.” Film-Cooling Effectiveness on a Gas Turbine Blade Tip Using Pressure Sensitive Paint,” GT2004-53249, Proceedings of ASME Turbo Expo 2004, Vienna, Austria.

[29] Christophel, J. R., Thole, K. A. and Cunha, F. J. “Cooling The Tip of a Turbine Blade Using Pressure Side Holes. Part 2: Heat Transfer Measurements,” GT2004-53254, Proceedings of ASME Turbo Expo 2004, Vienna, Austria.

[30] Polanka, M. D., Clark, J. P., White, A. L., Meininger, M. and Praisner, T. J. “ Turbine Tip and Shroud Heat Transfer and Loading. Part B: Comparisons Between Prediction and Experiment Including Unsteady Effects,” GT-2003-38916, Proceedings of ASME Turbo Expo 2003, June 16-19, 2003, Atlanta, Georgia, USA.

[31] Ameri, A. A., Steinthorsson, E. and Rigby, D. L.” Effect of Squealer Tip on Rotor Heat Transfer and Efficiency,” *Journal of Turbomachinery*, Vol. 120, pp. 753-759, 1998.

[32] Ameri, A. A., Steinthorsson, E. and Rigby, D.L. “ Effects of Tip Clearance and Casing Recess on Heat Transfer and Stage Efficiency in Axial Turbines,” *ASME Journal of Turbomachinery*, Vol. 121, pp. 683-693, 1999.

[33] Ameri, A. A.” Heat Transfer and Flow on the Blade Tip of a Gas Turbine Equipped with a Mean-Camberline Strip,” 2001-GT-0156, Proceedings of ASME Turbo Expo 2001, New Orleans, Louisiana.

[34] Yang, H., Acharya, S. and Ekkad, S. V.” Numerical Simulation of Flow and Heat Transfer Past a Turbine Blade with a Squealer-Tip,” GT-2002-30193, Proceedings of ASME TURBO EXPO 2002, Amsterdam, Netherlands.

[35] Yang, H., Chen, H. C. and Han, J. C.” Numerical Prediction of Film Cooling and Heat Transfer with Different Film-Hole Arrangements on the Plane and Squealer Tip of a Gas Turbine Blade,” GT2004-53199, Proceedings of ASME Turbo Expo 2004, Vienna, Austria.

[36] Incropera, F. P. and DeWitt, D. P. *Introduction to Heat Transfer*, New York: John Wiley & Sons, 2002.

[37] Metzger, D. E., and Larson, D. E., 1986, “Use of Melting Point Surface Coatings or Local Convective Heat Transfer Measurements in Rectangular Channel Flows with 90-Deg. Turns,” *ASME Journal of Heat Transfer*, Vol. 108, pp. 48-54.

[38] Vedula, R. P., and Metzger, D. E., 1991, “A Method for the Simultaneous Determination of Local Effectiveness and Heat Transfer Distributions in a Three Temperature Convective Situations,” ASME Paper 91-GT-345.

[39] Ekkad, S.V., Du, H., and Han, J. C., 1998, “Detailed Film Cooling Measurements on a Cylindrical Leading Edge Model: Effect of Free-stream Turbulence and Density Ratio,” *ASME Journal of Turbomachinery*, Vol. 120, pp. 779-807.

[40] Du, H. Han, J. C., and Ekkad, S.V., 1998, “Effect of Unsteady Wake on Detailed Heat Transfer Coefficient and Film Effectiveness Distributions for a Gas Turbine Blade,” *ASME Journal of Turbomachinery*, Vol. 120, pp. 808-817.

[41] Ekkad, S. V., Ou, S. and Rivir, R. V.” A Transient Infrared Thermography Method for Simultaneous Film Cooling Effectiveness and Heat Transfer Coefficient Measurements from a Single test,” GT2004-54236, Proceedings of ASME Turbo Expo 2004, Vienna, Austria.

[42] Gritsch, M., Schulz, A., and Witting, S., 1998, “Discharge Coefficient Measurements of Film-Cooling Holes with Expanded Exits,” *ASME Journal of Turbomachinery*, Vol. 120, pp. 557-563.

[43] Kline, S.J. and McClintock, F.A., 1953, “Describing Uncertainties in Single Sample Experiments,” *Mechanical Engineering*, Vol. 75, pp. 3-8.

[44] FLIR Systems, Incorporated. (2000). Feature Spec ThermoCAM SC Series [User’s Manual]. North Billerica, MA.

[45] Rohm and Haas Company. (1999). *CVD Zinc-Selenide*. Retrieved August 10, 2004, from <http://www.cvdmaterials.com/znse.htm>.

[46] Kontrovitz, D. M., (2000). *Effect of Tip Geometry on Blade Tip Flow and Heat Transfer*. Unpublished masters thesis, Louisiana State University, Baton Rouge.

[47] FLIR Systems, Incorporated. (2003). ThermoCAM TM Researcher, Professional Edition, Version 2.7[User’s Manual]. North Billerica, MA.

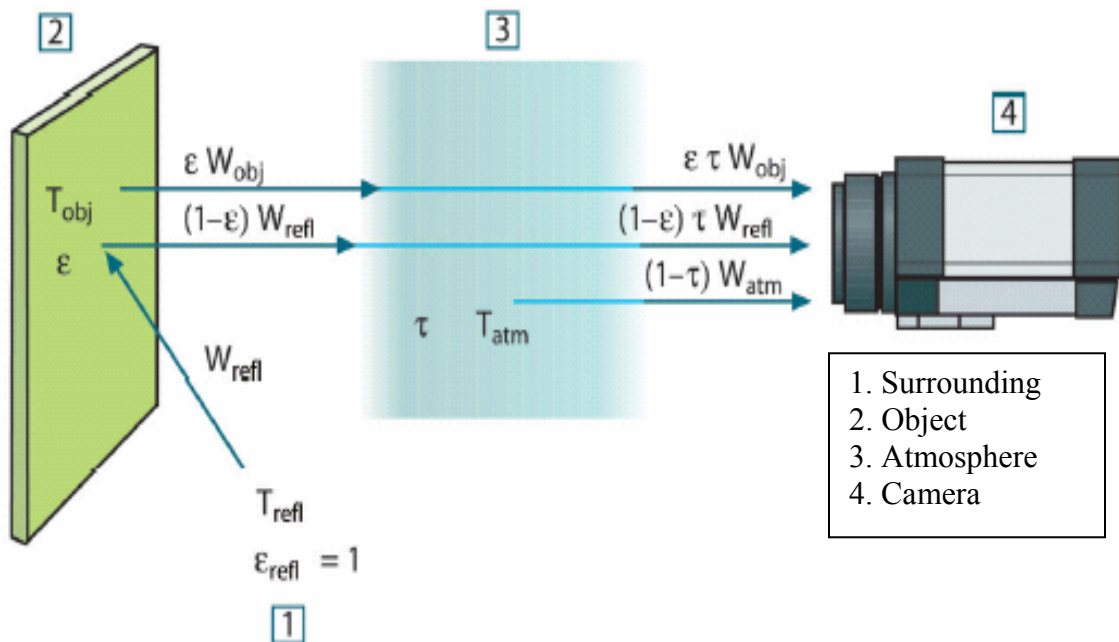
APPENDIX I: IR CAMERA MEASUREMENT FORMULA

The Figure below represents fairly true description of the measurement situation in real conditions. What has been neglected could for instance be sun light scattering in the atmosphere or stray radiation from intense radiation sources outside the field of view. Fortunately, in most cases they are small enough to be neglected.

Assume that the received radiation power W from a blackbody source of temperature T_{source} on short distance generates a camera output signal U_{source} that is proportional to the power input (power linear camera). We can then write the following equation

$$U_{\text{source}} = CW (T_{\text{source}}) \text{ or with simplified notation } U_{\text{source}} = CW_{\text{source}}$$

Where C is constant. Should the source be a graybody with emittance ε , the received radiation would consequently be $\varepsilon W_{\text{source}}$.



A schematic representation of the general thermographic measurement situation [47]

We are now ready to write the three collected radiation power terms:

Emission from the object = $\varepsilon \tau W_{\text{obj}}$, where ε is the emittance of the object and τ is the transmittance of the atmosphere. The object temperature is T_{obj} .

Reflected emission from the ambient source = $(1-\varepsilon)\tau W_{\text{refl}}$, where $(1-\varepsilon)$ is the reflectance of the object. The ambient sources have the temperature T_{refl} .

It has been assumed that the temperature T_{refl} is the same for all emitting surfaces within the half sphere seen from a point on the object surface. This is of course sometimes a simplification of the true situation. It is, however, a necessary simplification in order to derive a workable formula. Also, we have assumed that the emittance for the surroundings is equal to 1. This is correct in accordance with Kirchoff's law: All radiation impinging on the surrounding surfaces will be absorbed by the same surfaces.

Emission from the atmosphere = $(1-\tau)W_{\text{atm}}$, where $(1-\tau)$ is the emittance of the atmosphere. The temperature of the atmosphere is T_{atm} .

For the above three power terms, it is assumed that the view factor between the object and the camera is 1. In other words, the camera receives all the energy leaving the object, which is not the ideal case for many situations. But if the view factor is assumed 1, we can write the total received radiation power as [47]

$$W_{\text{tot}} = \varepsilon \tau W_{\text{obj}} + (1-\varepsilon)\tau W_{\text{refl}} + (1-\tau)W_{\text{atm}}$$

We multiply each term by the constant C of equation 1 and replace the CW products by the corresponding U according to the same equation and get the following equation

$$U_{\text{tot}} = \varepsilon \tau U_{\text{obj}} + (1-\varepsilon)\tau U_{\text{refl}} + (1-\tau)U_{\text{atm}}$$

Solving the above equation for U_{obj}

$$U_{\text{obj}} = \frac{1}{\varepsilon\tau} U_{\text{tot}} - \frac{1-\varepsilon}{\varepsilon} U_{\text{refl}} - \frac{1-\tau}{\varepsilon\tau} U_{\text{atm}}$$

This is the general measurement formula used in the Infrared (IR) camera used for the measurement.

Where,

U_{obj} = Calculated camera output voltage for a blackbody of temperature, T_{obj} i.e. a voltage that can be directly converted into true requested object temperature.

U_{tot} = Measured camera output voltage for the actual case.

U_{refl} = Theoretical camera output voltage for a blackbody of temperature, T_{refl} according to the calibration.

U_{atm} = Theoretical camera output voltage for a blackbody of temperature, T_{atm} according to the calibration.

APPENDIX II: UNCERTAINTY ANALYSIS

The following equation is used to calculate h for flow over a semi-infinite solid

$$\frac{T_w - T_i}{T_m - T_i} = 1 - \left[\exp\left(\frac{h^2 \alpha t}{k^2}\right) \right] \left[\operatorname{erfc}\left(\frac{h\sqrt{\alpha t}}{k}\right) \right] \quad (1)$$

For our case

Initial temperature, $T_i = 70 \text{ }^\circ\text{C}$

Mainstream temperature, $T_m = 20 \text{ }^\circ\text{C}$

Thermal conductivity of plexiglas, $k = 0.18737082 \text{ watt/mK}$

Thermal diffusivity of plexiglas, $\alpha = 1.075214904 \times 10^{-7} \text{ m}^2/\text{sec}$

Now, let us assume that wall temperature drops to $25 \text{ }^\circ\text{C}$ in 5 seconds in actual experiment.

So, Wall temperature, $T_w = 25 \text{ }^\circ\text{C}$

Time of change, $t = 5 \text{ sec}$

Now, if it is assumed that all the temperatures, time and variables mentioned above are true values without any error and solve the equation for h, the calculated value will be the actual h without any error. After solving equation (1),

$h_a = 1416 \text{ watt/m}^2\text{K}$ (Actual value without any error)

Now let us assume the maximum deviation (in the positive direction) for all the variables

Initial temperature, $T_i = 70 + 2 = 72 \text{ }^\circ\text{C}$

Mainstream temperature, $T_m = 20 + 0.2 = 20.2 \text{ }^\circ\text{C}$

Thermal conductivity of plexiglas, $k = 0.19299194 \text{ watt/mK}$

Thermal diffusivity of plexiglas, $\alpha = 1.107 \times 10^{-7} \text{ m}^2/\text{sec}$

Wall temperature, $T_w = 25 + 0.2 = 25.2 \text{ }^\circ\text{C}$

Time of change, $t = 5 + 0.125 = 5.125 \text{ sec}$

After incorporating all the values and solving equation (1), we get

$$h_p = 1471 \text{ watt/m}^2\text{K} \text{ (This is the value using variables with maximum deviation)}$$

Now, let us calculate the % difference between the actual h_a and calculated h_p using variables with maximum deviation

$$\text{Error} = \frac{h_p - h_a}{h_a} \times 100$$

$$\text{Error} = 3.896 \%$$

Effectiveness is calculated using the following equation

$$T_w - T_i = \left[1 - \exp\left(\frac{h^2 \alpha t}{k^2}\right) \operatorname{erfc}\left(\frac{h\sqrt{\alpha t}}{k}\right) \right] \times [\eta T_c + (1 - \eta)T_m - T_i] \quad (2)$$

$$\eta = \frac{T_f - T_m}{T_c - T_m}$$

Now let us assume that the actual coolant temperature, $T_c = 75 \text{ }^\circ\text{C}$ and all the variables are same as before. Also wall temperature drops to $25 \text{ }^\circ\text{C}$ in 5 seconds in actual experiment. In that case, our actual heat transfer coefficient will be $h = 1416 \text{ watt/m}^2\text{K}$. After inserting all the variables in equation (2), we get the actual effectiveness or effectiveness without error

$$\eta_a = 0.873$$

Now let us assume the maximum deviation (in the positive direction) for all the variables

$$\text{Initial temperature, } T_i = 70 + 2 = 72 \text{ }^\circ\text{C}$$

$$\text{Mainstream temperature, } T_m = 20 + 0.2 = 20.2 \text{ }^\circ\text{C}$$

$$\text{Thermal conductivity of plexiglas, } k = 0.19299194 \text{ watt/mK}$$

$$\text{Thermal diffusivity of plexiglas, } \alpha = 1.107 \times 10^{-7} \text{ m}^2/\text{sec}$$

$$\text{Wall temperature, } T_w = 25 + 0.2 = 25.2 \text{ }^\circ\text{C}$$

$$\text{Time of change, } t = 5 + 0.125 = 5.125 \text{ sec}$$

And heat transfer coefficient, $h = 1471 \text{ watt/m}^2\text{K}$

After incorporating all the values and solving equation (1), we get

$$\eta_p = 0.942 \text{ (This is the value using variables with maximum deviation)}$$

Now, let us calculate the % difference between the actual η_a and calculated η_p using variables with maximum deviation

$$\text{Error} = \frac{\eta_p - \eta_a}{\eta_a} \times 100$$

$$\text{Error} = 7.86 \%$$

VITA

Hasan Nasir was born in Dhaka, Bangladesh, on June 1st, 1972. He is the eldest son of his parents, Abdul Quadir Bhuiyan and Shamsunnar Shelly. He received his high school degree from Rajshahi College in Rajshahi, Bangladesh, in August of 1990. Next he attended Bangladesh University of Engineering and Technology (BUET) where he obtained his Bachelor of Science in Mechanical Engineering in July of 1997. Hasan then attended Louisiana State University Graduate School to pursue his Doctor of Philosophy degree in mechanical engineering. As of December 2004, he has completed all the requirements to obtain the degree of Doctor of Philosophy in mechanical engineering, which he will receive in December of 2004.